

N73-16813

17433-6002-R0-00

STUDY OF  
IMPACT CRATERING IN  
LUNAR-LIKE MATERIALS

FINAL REPORT

**CASE FILE  
COPY**

by

N. L. Roy and J. C. Slattery

Prepared for

NATIONAL AERONAUTICS AND SPACE ADMINISTRATION  
HEADQUARTERS  
Washington, D.C. 20546  
Contract No. NASW-2311

JANUARY 1973

**TRW**  
SYSTEMS GROUP

ONE SPACE PARK • REDONDO BEACH, CALIFORNIA 90278

STUDY OF  
IMPACT CRATERING IN LUNAR-LIKE MATERIALS

FINAL REPORT

Prepared by: N. L. Roy  
N. L. Roy  
Meteoritics  
Systems Group Research Staff

and: J. C. Slattery  
J. C. Slattery  
Meteoritics  
Systems Group Research Staff

Approved by: J. F. Friichtenicht  
J. F. Friichtenicht, Manager  
Meteoritics  
Systems Group Research Staff

## ABSTRACT

Electrostatically accelerated microparticles are used to perform simulated micrometeoroid impact cratering experiments in oligoclase. Impact craters were obtained using iron, lanthanum hexaboride, and silicon as the projectile materials. Each particle material was impacted at normal incidence and at 30° and 60° oblique angles. Tabular data for all impacts are presented and central crater pit diameter normalized to particle diameter and the total spall diameter normalized to particle diameter are plotted vs impact velocity for nine particle/angle combinations and three crystal orientations. Impact crater characteristics are photodocumented as a function of impact velocity for the nine particle/angle combinations and three crystal orientations in oligoclase and at fixed impact velocity for six other minerals.

## TABLE OF CONTENTS

	<u>Page</u>
ABSTRACT . . . . .	iii
LIST OF ILLUSTRATIONS . . . . .	vi
1.0 INTRODUCTION . . . . .	1
2.0 DESCRIPTION OF THE MICROPARTICLE FACILITY . . . . .	2
2.1 The Van de Graaff Accelerator and Associated Apparatus . . . . .	2
2.2 The Linear Accelerator . . . . .	6
3.0 EXPERIMENTAL PROCEDURE . . . . .	10
3.1 The Target Chamber . . . . .	10
3.2 Identification of Impact Craters . . . . .	12
3.3 Data Acquisition Procedures . . . . .	13
3.4 The Target Material . . . . .	14
3.5 Particle Materials . . . . .	17
4.0 EXPERIMENTAL RESULTS . . . . .	19
4.1 Quantitative Data on Cratering Parameters . . . . .	19
4.1.1 Iron Particle Impacts on Oligoclase and Miscellaneous Minerals . . . . .	19
4.1.1.1 Normal impacts on Oligoclase . . . . .	19
4.1.1.2 Normal Impacts on Miscellaneous Minerals . . . . .	23
4.1.1.3 Oblique Impacts on Oligoclase . . . . .	25
4.1.2 Lanthanum Hexaboride Particle Impacts on Oligoclase . . . . .	34
4.1.3 Silicon Particle Impacts on Oligoclase . . . . .	41
4.1.3.1 Normal Impacts at Different Crystal Orientations . . . . .	41
4.1.3.2 Oblique Impacts . . . . .	49

## TABLE OF CONTENTS (continued)

	<u>Page</u>
4.2 Photographs of Impact Craters in Minerals . . . . .	54
4.2.1 Iron Particle Impact Craters . . . . .	55
4.2.1.1 Photographs of Normal Impact Craters in Oligoclase . . . . .	55
4.2.1.2 Photographs of Craters from Normal Impact on Miscellaneous Minerals . . . . .	57
4.2.1.3 Photographs of 60° to Normal Impact Craters in Oligoclase . . . . .	71
4.2.2 Lanthanum Hexaboride Particle Impact Craters in Oligoclase . . . . .	71
4.2.2.1 Photographs of Normal Impact Craters . . . . .	71
4.2.2.2 Photographs of Oblique Impacts . . . . .	77
4.2.3 Silicon Particle Impact Craters in Oligoclase . . . . .	77
4.2.3.1 Photographs of Normal Impact Craters at Different Crystal Orientations . . . . .	77
4.2.3.2 Oblique Impacts . . . . .	82
5.0 SUMMARY . . . . .	93
REFERENCES . . . . .	95

## LIST OF ILLUSTRATIONS

<u>Figure</u>		<u>Page</u>
2-1	Block Diagram of TRW Systems Group Micrometeoroid Simulation and Test Facility, showing setup for impact cratering . . . . .	3
2-2	Block Diagram of Linear Accelerator . . . . .	7
3-1	Diagram of Particle Position Detector and Target Chamber . .	11
3-2	SEM Photographs of Iron, Silicon, and Lanthanum Hexaboride Particles . . . . .	17
4-1	Crater Diameter/Particle Diameter vs Particle Velocity for Normal Impact of Iron Particles on Oligoclase . . . . .	22
4-2	Crater Diameter/Particle Diameter vs Particle Velocity for 30° to Normal Impacts of Iron Particles on Oligoclase . . . . .	33
4-3	Crater Diameter/Particle Diameter vs Particle Velocity for 60° to Normal Impacts of Iron Particles on Oligoclase . . . . .	37
4-4	Crater Diameter/Particle Diameter vs Particle Velocity for Normal Impact of Lanthanum Hexaboride Particles on Oligoclase . . . . .	40
4-5	Crater Diameter/Particle Diameter vs Particle Velocity for Oblique Impacts of Lanthanum Hexaboride Particles on Oligoclase . . . . .	42
4-6	Crater Diameter/Particle Diameter vs Particle Velocity for Normal Impact of Silicon Particles on Oligoclase, Target Surface Parallel to (010) . . . . .	44
4-7	Crater Diameter/Particle Diameter vs Particle Velocity for Normal Impact of Silicon Particles on Oligoclase, Target Surface at 45° to (010) and (001) . . . . .	46
4-8	Crater Diameter/Particle Diameter vs Particle Velocity for Normal Impact of Silicon Particles on Oligoclase, Target Surface Parallel to (001) . . . . .	48
4-9	Crater Diameter/Particle Diameter vs Particle Velocity for 30° to Normal Oblique Impact of Silicon Particles on Oligoclase . . . . .	51

## LIST OF ILLUSTRATIONS (continued)

<u>Figure</u>		<u>Page</u>
4-10	Crater Diameter/Particle Diameter vs Particle Velocity for 60° to Normal Oblique Impact of Silicon Particles on Oligoclase . . . . .	53
4-11	Photographs of Craters from Normal Impacts of Iron Particles on Oligoclase, 2.86 to 5.47 km/s: . . . . .	56
4-12	Photographs of Craters from Normal Impacts of Iron Particles on Oligoclase, 6.16 to 11.4 km/s: . . . . .	58
4-13	Photographs of Craters from Normal Impacts of Iron Particles on Oligoclase at 3.06 km/s: . . . . .	59
4-14	Photographs of Craters from Normal Impacts of Iron Particles on Diopside at 3.06 km/s: . . . . .	60
4-15	Photographs of Craters from Normal Impacts of Iron Particles on Biotite Mica at 3.06 km/s: . . . . .	62
4-16	Photographs of Craters from Normal Impacts of Iron Particles on Hedenbergite at 3.06 km/s: . . . . .	63
4-17	Photographs of Craters from Normal Impacts of Iron Particles on Ilmenite at 3.06 km/s: . . . . .	64
4-18	Photographs of Craters from Normal Impacts of Iron Particles on Monticellite at 3.06 km/s: . . . . .	65
4-19	Photographs of Craters from Normal Impacts of Iron Particles on Orthoclase at 3.06 km/s: . . . . .	66
4-20	Photographs of Craters from 30° to Normal Oblique Impacts of Iron Particles on Oligoclase at 3.06 km/s: . . .	68
4-21	Photographs of Craters from 30° to Normal Oblique Impacts of Iron Particles on Oligoclase, 2.45 to 4.93 km/s: . . . . .	69
4-22	Photographs of Craters from 30° to Normal Oblique Impacts of Iron Particles on Oligoclase, 5.93 to 27.9 km/s: . . . . .	70
4-23	Photographs of Craters from 60° to Normal Oblique Impacts of Iron Particles on Oligoclase at 3.06 km/s: . . .	72
4-24	Photographs of Craters from 60° to Normal Oblique Impacts of Iron Particles on Oligoclase, 1.91 to 5.20 km/s: . . . . .	73

## LIST OF ILLUSTRATIONS (continued)

<u>Figure</u>		<u>Page</u>
4-25	Photographs of Craters from 60° to Normal Oblique Impacts of Iron Particles on Oligoclase, 6.57 to 26.1 km/s: . . . . .	74
4-26	Photographs of Craters from Normal Impacts of Lanthanum Hexaboride Particles on Oligoclase, 1.46 to 5.12 km/s: . . . . .	75
4-27	Photographs of Craters from Normal Impacts of Lanthanum Hexaboride Particles on Oligoclase, 6.21 to 22.9 km/s: . . . . .	76
4-28	Photographs of Craters from 30° to Normal Oblique Impacts of Lanthanum Hexaboride Particles on Oligoclase, 2.43 to 5.31 km/s: . . . . .	78
4-29	Photographs of Craters from 60° to Normal Oblique Impacts of Lanthanum Hexaboride Particles on Oligoclase, 3.08 to 8.18 km/s: . . . . .	79
4-30	Photographs of Craters from Normal Impacts of Silicon Particles on Oligoclase, Surface Parallel to (010), 2.40 to 8.52 km/s: . . . . .	80
4-31	Photographs of Craters from Normal Impacts of Silicon Particles on Oligoclase, Surface Parallel to (010), 9.68 to 22.4 km/s: . . . . .	81
4-32	Photographs of Craters from Normal Impacts of Silicon Particles on Oligoclase, Surface at 45° to both (010), and (001), 2.12 to 5.25 km/s: . . . . .	83
4-33	Photographs of Craters from Normal Impacts of Silicon Particles on Oligoclase, Surface at 45° to both (010) and (001), 5.31 to 12.7 km/s: . . . . .	84
4-34	Photographs of Craters from Normal Impacts of Silicon Particles on Oligoclase, Surface Parallel to (001), 2.82 to 10.6 km/s: . . . . .	85
4-35	Photographs of Craters from Normal Impacts of Silicon Particles on Oligoclase, Surface Parallel to (001), 10.6 to 12.4 km/s: . . . . .	86
4-36	Photographs of Craters from 30° to Normal Oblique Impacts of Silicon Particles on Oligoclase, 2.31 to 8.18 km/s: . . . . .	87

## LIST OF ILLUSTRATIONS (continued)

<u>Figure</u>		<u>Page</u>
4-37	Photographs of Craters from 30° to Normal Oblique Impacts of Silicon Particles on Oligoclase, 10.5 to 20.6 km/s: . . . . .	88
4-38	Photographs of Craters from 60° to Normal Oblique Impacts of Silicon Particles on Oligoclase, 2.18 to 9.08 km/s: . . . . .	90
4-39	Photographs of Craters from 60° to Normal Oblique Impacts of Silicon Particles on Oligoclase, 10.6 to 19.5 km/s: . . . . .	91

1.0

INTRODUCTION

Since the first Apollo team returned from the moon with lunar samples, investigators have been reporting the existence of numerous impact microcraters in the surfaces of the rocks and spherules which had been exposed to the lunar surface environment. The objective of this program has been to act as a supporting study and to provide additional information regarding cratering characteristics in lunar-like materials to that already existing in the field. Hopefully, the information obtained would aid investigators in their analyses of microcraters found in the lunar samples. Specifically, the goal was to perform a detailed set of controlled laboratory experiments in earth-type minerals with properties similar in nature to those found on the moon. The goal of such experiments is to generate a "catalog" of impact crater photographs arranged so as to convey as much information as possible regarding the relationship between observed crater details and the parameters of the target and impacting particle.

Toward this end, impact experiments have been conducted utilizing iron, lanthanum hexaboride, and silicon as the impacting particle materials. For the target material, a piece of oligoclase single crystal was selected as being a closely representative mineral. Impacts were obtained at three different angles of impact for each of the three different particle materials. In addition, craters were obtained at fixed impact velocity in six other common minerals using iron particles. Impacts were also obtained at three different crystal orientations for silicon particle impacts on an oligoclase target.

A description of the accelerator facility and the experimental arrangements used is given to provide a foundation for the data to be presented. This is followed by a comprehensive accounting of the numerical data obtained and such relationships as was found to exist. The final data presented is a rather large collection of scanning electron microscope crater photographs including a group for each set of conditions studied.

2.0 DESCRIPTION OF THE MICROPARTICLE FACILITY2.1 The Van de Graaff Accelerator and Associated Apparatus

Before presenting the cratering data obtained during the course of the subject program, a description of the experimental facility is given in order to acquaint the reader with the electrostatic techniques employed to generate high velocity microparticles. This description should also serve to illustrate the advantages of electrostatically accelerated particles and also the limitations imposed upon the experimenter by their use.

One of the two experimental arrangements used is shown in the block diagram of Figure 2-1. The source of microparticles in this arrangement is a two million volt Van de Graaff generator, shown as a block at the left of the figure, in which the high voltage terminal has been modified to accept microparticle charging and injection equipment<sup>1</sup>. Particle charging is accomplished by electrically agitating a supply of the microparticles thereby causing some to come into contact with a small tungsten electrode held at a high positive potential. Contact with the electrode causes the particle to rebound with a high positive charge and surface electric field strength of about  $10^9$  volts per meter. The rebounding particle then enters the accelerator tube of the Van de Graaff where it is accelerated by the positive potential of the Van de Graaff terminal.

The final velocity obtained as the particles exit the Van de Graaff is dependent upon the total accelerating potential, the material used, and the geometry of the particular particle. The upper velocity limit is dependent upon the electronics used since it is generally detection limited by signal-to-noise considerations. For most metallic materials, or materials having volume resistivities less than about  $10^7$  ohm-centimeters, the size range 0.1 to 5.0 microns can be accelerated to final velocities in the range from 1 to 50 km/s. The final velocity is

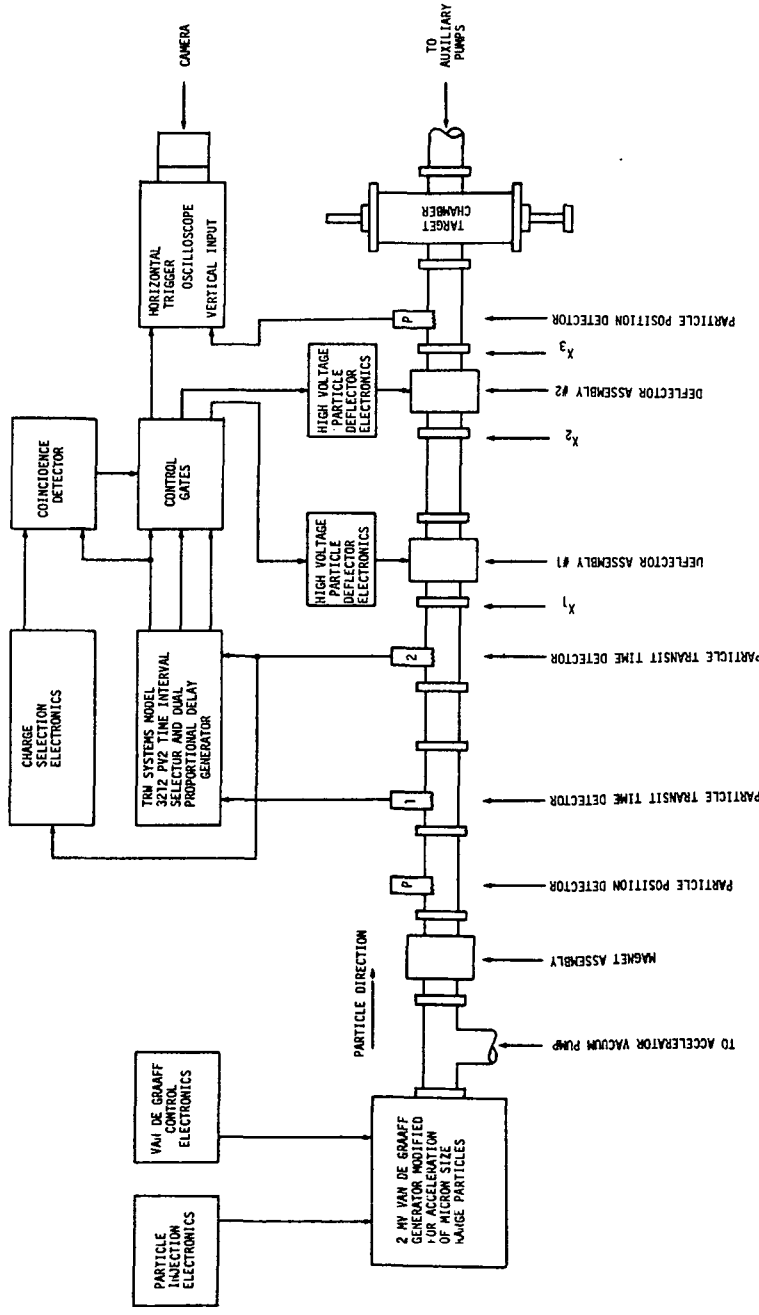


FIGURE 2-1. Block Diagram of TRW Systems Group Micrometeoroid Simulation and Test Facility, showing setup for impact cratering. A particle emerging from Van de Graaff passes first through magnet assembly where ions created by charging process are deflected then passes through position detector (P) and transit time detectors 1 and 2. Transit time is measured by Time Interval Selector (TIS) and charge amplitude by charge selection electronics. If both are within preset limits, coincidence detector activates control gates allowing first pulse from TIS (occurs when selected particle is at position  $X_1$ ) to remove voltage from deflector assembly #1. Two proportionally delayed pulses then occur: first (when particle is at position  $X_2$ ) removes voltage from deflector assembly #2; second (when particle is at position  $X_3$ ) triggers oscilloscope sweep causing particle charge and transit time to be recorded as it passes through final position detector before impacting target in target chamber.

inversely proportional to particle size with the higher velocities being obtained only with the smaller particles. Particle injection may be controlled over a wide range of output particle flux. At the lower limits it can be made essentially a single shot device while at the upper limits the output particle flux can be raised to several hundred per second.

Particles exiting from the accelerator first pass through a magnet assembly where ions, which may have been produced by the charging process, are removed. A particle position detector<sup>2</sup> then provides a means for locating the particle "beam" axis in order to align the system. (This detector will be described in more detail later.) The particles next pass through two detectors, spaced apart a carefully measured distance, and the transit time over this distance is measured. The time separation of the two detector signals is analyzed by a TRW Systems Model 3212 PV2 Time Interval Selector and Dual Proportional Delay Generator<sup>3</sup>.

This unit provides two functions: first, it provides an output pulse to a particle deflector when the measured transit time falls within the bounds of some predetermined time interval. Normally, with no signal applied to the input of the particle deflector high voltage electronics, all particles are deflected by a bias voltage on a pair of parallel deflector plates and are not allowed to continue downstream toward the experimental area. A signal from the Time Interval Selector removes the bias voltage for a time just sufficient to allow the selected particle to pass. This first deflector pulse, which removes the bias voltage on deflector assembly #1, would normally occur when the particle is detected at the second timing station approximately at the position labeled  $X_1$ , in Figure 2-1. Second, the Time Interval Selector contains proportional delay generators which produce two trigger pulses at adjustable multiples of the actual measured transit time. By proper adjustment of the multiplication factors, these pulses can be made to appear when the selected particle is at two arbitrarily selected points downstream, independent of particle velocity.

The first of these pulses is used to remove the bias voltage on deflector assembly #2 which would occur when the selected particle is at position  $X_2$ . (The reason for a second deflector system is to prevent high velocity particles from "leaking" through the selector system when it is set for lower velocities. With the two deflector arrangement, a fast particle can quickly pass through the first deflector while it is open for a slower (longer transit time) particle. However, the faster particle will find the second deflector still closed and will therefore be deflected out of the experimental area.) As in the case of deflector #1, the pulse remains on deflector #2 for a time just sufficient to allow the selected particle to pass. The second proportionally delayed pulse is used to trigger an oscilloscope and/or recording equipment so that the parameters of the selected particle are recorded as it passes through a sensitive particle detector<sup>4</sup>. This trigger pulse is generated as the selected particle passes the point  $X_3$  just prior to entering the particle detector and target area.

The foregoing paragraph has indicated the sequence of events when particle velocity (transit time) is the only parameter being selected. Provisions also exist to allow simultaneous selection, within certain bounds, of the electrical charge on the particle. The selection of both velocity and charge is equivalent to mass selection. The mass-velocity characteristic of the electrostatic accelerator is governed by the conservation of energy equation  $1/2 m v^2 = q V_a$ , where  $m$  is the mass of the particle,  $v$  is the particle velocity, and  $V_a$  is the accelerating voltage. From this,  $m = 2 q V_a / v^2$ . Therefore, if both  $q$  and  $v$  are constrained to lie within some predetermined limits, then  $m$  must also lie within some specified range.

When both charge and velocity selection is employed, the three output pulses from the Time Interval Selector are inhibited by control gates under control of a coincidence gate unless the particle charge lies within the preselected limits. If the selected charge is found to exist

at the time a particle passes position  $X_1$ , the charge selector puts out an output pulse. If the Time Interval Selector has found that the same particle meets the transit time requirements then it begins its sequence of three output pulses. The first pulse occurs at the time the particle is at position  $X_1$  and will therefore be in coincidence with the output pulse from the charge selector. The coincidence gate will then fire thereby activating the control gates for the Time Interval Selector output pulses. These three pulses then pass through and perform the previously described functions. The net effect of the system is a particle beam at the area of the target chamber having closely controlled mass and velocity limits.

## 2.2 The Linear Accelerator

A TRW-developed linear accelerator (linac) has been used for most of the data which will be presented later<sup>5,6</sup>. The advantage of the linac over the Van de Graaff accelerator is that a substantial increase in mass is realized from the additional acceleration voltage.

Figure 2-2 is a block diagram of the linac and its associated components. A particle exiting from the Van de Graaff accelerator passes first through the first and second detectors shown in the figure which comprise a time-of-flight range. The transit time of the particle is analyzed by a velocity (transit time) discriminator. If the detected charge signals have the preselected time separation they are allowed to pass through to the frequency generating system. This system converts the transit time information of the selected particle to a switching frequency to be applied to the drift tube structure of the linac. The output signals from the frequency generator are conditioned by several sets of electronics and are finally applied to the bus bars of the drift tube assembly as shown in the figure. Before acceleration begins, the entire structure is at ground potential. A delaying function in the frequency generator causes the first pulse to appear on the bus bars at the time the selected particle is in the central region of the first

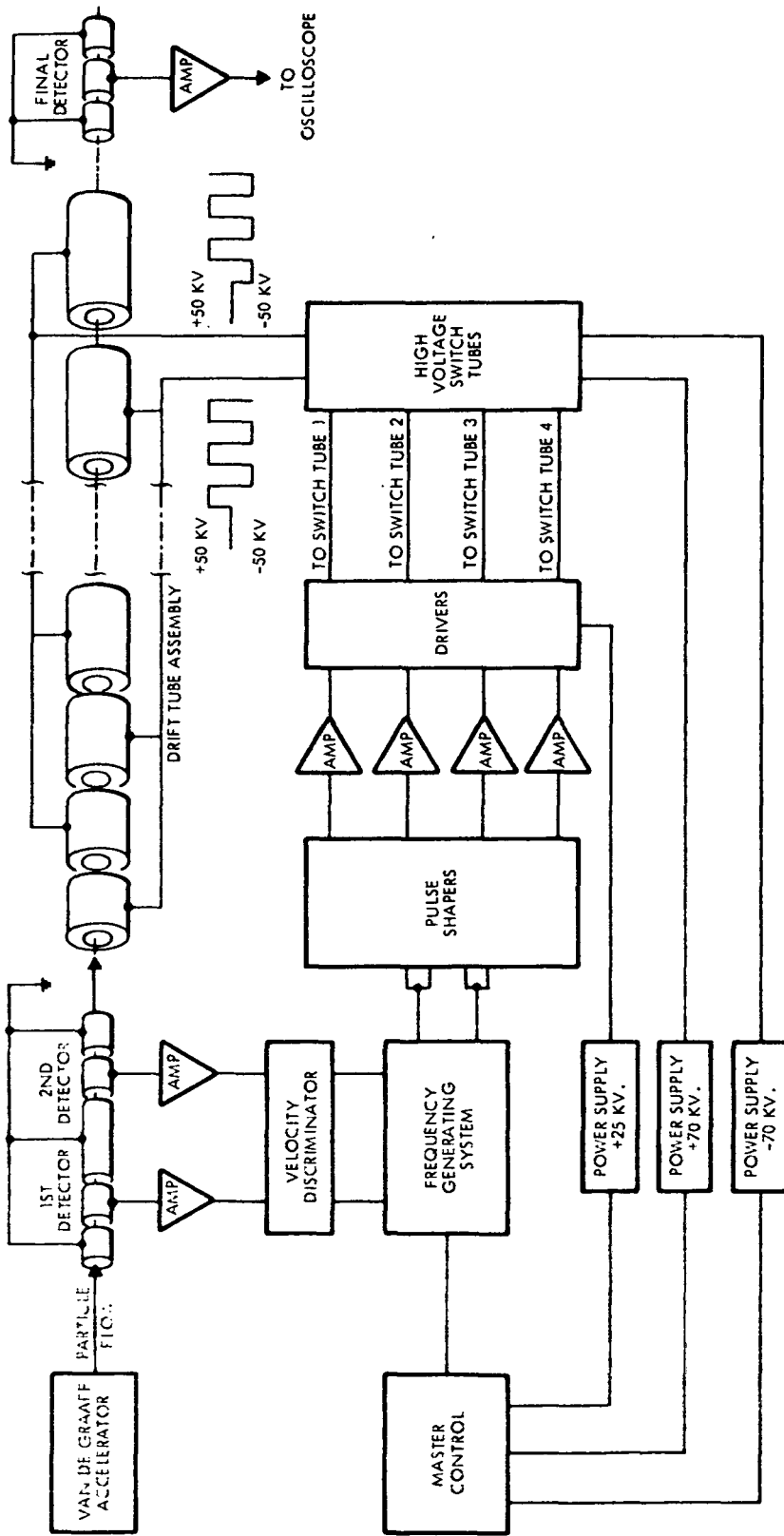


**FIGURE 2-2. Block Diagram of Linear Accelerator.** Particles from Van de Graaff pass through detectors 1 and 2 where transit time (velocity) is measured by velocity discriminator. Timing signals from particle falling within preset limits pass through to frequency generating system where appropriate switching frequency is generated. Output pulses are shaped, amplified, and presented to switch tubes which generate a high voltage rectangular wave. Wave is delayed and begins when particle is in center of first drift tube causing particle to be accelerated across gap #1 and gains 100 KV in accelerating voltage. Then reverses causing particle to be accelerated across gap #2, etc. Particle emerges from machine after 92 stages of acceleration and enters final position detector and target area (not shown) to right of figure. A proportionally delayed "acceleration completed" signal (not shown) triggers recording equipment as particle enters experimental area.

drift tube. As the particle emerges from the first tube it experiences an accelerating electric field due to the 100 kV potential existing between tubes 1 and 2 for the case illustrated in the figure. The switching frequency has been chosen so that the polarity of the potentials on the two rails will reverse when the particle is in the center of the second tube. This process then continues until the particle has traversed a total of 92 gaps. The total accelerating voltage is then the initial injection voltage of the Van de Graaff plus that obtained in traversing the 92 gaps of the linac.

When the linac is employed for high velocity impacts, the target chamber and the final position detector preceding the target chamber are removed from their position shown in Figure 2-1 and placed to the right of the diagram in Figure 2-2. The particle beam exiting from the selection apparatus previously described is then allowed to enter directly into the linac timing electronics. After the particle has undergone acceleration, a convenient timing signal (not shown in the figure) is provided by the frequency generating system which signals the time at which the particle will exit the linac and enter the final detector and target chamber.

Although the linac has a design goal of 10.8 million volts as the net accelerating voltage, it was limited for the purposes of this program to a net of approximately 6.0 million volts. Prior to its use on this program, the linac had sustained considerable damage to its internal drift tube structure due to high voltage arcing. A complete dismantling of the drift tube structure and polishing of all drift tubes was necessitated before the machine could be restored to service. This operation although not difficult is nevertheless time consuming. As a result, the linac was operated cautiously at a moderate voltage level so as not to risk a further delay which prolonged high voltage arcing might necessitate.

The penalty for the lower operating voltage was slightly less than a factor of 2 in particle radius at any given velocity. It can be shown that for constant surface field strength (a reasonable approximation for the contact charging method used) the particle radius varies directly as the accelerating voltage at any fixed velocity. Therefore, if the machine could have been operated at full potential the particle radius would have been larger by the ratio of 10.8/6.0. It was felt that the gain in particle size did not warrant the risk of possible further delays.

3.0 EXPERIMENTAL PROCEDURE3.1 The Target Chamber

Since the program required a large number of impacts at both normal and oblique incidence, a target chamber was used which would permit a change in impact targets as well as a change in the angle of impact while the target remained under vacuum.

Figure 3-1 illustrates the target chamber preceded by the final particle position detector. The chamber consists of an approximately four inch diameter pipe with ports mounted at right angles to the centerline through which the particles could pass. End flanges on the pipe provide support for an axially mounted rod which passes through O-ring seals in both end flanges. The center section of the rod was replaced by a mounting block machined with a flat surface sufficiently far off the axis of the rod so that a target could be mounted thereon and have its top surface lie on the centerline of the support rods. When mounted in this manner, the target can be rotated for oblique impacts without changing the impact point of the particle beam centerline. An angular index head (not shown) was affixed to the flange in the lower part of Figure 3-1 so that the angle of impact could be precisely determined.

A change in position upon the target surface or a complete change in targets could be accomplished by axially sliding the rod. The external portion of the rod in the lower part of the figure was scribed with position indexes. Corresponding index marks upon the flat mounting surface of the target holder permitted correlation of impact points upon the target surface with the external index marks. The impact position could then be read easily from outside while changing the impact site.

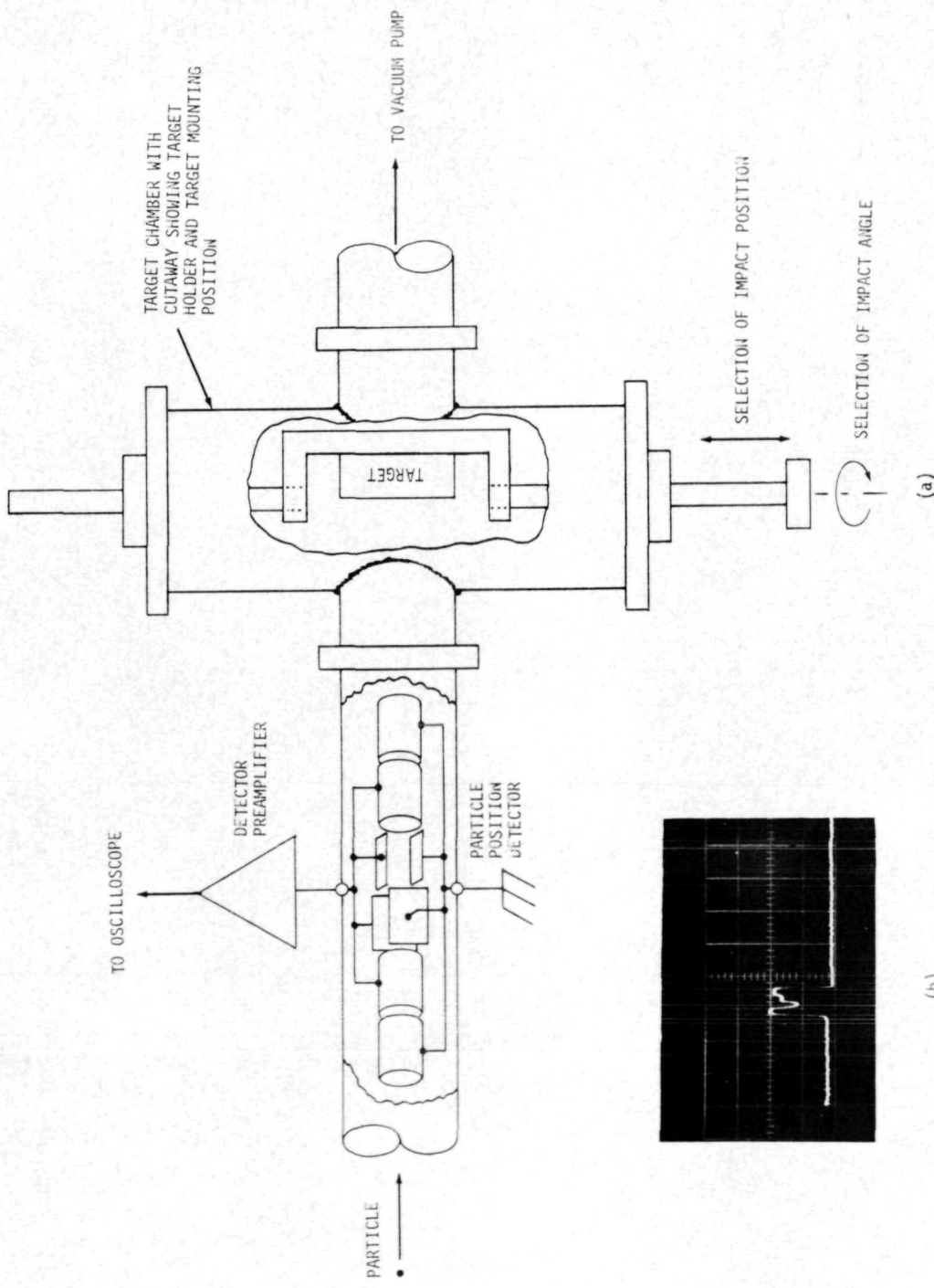


FIGURE 3-1. Diagram of Particle Position detector and Target Chamber. In (a) the cutaway view of the particle position detector shows schematically the internal geometry and electrical connections. A particle passing through the detector generates a signal similar to the oscilloscope trace shown in (b) from which relative position within an 0.25 inch diameter circle can be determined. Particles emerging from this detector proceed unobstructed to impact target shown in cutaway view of target chamber. Impact position is changed by axial motion of rod while impact angle is modified by rotation of rod. External index marks (not shown) show impact angle and position of target.

3.2 Identification of Impact Craters

Correlation of individual impact craters with the impacting particle and measurement of the particle parameters just prior to impact is accomplished by use of the particle position detector shown in Figure 3-1. This detector is located in close proximity to the impact target surface.

As can be seen from the figure, a particle traversing the detector from left to right first passes through two tubes, the first of which is grounded and the second which is electrically connected to the input of a sensitive preamplifier. The particle then traverses a set of parallel plates one of which is grounded while the second is connected to the amplifier input. This set of parallel plates is followed by a second set of plates mounted orthogonal to the first set and connected in the same manner. The particle then passes through a third tube which is connected to the amplifier input and finally out through a fourth tube which is grounded.

While the charged particle is traversing one of the tubes essentially all the particle charge is induced on that tube. When traversing a set of plates the induced charge is determined by the proximity to a given plate. When the particle passes near the surface of the active plate essentially all the charge is induced on the active member and virtually zero on the grounded member. When it passes near the grounded member the converse is true. Therefore, the geometry shown forms a detector which is capable of indicating the relative coordinates of a particle which traverses its length. A typical oscilloscope waveform is shown in Figure 3-1b. Passage of the particle through the detector guarantees impact upon the target surface.

The transit time through the detector provides a means of determining the impact velocity while the magnitude of the charge signal determines the total particle charge. Hence, the mass of the particle

may be calculated from a knowledge of the velocity, charge, and accelerating voltage. Since the particle material is generally known, and therefore the material density, an apparent radius may also be calculated. This calculated radius is quite accurate for spherical particles, but subject to considerable error for irregularly shaped particles as will be shown later.

### 3.3 Data Acquisition Procedures

Two different approaches were used to obtain the cratering data. The first approach was on a statistical basis. For these experiments the Van de Graaff accelerator was utilized which has a relatively high flux (several per minute) throughout most of the velocity range of interest. The particle parameter selection equipment previously described was then used to limit the particles striking the target. The boundary limits used were typically  $\pm 5$  percent on impact velocity, and  $\pm 10$  percent on particle charge which is equivalent to  $\pm 20$  percent on particle mass.

Typically, several hundred particles having closely controlled parameters would be allowed to impact in a selected target area. Such a large number of craters located in a small area (5 millimeters<sup>2</sup> or less) are relatively easy to find. Crater parameters are then obtained by selecting several craters arbitrarily and measuring these to obtain average characteristics. Likewise, a large number of the impacting particles may be measured during the bombardment phase to obtain average particle characteristics.

Most of the data to be presented were obtained using the linear accelerator which provides about a factor of four increase in particle diameter over that obtained from the Van de Graaff at any given velocity. The linear accelerator is a single shot device with a maximum repetition rate of about one per minute. Since a large number of craters would be

necessary for the statistical approach requiring long accelerator running times, it was felt that less time would be required if each individual crater was correlated with the particular impacting particle which formed it. This technique uses more search time in locating each crater, but is more than offset by the savings made in accelerator running time. In addition, the exact parameters of the particle and resulting crater would be known.

Typically, the procedure was to impact about three particles into each one-quarter inch square site on the target. The coordinate or position information available from the oscilloscope trace of the final particle position detector was then used to correlate the craters found with the impacting particles. Although the particle beam diameter is one-quarter inch where it strikes the target, the approximate position of the crater can be located within about a one millimeter diameter area by using the information obtained from the particle position detector.

All craters formed from particles accelerated by the linac were located by use of an optical microscope and the approximate coordinates obtained from the particle position detector signal. After all impacts were correlated with the corresponding particle detector signal, the craters so located were subsequently marked with small droplets of RTV silicon rubber. When marked in this manner, the approximate location of each crater could be easily found by the Scanning Electron Microscope (SEM) microscopist.

### 3.4 The Target Material

Except for a few craters in each of several miscellaneous minerals to be described later, all data were obtained using targets cut from a piece of oligoclase single crystal originally measuring about 2.5 x 3 x 9 cm. This sample was No. MLQ-10-67 from Muskwa Lake, Ontario, Canada and was supplied for use on the subject program by Dr. E. C. T. Chao of the U. S. Geological Survey.

The oligoclase sample was first encapsulated in epoxy in order to provide strength for the thin target specimens which would be sliced from the crystal. A total of seven slices having a thickness of approximately 2.5 millimeters were cut from the sample with the cut running parallel to the (010) face. This face was clearly shown on the sample by the trace of the composition plane of the albite twinning. Five of these seven targets were used for data appearing later in this report and have been given the code designation of S2, S3, S4, S5, and S6. These five targets then have impact surfaces which are parallel to (010).

In order to vary crystal orientation, two other target specimens were cut from the sample. The first of these with the code designation S10 was cut parallel to the prominent cleavage face (001). The second was cut from the sample at approximately 45° to both (010) and (001) and parallel to the line of intersection of (010) and (001). This target has been given the designation S9.

These specimens were then metallurgically polished through several steps with the final step using 0.05 micron abrasive compound. In order to facilitate identification of target impact sites for the bombardment phase and for the photographic phase, the polished surface of each specimen was ruled with lines at one-quarter inch intervals with a diamond scribe to form one-quarter inch square impact sites. Generally, 20 impact sites were obtained in this manner on each of the previously described targets. For ease of identification, each of the squares obtained were numbered by scribing the surface. With each target marked in this manner, it is relatively easy for the microscopist to determine his viewing position upon the surface, or conversely, to locate a particular crater upon the surface when given the site number and relative coordinates within the site.

Our first attempt at crater location using an optical microscope was only partially successful. It was found that the oligoclase is semi-transparent in thin sections and is filled with numerous color centers which hampered location of the damage site created by an impacting particle. At high magnification (100x to 500x) the surface was difficult to find even where a rough texture existed. As a result, craters on the first impact specimen could only be found where a large amount of surface damage resulted from the impact. This occurs only at relatively low velocities where large particles are available.

To circumvent this difficulty, the target surface was coated with a 100 to 125 Å film of aluminum by using vacuum deposition. At this thickness, aluminum films transmit only about 10 percent of the incident light at a wavelength of 5000 Å<sup>7</sup>. By bottom lighting the sample, any break in the film could be detected with relative ease and yet the film was still sufficiently thin to allow the underlying mineral structure to be viewed if desired. It is felt that the 125 Å film of aluminum does not materially change the cratering characteristics of the impacting particles since this thickness represents only about 5 percent of the diameter of the smallest particle observed in the reported data.

In addition to the oligoclase, six other minerals were bombarded during the course of the program. Targets were cut from the minerals without regard to crystal orientation and were metallurgically polished by the same procedures used for the oligoclase targets. The exception to this was biotite mica which was cleaved along a cleavage plane in order to obtain a smooth surface for impact. Since the targets would be bombarded with a large number of particles in a small area and the craters could therefore be easily found, the aluminum coating was not required and was therefore not used.

The minerals used and their sources were as follows: Biotite Mica from Silver Crater, Haliburton County, Ontario, Canada; Diopside from Yates Mine near Otter Lake, Quebec, Canada; Hedenbergite from

Yerington, Nevada; Ilmenite from near St. Urbain, Quebec, Canada; Monticellite from Crestmore Quarry near Riverside, California; and Orthoclase--source unknown.

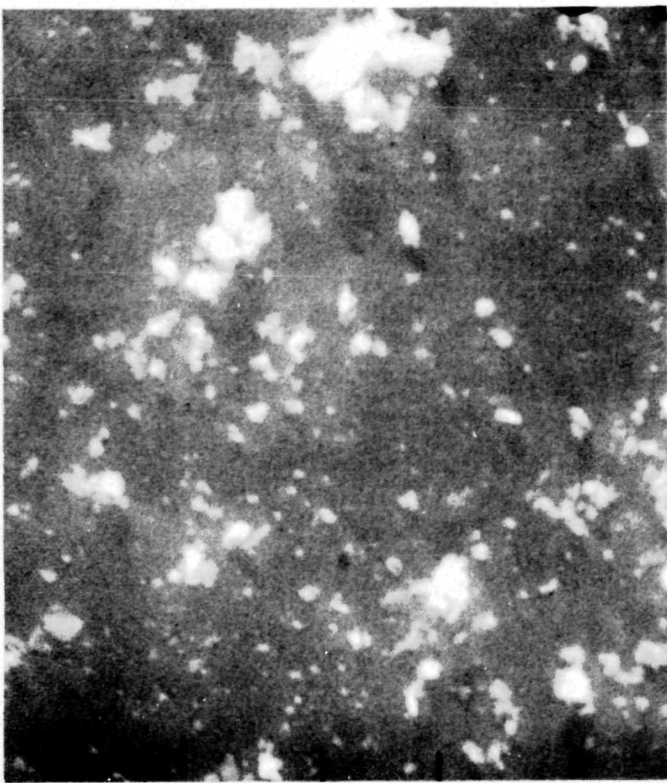
### 3.5 Particle Materials

The particle materials used to obtain the reported data were iron, lanthanum hexaboride ( $\text{LaB}_6$ ), and silicon. SEM photographs of these three materials are shown in Figure 3-2.

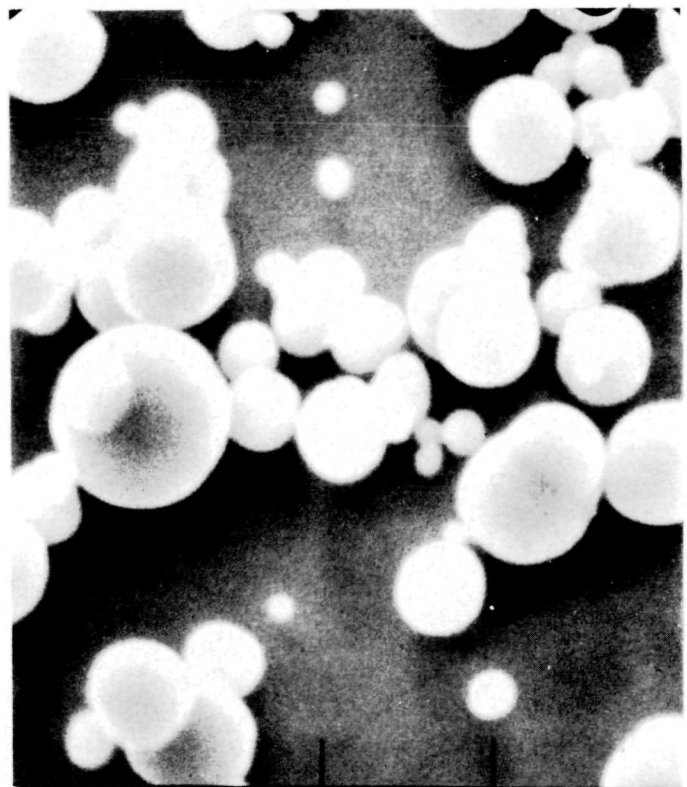
Figure 3-2a shows the iron particles with index marks spaced at 2 microns separation. This material is commonly referred to as carbonyl iron powder obtained from General Aniline and Film Corporation. The manufacturers specifications are 98% iron (minimum), 0.8% carbon (maximum), and 1.2% oxygen and nitrogen (maximum). The material density is assumed to be that of pure iron,  $7.8 \text{ gm/cm}^3$ . These particles are formed by depositing iron from a vapor state, and hence form quite spherical particles which are particularly well suited for electrostatic acceleration.

Figure 3-2b is an SEM photograph of the silicon powder which was used. The spacing of the index marks is 5 microns. This material was obtained from Cerac, Incorporated of Butler, Wisconsin. The manufacture of the particles is a proprietary process of Cerac, but apparently involves some form of grinding procedure since the particles can be seen to be quite irregular in shape. An irregular shape factor is unfortunate for cratering studies since the geometry of the impacting particle is never known very well. The material density is assumed, for apparent radius calculations, to be that of pure silicon,  $2.33 \text{ gm/cm}^3$ .

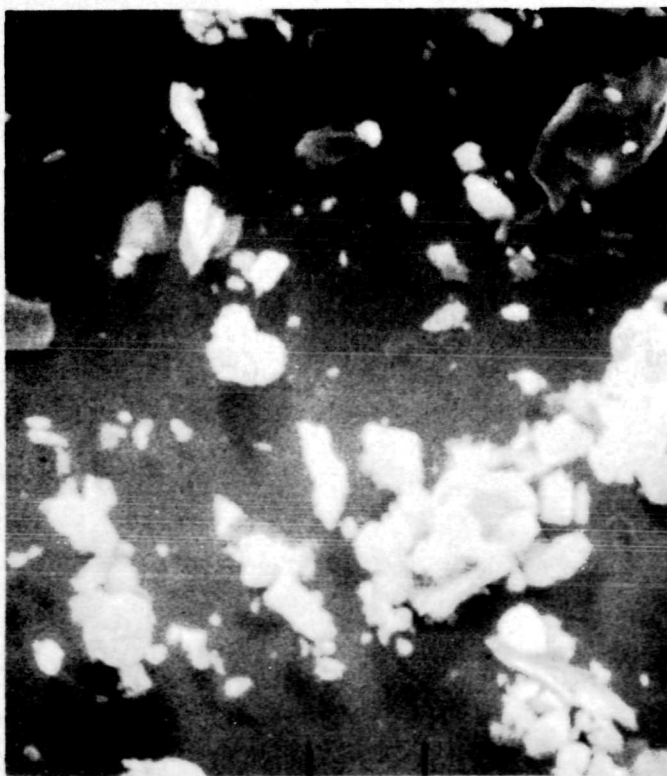
Figure 3-2c is an SEM photograph of the lanthanum hexaboride particles. Index marks are shown at 5 microns separation. This material was also obtained from Cerac and is similar in shape to the silicon. The density of the particle material is assumed to be  $2.61 \text{ gm/cm}^3$  for apparent radius calculations.



(b)



(a)



(c)

FIGURE 3-2.

SEM Photographs of Iron, Silicon, and Lanthanum Hexaboride Particles. Spherical iron particles are shown in (a) with index marks at 2 micron separation. Silicon particles are shown in (b) and Lanthanum hexaboride in (c) with index marks at 5 microns separation

## 4.0 EXPERIMENTAL RESULTS

### 4.1 Quantitative Data on Cratering Parameters

#### 4.1.1 Iron Particle Impacts on Oligoclase and Miscellaneous Minerals

##### 4.1.1.1 Normal Impacts on Oligoclase

In order to convey as much of the program results as possible to the interested reader, all numerical cratering data and associated particle parameters have been tabulated in addition to certain graphical presentations to follow. These are presented below.

The data obtained for normal impacts of iron particles on oligoclase are presented in Tables 1 and 2. Table 1 contains data from individually correlated particle and crater combinations while that in Table 2 is the result of a statistical approach where average characteristics at a fixed velocity are found. Table 2 will be included in the next section along with data from several other mineral specimens having the same particle impact parameters.

The data in each table begins with a crater designation which is a code number identifying the particular crater being measured. For example, the first line in Table 1 is for crater number S4-13-C. The number states that this is crater C in site number 13 located on Target S4. The crater designation numbers have been included so that numerical data may be readily found for each of the many crater photographs found later in this report.

Table 1 contains data for normal impact of iron particles on oligoclase where each crater has been correlated with the particle which formed it. In this case, individually calculated values are obtained for the velocity, mass and radius of the impacting particle. The data are listed in the order of increasing velocity.

TABLE 1  
DATA FOR NORMAL IMPACTS OF IRON PARTICLES ON OLIGOCLASE

Crater Designation	PARTICLE DATA			CRATER DIMENSIONS			NORMALIZED DIMENSIONS		
	Velocity km/s	Mass x 10 <sup>-14</sup> kgm	Radius (microns)	Central Pit Dia (microns) Max.	Spall Dia (microns) Max.	Pit Dia/ Particle Dia (D <sub>p</sub> /d)	Spall Dia/ Particle Dia (D <sub>s</sub> /d)	Max.	Min.
S4-13-C	2.75	9.21	1.41	2.9	2.8	22	19	1.03	.99
S4-13-D	2.86	18.0	1.76	3.7	3.4	54	33	1.1	.97
S4-13-B	3.08	24.6	1.95	4.3	4.1	52	28	1.1	1.1
S4-13-A	3.33	5.23	1.17	2.8	2.6	16	16	1.2	1.1
S4-14-B	4.09	8.71	1.38	3.2	2.9	30	18	1.2	1.1
S4-14-A	4.39	13.3	1.59	3.4	3.1	34	31	1.1	.97
S4-15-B	4.44	10.3	1.46	3.3	3.1	57	31	1.1	1.1
S4-15-A	4.82	9.27	1.41	3.1	3.0	38	26	1.1	1.1
S4-14-D	5.36	3.50	1.02	2.5	2.5	22	14	1.2	1.2
S4-15-C	5.47	3.76	1.05	2.6	2.6	22	14	1.2	1.2
S3-1-A	6.03	2.01	.848	1.6	1.6	9.7	9.7	.94	.94
S4-15-D	6.16	2.69	.935	2.5	2.3	21	14	1.3	1.2
S3-17-C	6.90	1.69	.800	1.8	1.7	13	7.5	1.1	1.06
S3-1-C	6.99	1.48	.765	1.6	1.5	12	11	1.05	.98
S4-14-C	7.11	.854	.638	1.3	1.3	9.9	8.3	1.02	1.08
S3-1-B	7.21	.720	.602	1.1	1.0	Cracks	.91	.83	Cracks
S3-17-D	7.26	1.00	.672	1.8	1.6	Undetermined	1.3	1.2	Undetermined
S3-17-B	7.53	.722	.603	1.4	1.3	Cracks	1.2	1.07	Cracks
S3-17-A	7.87	.610	.570	1.2	1.2	"	1.05	1.05	"
S3-2-A	8.35	1.13	.699	1.6	1.4	"	1.1	1.05	"
S3-18-B	8.74	.376	.485	1.0	.97	"	1.03	1.00	"
S3-18-A	9.37	.286	.443	.94	.91	No Spall	1.2	1.1	No Spall
S3-2-C	9.59	.169	.372	.91	.83	"	1.8	1.4	"
S3-2-B	10.6	.324	.462	1.7	1.3	"	1.1	1.05	"
S3-19-A	11.4	.114	.326	.73	.69	"	1.1	1.05	"
S3-3-A	11.5	.0470	.243	.87	.73	Spall?	1.8	1.5	Spall?

Since the crater pit and spall area are not generally circular, a minimum and a maximum diameter are listed for each. The minimum and maximum diameters for the central pit and the spall area were normalized to the calculated diameter of the impacting particle and are listed in the rightmost four columns of the table.

A general characteristic of electrostatic particle accelerators may be seen in this and other tables to follow which is that mass and radius decrease with increasing particle velocity. Note also in the column of normalized dimensions for  $D_s/d$  that observable spallation ceases for the impacts tabulated around 7 km/s and that only cracks are observed at higher velocities.

The data in Table 1 are presented graphically in Figure 4-1. The figure is a plot of crater diameter normalized to particle diameter vs particle velocity. The triangular data points are the data from Table 1. The light triangles nearer the bottom of the figure are for the normalized central pit diameter ( $D_p/d$ ) while the darker triangles nearer the top of the figure are for the normalized spall diameter ( $D_s/d$ ). In each case, a maximum and a minimum value have been plotted and connected with a vertical bar. The circular data points are for average normalized pit and spall diameter from 6 impacts in oligoclase at 3.06 km/s. These data will be presented in Table 2 but are included on this graph since the data are for normal impacts of iron particles on oligoclase. The average mass of a particle in this set is  $2.24 \times 10^{-14}$  kgm which is about 1/10 the mass of the particle in Table 1 at 3.08 km/s. Since a slightly smaller  $D_p/d$  and  $D_s/d$  ratio are obtained a possible size effect is indicated.

Impacts which produced cracks without spallation have been so indicated by a circle with enclosed dot appearing at the appropriate velocity near the bottom of the figure. Likewise, craters without spallation or visible cracks are indicated by a small square placed at the impact velocity.

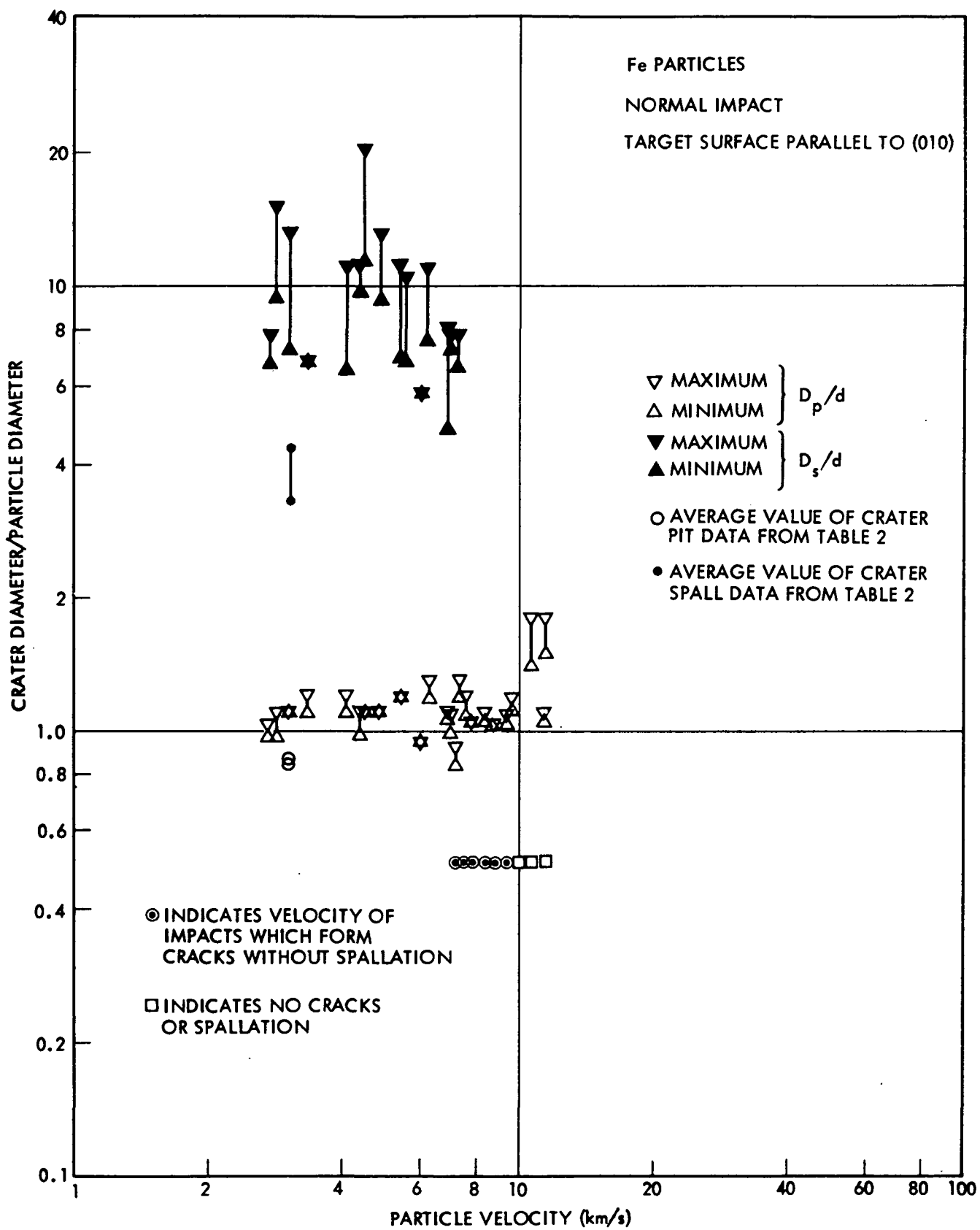


FIGURE 4-1. Crater Diameter/Particle Diameter vs Particle Velocity for Normal Impact of Iron Particles on Oligoclase. Normalized central pit diameter ( $D_p/d$ ) is plotted in the lower part of figure while normalized spall diameter ( $D_s/d$ ) is plotted in the upper part of figure.

#### 4.1.1.2 Normal Impacts on Miscellaneous Minerals

Several different minerals including oligoclase were bombarded with particles having closely controlled parameters in order to obtain average characteristics at a fixed mass and velocity. The particle selection and data acquisition procedures were previously described in Sections 2.1 and 3.3.

A total of seven different minerals were impacted with particles at about 3 km/s. These target materials and their source were described in Section 3.4. In each case, the selected impact site was bombarded with approximately 500 particles. Particle transit time and charge were recorded on 15 to 20 particles out of each set of about 500. The particles recorded were photographed at arbitrary intervals throughout the bombardment phase on each of the seven minerals. In this manner, a total of 125 particle detector waveforms were recorded each of which provided sufficient information to calculate the mass and velocity of the particular particle photographed. These recorded data were assumed to represent a good statistical sampling of the impacting particles for the seven mineral samples.

The calculated average velocity for the 125 events is  $3.06 \pm .11$  km/s where the error shown is  $\pm$  one standard deviation. The maximum recorded velocity for the set was 3.45 km/s and the lowest recorded velocity was 2.83 km/s. The calculated average mass for the set is  $(2.24 \pm .24) \times 10^{-14}$  kg. The maximum calculated mass was  $2.83 \times 10^{-14}$  kg while the lowest was  $1.59 \times 10^{-14}$  kg. The calculated average radius for the particles is  $0.88 \pm .03$  microns. The highest calculated radius was 0.936 microns and the lowest was 0.786 microns. The error limits given on mass and radius are also  $\pm$  one standard deviation.

Table 2 contains the data for normal impacts of iron particles on oligoclase. Six craters were photographed and measured. The columnar data are in the same format as that used for Table 1 with the exception

TABLE 2  
DATA FOR NORMAL IMPACTS OF IRON PARTICLES ON OLIGOCLASE

Crater Designation	PARTICLE DATA			CRATER DIMENSIONS			NORMALIZED DIMENSIONS		
	Velocity km/s	Mass $\times$ $10^{-14}$ kgm	Radius (microns)	Central Dia (microns) Max.	Pit Dia (microns) Min.	Spall Dia (microns) Max.	Pit Dia/ Particle Dia ( $D_p/d$ ) Max.	Spall Dia/ Particle Dia ( $D_s/d$ ) Max.	Spall Dia/ Particle Dia ( $D_s/d$ ) Min.
S5-3-1				1.5	1.5	6.5	.85	.85	3.7
S5-3-2				1.4	1.4	8.3	.80	.80	4.7
S5-3-3	3.06±.11	2.24±.24	.88±.03	1.6	1.5	7.4	.91	.85	4.3
S5-3-4				1.5	1.5	9.4	6.6	.85	5.3
S5-3-5				1.6	1.5	5.4	5.0	.85	3.1
S5-3-6				1.6	1.6	7.7	6.5	.91	4.4
Average Values				1.5	1.5	7.5	.87	.85	3.3

that average values are listed for each. Tables 3, 4, 5, and 6 contain similar data for normal impacts of iron particles on diopside, biotite mica, hedenbergite, ilmenite, monticellite, and orthoclase. In each case average values are listed for  $D_p$ ,  $D_s$ ,  $D_p/d$ , and  $D_s/d$ . Table 6A summarizes the average values found for each of the seven minerals bombarded. For each mineral, the published values for specific gravity and hardness are shown.<sup>8</sup> The hardness values are for Moh's scale.

#### 4.1.1.3 Oblique Impacts on Oligoclase

The data acquired for 30° to normal oblique impacts of iron particles on oligoclase are presented in Tables 7 and 8. The first table is the data collected at 3.06 km/s. The impacting particles in this group have the same parameters as those used for the bombardment of the miscellaneous minerals listed above. As before, six craters were photographed and measured to obtain the values shown for the central pit and spall data. Again, average value for each column is shown near the bottom. Since oblique impacts result in elongated craters, the measured values of the central pit diameter and the spall diameter have been made along the direction of impact (length) and perpendicular to the direction of impact (width).

Table 8 contains data for 30° to normal oblique impacts where each individual crater was correlated with the particle which formed it. The data are arranged in ascending order of impact velocity and extends from 2.45 to 27.9 km/s.

The values for  $D_p/d$  and  $D_s/d$  in Tables 7 and 8 are presented graphically in Figure 4-2 plotted vs particle impact velocity in the same manner as was done for the normal impacts of Figure 4-1. Note that all impacts obtained produced spallation at 30° to normal while the normal impacts obtained above 7.5 km/s produced no spallation. The triangular data points are the data from Table 8 while the circular data points are the data from Table 7.

TABLE 3  
DATA FOR NORMAL IMPACTS OF IRON PARTICLES ON DIOPSIDE

Crater Designation	PARTICLE DATA			CRATER DIMENSIONS				NORMALIZED DIMENSIONS			
	Velocity km/s	Mass $\times$ $10^{-14}$ kgm	Radius (microns)	Central Pit Dia (microns)	Spall Dia (microns)	Pit Dia/ Particle Dia (D <sub>p</sub> /d)	Spall Dia/ Particle Dia (D <sub>s</sub> /d)	Particle Dia (D <sub>s</sub> /d)	Max.	Min.	Max.
D-1				1.9	1.8	5.1	4.1	1.08	1.02	2.9	2.3
D-2				1.9	1.7	4.6	3.9	1.08	.97	2.6	2.2
D-3				1.6	1.5	4.2	3.6	.91	.85	2.4	2.0
D-4				2.0	1.9	5.1	4.3	1.1	1.08	2.9	2.4
D-5				1.7	1.6	6.1	5.0	.97	.91	3.5	2.8
D-6	3.06±.11	2.24±.24	.88±.03	2.1	2.1	5.5	4.7	1.2	1.2	3.1	2.7
D-7				1.9	1.8	6.2	5.4	1.08	1.02	3.5	3.1
D-8				2.1	1.9	4.9	3.2	1.08	1.02	2.8	1.8
D-9				2.0	1.7	4.7	4.4	.97	1.1	2.7	2.5
D-10				1.9	1.8	6.4	6.3	1.08	1.02	3.6	3.6
D-11				1.9	1.9	6.5	5.9	1.08	1.08	3.7	3.4
D-12				1.9	1.9	6.9	5.8	1.08	1.08	3.9	3.3
Average Values				1.9	1.8	5.5	4.7	1.06	1.04	3.1	2.7

TABLE 4  
DATA FOR NORMAL IMPACTS OF IRON PARTICLES ON BIOTITE MICA AND HEDENBERGITE

Crater Designation	Velocity km/s	Mass x 10-14 kgm	Radius (microns)	CRATER DIMENSIONS				NORMALIZED DIMENSIONS			
				Max.	Min.	Central Pit Dia (microns)	Spall Dia (microns)	Pit Dia/ Particle Dia (D <sub>p</sub> /d)	Spall Dia/ Particle Dia (D <sub>s</sub> /d)	Max.	Min.
<u>BIOTITE MICA</u>											
B-1				2.5	2.5	6.1	6.0	1.4	1.4	3.5	3.4
B-2				2.2	2.1	5.6	5.5	1.3	1.2	3.2	3.1
B-3	3.06±.11	2.24±.24	.88±.03	2.3	2.3	5.6	4.7	1.3	1.3	3.2	2.7
B-4				2.5	2.4	6.1	5.0	1.4	1.4	3.5	2.8
B-5				2.2	2.1	6.3	5.2	1.3	1.2	3.6	3.0
B-6				2.5	2.5	5.9	5.5	1.4	1.4	3.4	3.1
Average Values				2.4	2.3	5.9	5.3	1.4	1.3	3.4	3.0
<u>HEDENBERGITE</u>											
H-1				1.5	1.4	6.5	5.6	.85	.80	3.7	3.2
H-2				2.0	1.4	8.0	5.9	1.1	.80	4.6	3.4
H-3	3.06±.11	2.24±.24	.88±.03	1.6	1.4	9.2	8.1	.91	.80	5.2	4.6
H-4				1.6	1.5	7.5	6.8	.91	.85	4.3	3.9
H-5				1.5	1.4	8.2	7.2	.85	.80	4.7	4.1
H-6				1.2	1.2	6.7	5.4	.68	.68	3.8	3.1
Average Values				1.6	1.4	7.7	6.5	.88	.79	4.4	3.7

TABLE 5  
DATA FOR NORMAL IMPACTS OF IRON PARTICLES ON ILMENITE

Crater Designation	PARTICLE DATA			CRATER DIMENSIONS			NORMALIZED DIMENSIONS			
	Velocity (km/s)	Mass $\times$ $10^{-14}$ kgm	Radius (microns)	Central Pit Dia (microns)	Spall Dia (microns)	Pit Dia/ Particle Dia (D <sub>p</sub> /d)	Spall Dia/ Particle Dia (D <sub>s</sub> /d)	Particle Dia (D <sub>s</sub> /d)	Min.	Max.
I-1				2.1	1.7	3.2	2.7	1.2	.97	1.8
I-2				1.9	1.9	5.6	4.4	1.08	1.08	3.2
I-3				2.1	1.9	6.5	3.2	1.2	1.08	3.7
I-4	$3.06 \pm .11$	$2.24 \pm .24$	$.88 \pm .03$	1.9	1.7	4.5	3.7	1.08	.97	2.6
I-5				2.1	1.9	4.7	4.6	1.2	1.08	2.7
I-6				2.1	1.5	4.8	3.6	1.2	.85	2.7
I-7				2.1	1.9	4.2	3.2	1.2	1.08	2.4
Average Values			2.0	1.8	4.8	3.6	1.2	1.02	2.7	2.0

TABLE 6  
DATA FOR NORMAL IMPACTS OF IRON PARTICLES ON MONTICELLITE AND ORTHOCLASE

Crater Designation	PARTICLE DATA			CRATER DIMENSIONS			NORMALIZED DIMENSIONS		
	Velocity (km/s)	Mass $\times$ $10^{-14}$ kgm	Radius (microns)	Central Pit Dia (microns)	Spall Dia (microns)	Particle Dia (D <sub>p</sub> /d)	Pit Dia/ Particle Dia	Particle Dia (D <sub>s</sub> /d)	Min.
<u>MONTICELLITE</u>									
M-1			1.9	1.9	6.3	6.0	1.08	1.08	3.6
M-2			1.9	1.9	6.5	5.3	1.08	1.08	3.7
M-3	3.06±.11	2.24±.24	.88±.03	1.7	4.3	3.8	.97	.97	3.0
M-4			2.0	1.9	7.2	4.2	1.1	1.08	4.1
M-5			1.9	1.7	7.9	4.1	1.08	.97	4.5
M-6			Undetermined	Undetermined	Undetermined	Undetermined	Undetermined	Undetermined	Undetermined
<u>ORTHOCLASE</u>									
0-1			1.4	1.4	7.1	5.2	.80	.80	4.0?
0-2			1.8	1.6	9.0	8.9	1.02	.91	5.1
0-3	3.06±.11	2.24±.24	.88±.03	1.5	1.5	12	9.9	.85	6.8
0-4			1.6	1.5	12	8.9	.91	.85	5.1
0-5			1.5	1.5	10.1	9.9	.85	.85	5.7
0-6			1.8	1.7	9.5	8.9	1.02	.97	5.4
<u>Average Values</u>									
			1.6	1.5	10.0	8.6	.91	.87	5.6
									4.9

TABLE 6A

## AVERAGE VALUES OF DATA FOR NORMAL IMPACTS OF IRON PARTICLES ON MISCELLANEOUS MINERALS

Mineral	Mineral Data <sup>8</sup>		Crater Dimensions				Normalized Dimensions			
	Specific Gravity	Hardness	Central Pit Dia (microns)	Spall Dia (microns)	Pit Dia/Particle Dia (D <sub>p</sub> /d)	Spall Dia/Particle Dia (D <sub>s</sub> /d)	Max.	Min.	Max.	Min.
Oligoclase	2.63-2.65	6-6.5	1.5	1.5	7.5	5.7	.87	.85	4.3	3.3
Diopside	3.22-3.38	5.55-6.5	1.9	1.8	5.5	4.7	1.06	1.04	3.1	2.7
Biotite Mica	2.7-3.3	2.5-3	2.4	2.3	5.9	5.3	1.4	1.3	3.4	3.0
Hedenbergite	3.50-3.56	6	1.6	1.4	7.7	6.5	.88	.79	4.4	3.7
Ilmenite	4.68-4.76	5-6	2.0	1.8	4.8	3.6	1.2	1.02	2.7	2.0
Monticellite	3.08-3.27	5.5	1.9	1.8	6.4	4.7	1.06	1.04	3.7	2.7
Orthoclase	2.55-2.63	6-6.5	1.6	1.5	10.0	8.6	.91	.87	5.6	4.9

TABLE 7  
DATA FOR 30° OBLIQUE IMPACTS OF IRON PARTICLES ON OLIGOCLASE

Crater Designation	PARTICLE DATA			CRATER DIMENSIONS			NORMALIZED DIMENSIONS		
	Velocity km/s	Mass $\times$ $10^{-14}$ kgm	Radius (microns)	Central Dia (microns)	Pit Dia (microns)	Span Width Length	Particle Dia (D <sub>p</sub> /d)	Pit Dia/ Particle Dia (D <sub>p</sub> /d)	Span Width Length Width
S5-2-1				2.2	1.5	5.8 6.2	1.3	.85	3.3 3.5
S5-2-2				2.2	1.6	5.8 4.2	1.3	.91	3.3 2.4
S5-2-3	3.06±.11	2.24±.24	.88±.03	2.5	1.6	5.8 Length	1.4	.91	3.3 3.3
S5-2-4				2.4	1.8	8.3 Width	1.4	1.02	4.7 3.1
S5-2-5				2.2	1.6	5.4 Length	1.3	.91	3.1 2.8
S5-2-6				2.1	1.5	5.4 Length	1.2	.85	3.1 2.6
Average Values									
	2.3	1.6	6.1	5.2	1.3		.91	3.5	3.0

TABLE 8  
DATA FOR 30° OBLIQUE IMPACTS OF IRON PARTICLES ON OLIGOCLASE

Crater Designation	PARTICLE DATA			CRATER DIMENSIONS				NORMALIZED DIMENSIONS			
	Velocity km/s	Mass $\frac{1}{2}$ 10 <sup>-14</sup> kgm	Radius microns	Central Length Width	Pit Length Width	Spall Length Width	Dia/ Width	Pit Dia/ Width	Particle Dia (D <sub>p</sub> /d)	Spall Dia (D <sub>s</sub> /d)	Particle Dia (D <sub>p</sub> /d)
S4-10-B	2.45	37.3	2.25	7.5	4.2	29	21	1.7	.93	6.4	4.7
S4-17-B	2.49	16.5	1.71	3.1	2.8	19	15	.91	.82	5.6	4.4
S4-10-A	2.52	6.81	1.27	3.3	2.1	8.1	8.0	1.3	.83	3.2	3.1
S4-17-E	2.84	7.06	1.29	2.5	2.1	6.3	5.2	.97	.81	2.4	2.0
S4-17-C	2.95	7.49	1.32	3.2	2.3	8.5	8.6	1.2	.87	3.2	3.3
S4-8-A	3.21	30.4	2.10	8.5	7.5	23	16	2.0	1.8	5.5	3.8
S4-3-A	4.22	11.4	1.51	6.4	4.1	22	20	2.1	1.4	7.3	6.6
S4-17-A	4.26	4.38	1.10	No	Pit	6.8	6.8	No	Pit	3.1	3.1
S4-17-D	4.35	8.11	1.35	5.6	3.4	24	29	2.1	1.3	8.9	11
S4-5-A	4.38	12.5	1.56	6.4	4.1	23	23	2.1	1.3	7.4	7.4
S4-3-B	4.91	7.87	1.34	4.9	3.8	23	17	1.8	1.4	8.6	6.3
S3-6-A	4.93	5.44	1.18	1.1	.88	5.9	6.9	.47	.37	2.5	2.9
S3-6-B	5.84	2.07	.856	2.5	1.6	9.7	7.8	1.5	.93	5.7	4.6
S3-6-C	5.93	3.68	1.04	4.2	3.4	14	12	2.0	1.6	6.7	5.8
S3-11-A	6.76	1.75	.810	2.6	1.7	5.9	11	1.6	1.05	3.6	6.8
S3-13-C	8.22	.345	.472	1.5	1.0	5.9	5.3	1.6	1.06	6.3	5.6
S3-13-B	8.35	.372	.483	1.6	1.1	4.7	5.3	1.7	1.1	4.9	5.5
S3-13-A	9.01	.342	.470	4.2	1.9	8.8	5.3	4.5	2.0	9.4	5.6
S3-10-A	12.0	.0352	.220	.74	.53	2.1	2.6	1.7	1.2	4.8	5.9
S3-15-B	13.1	.0823	.292	2.3	1.6	5.8	6.2	3.9	2.7	9.9	10.6
S3-15-A	14.7	.0631	.268	2.8	2.0	6.3	6.2	5.2	3.7	12.	12.
S4-1-C	23.4	.00983	.144	.49	.29	Spall?	1.7	1.01	Spall?	1.01	Spall?
S4-1-D	23.4	.00428	.109	1.3	.63	2.1	1.8	6.0	2.9	9.6	8.3
S4-1-E	27.9	.00338	.101	1.02	.45	2.3	1.8	5.0	2.2	11.	8.9

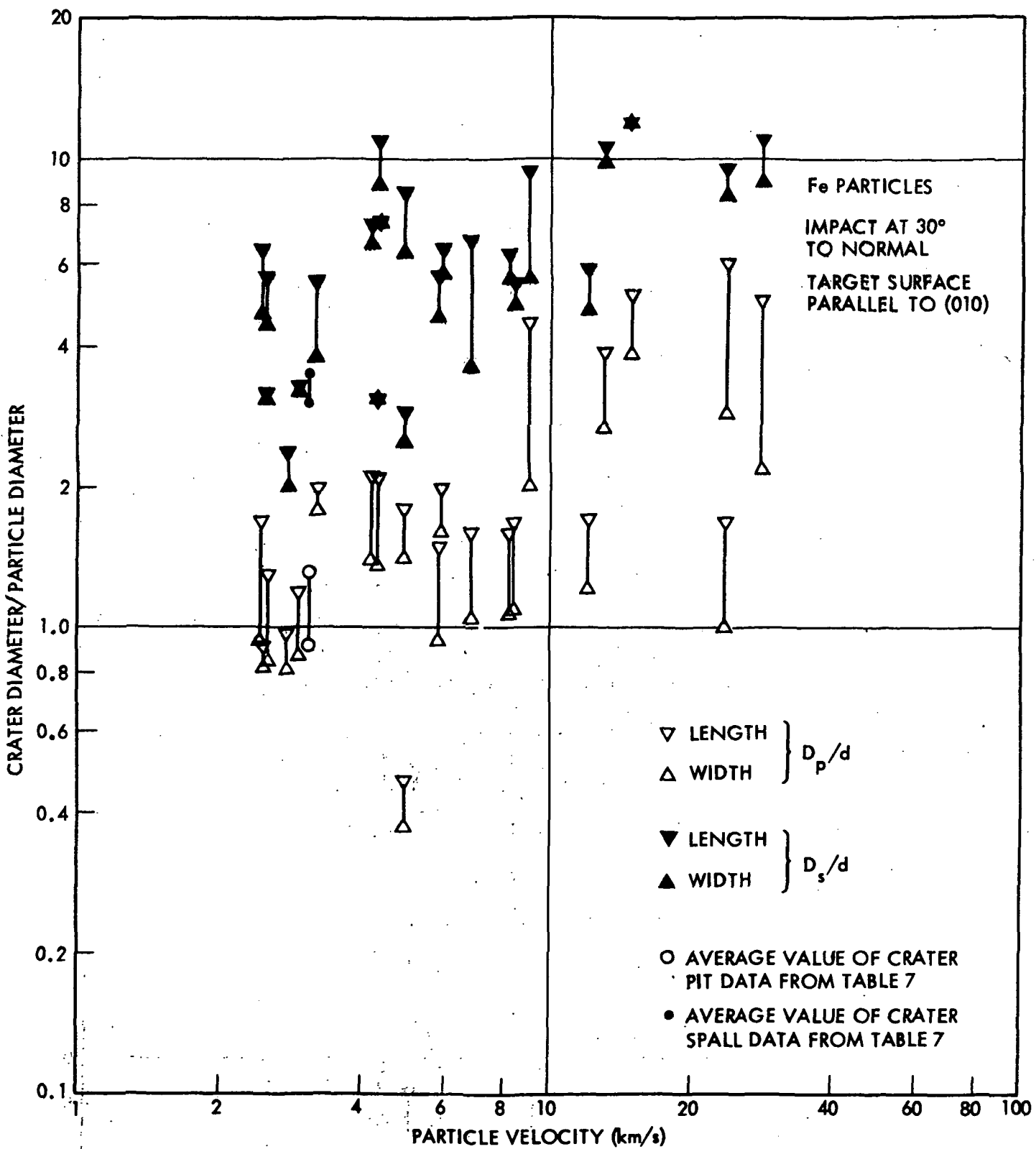


FIGURE 4-2. Crater Diameter/Particle Diameter vs Particle Velocity for 30° to Normal Impacts of Iron Particles on Oligoclase. Normalized central pit diameter ( $D_p/d$ ) is plotted in the lower part of figure while normalized spall diameter ( $D_s/d$ ) is plotted in the upper part of figure.

Tables 9 and 10 show the data obtained for 60° oblique impacts of iron particles on oligoclase. Table 9 shows the average data obtained for six measured craters at 3.06 km/s using the statistical approach previously described. The data in Table 10 are for craters which were individually correlated with the impacting particle which formed it. The table is arranged in ascending order of impact velocity as before.

The values for  $D_p/d$  and  $D_s/d$  in Tables 9 and 10 are presented graphically in Figure 4-3 in the same manner as was done for Figure 4-2. The triangular data points represent the data in Table 10 while the circular ones represent the data in Table 9. Note that spallation occurs for all impact velocities on this graph.

#### 4.1.2 Lanthanum Hexaboride Particle Impacts on Oligoclase

All lanthanum hexaboride particle impacts were obtained using the linear accelerator and a single shot approach. Each measured crater listed in Tables 11 and 12 has been individually correlated with the particle which produced it. The format of the data is the same as that used for the previously described iron particle impacts.

Table 11 is the data for normal impacts. The data are arranged in ascending order of impact velocity and extend from 1.46 to 22.9 km/s. The values found for  $D_p/d$  and  $D_s/d$  have been plotted vs particle impact velocity in Figure 4-4. As before the light triangles are for values of  $D_p/d$  while the dark triangles are for values of  $D_s/d$ . Impacts which did not produce observable spallation are so indicated by a small square located at the appropriate velocity. Note that a large number of these low density particles did not produce spallation.

The data for oblique impacts of lanthanum hexaboride particles are contained in Table 12. Only a limited number of oblique impacts were obtained due to an equipment failure in the particle accelerator facility. Time and budgetary limitations did not permit the bombardment phase with  $\text{LaB}_6$  particles to be extended once the facility had been restored to an operational status.

TABLE 9  
DATA FOR 60° OBLIQUE IMPACTS OF IRON PARTICLES ON OLIGOCLASE

Crater Designation	PARTICLE DATA			CRATER DIMENSIONS				NORMALIZED DIMENSIONS			
	Velocity km/s	Mass $\times$ 10 <sup>-14</sup> kgm	Radius (microns)	Central Pit Length	Spall Dia Width	Dia(microns) Length	Pit Dia/ Particle Dia (D <sub>p</sub> /d)	Spall Dia/ Particle Dia (D <sub>s</sub> /d)	Length	Width	Length
S5-1-1				2.7	1.5	4.7	3.7	1.5	.85	2.7	2.1
S5-1-2				2.4	1.4	3.3	3.7	1.4	.80	1.9	2.1
S5-1-3	3.06±.11	2.24±.24	.88±.03	2.4	1.5	4.7	5.5	1.4	.85	2.7	3.1
S5-1-4				2.9	1.1	2.2	2.9	1.6	.63	1.3	1.6
S5-1-5				2.9	1.3	?		1.6	.74		
S5-1-6				2.7	1.2	2.2	3.7	1.5	.68	1.3	2.1
Average Values				2.7	1.3	3.4	3.9	1.5	.76	2.0	2.2

TABLE 10  
DATA FOR 60° OBLIQUE IMPACTS OF IRON PARTICLES ON OLIGOCLASE

Crater Designation	Velocity km/s	Mass $\times$ $10^{-14}$ kgm	Radius (microns)	CRATER DIMENSIONS				NORMALIZED DIMENSIONS			
				Length	Width	Central Pit Dia (microns)	Spall Dia (microns)	Pit Dia/ Particle Dia (D <sub>p</sub> /d)	Spall Dia/ Particle Dia (D <sub>s</sub> /d)	Length	Width
S-4-16-B	1.91	40.6	2.31	5.5	2.7	14	9.1	1.2	.58	3.0	2.0
S4-16-C	2.35	7.20	1.30	2.8	1.5	2.5	3.0	1.1	.58	.96	1.2
S4-16-A	2.64	14.2	1.63	4.2	2.3	9.9	6.4	1.3	.71	3.0	2.0
S4-11-A	2.71	17.2	1.73	6.6	3.7	10.0	9.4	1.9	1.1	2.9	2.7
S4-9-A	3.16	30.3	2.10	7.6	3.8	18.	11	1.8	.90	4.3	2.6
S4-4-A	4.23	13.7	1.61	7.4	3.4	21.	13	2.3	1.1	6.5	4.0
S4-4-B	4.50	6.51	1.25	5.6	2.5	19.	10.0	2.2	1.06	7.6	4.0
S3-12-A	5.20	4.58	1.12	5.6	2.6	9.2	8.3	2.5	1.2	4.1	3.7
S3-7-C	6.57	2.38	.897	8.1	2.6	11	11	4.5	1.4	6.1	6.1
S3-7-A	6.78	3.72	1.04	7.8	3.2	15	16	3.8	1.5	7.2	7.7
S3-7-B	6.85	3.20	.990	6.0	2.8	12	12	3.0	1.4	6.1	6.1
S3-14-A	9.08	.269	.434	2.5	1.5	3.8	3.8	2.9	1.7	4.4	4.4
S3-9-B	9.12	.232	.413	2.8	1.4	3.5	3.0	3.4	1.7	4.2	3.6
S3-14-B	9.37	.177	.378	2.8	1.3	4.3	3.2	3.7	1.6	5.7	4.2
S3-9-A	9.42	.261	.430	2.8	1.6	5.2	3.3	3.3	1.9	6.0	3.8
S4-2-A	20.6	.0146	.164	1.9	.79	2.9	2.3	5.8	2.4	8.8	7.0
S4-2-B	23.7	.0165	.171	1.3	1.1	2.8	2.8	3.8	3.2	8.2	8.2
S4-2-C	26.1	.00555	.119	1.4	.58	2.1	2.0	5.9	2.4	8.8	8.4

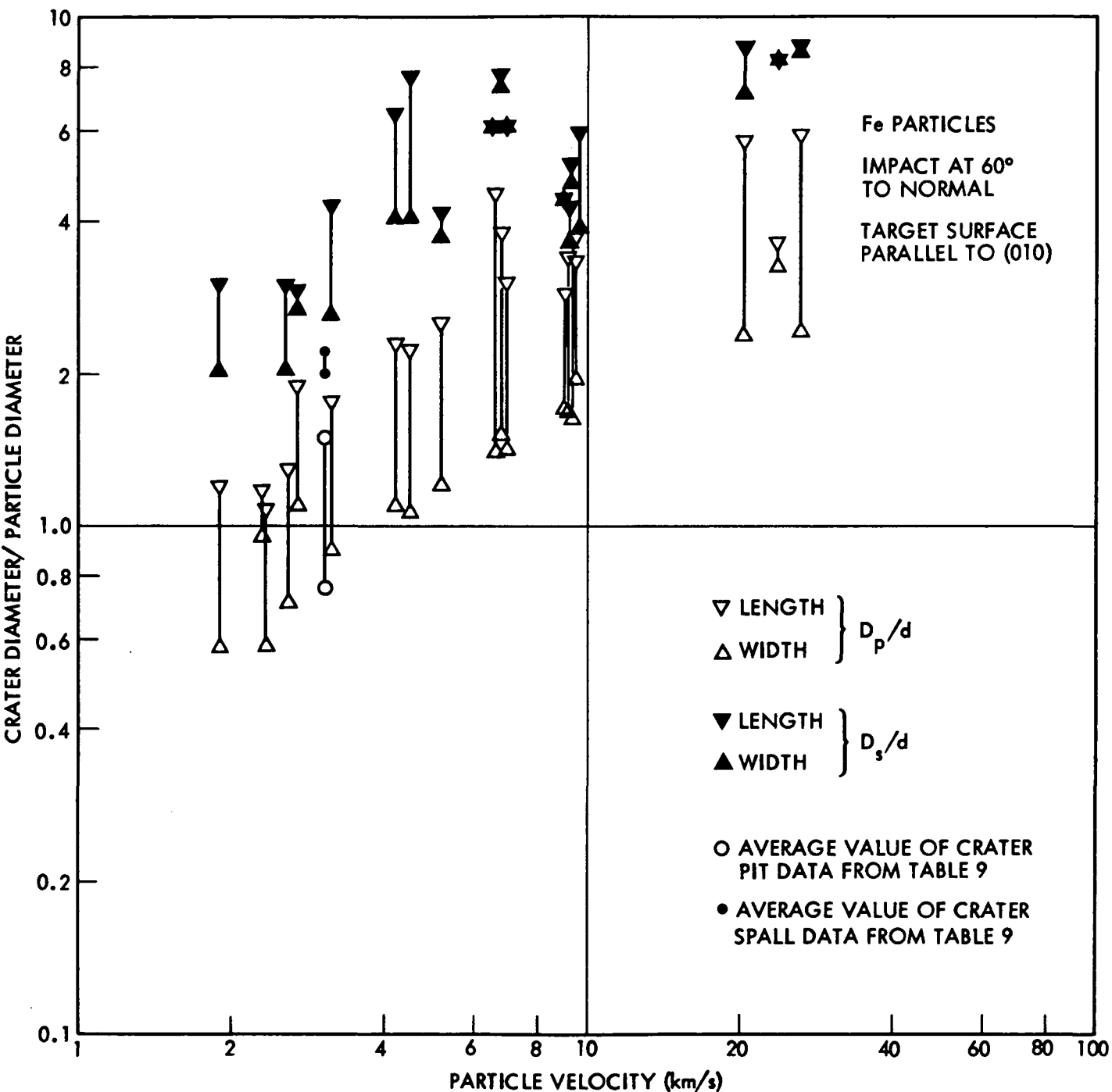


FIGURE 4-3. Crater Diameter/Particle Diameter vs Particle Velocity for 60° to Normal Impacts of Iron Particles on Oligoclase. Normalized central pit diameter ( $D_p/d$ ) is plotted in the lower part of figure while normalized spall diameter ( $D_s/d$ ) is plotted in the upper part of figure.

TABLE 11  
DATA FOR NORMAL IMPACT OF LANTHANUM HEXABORIDE PARTICLES ON OLIGOCLASE

Crater Designation	PARTICLE DATA			CRATER DIMENSIONS			NORMALIZED DIMENSIONS		
	Velocity km/s	Mass $\times$ $10^{-14}$ kgm	Radius (microns)	Central Pit Dia (microns) Max.	Spall Dia (microns) Max.	Pit Dia/ Particle Dia ( $D_p/d$ ) Max.	Spall Dia/ Particle Dia ( $D_s/d$ ) Max.	Spall Dia/ Particle Dia ( $D_s/d$ ) Min.	Spall Dia/ Particle Dia ( $D_s/d$ ) Min.
S2-2-A	1.46	41.2	3.35	10.0	4.8	32	9.7	1.5	.72
S2-2-B	1.73	18.5	2.57	14	7.7	8.7	3.9	2.7	1.5
S2-2-D	1.79	20.0	2.63	15	4.4	No Spall	2.9	.84	No Spall
S2-1-A	2.44	6.27	1.79	2.9	1.7	11	7.1	.81	.47
S2-2-C	2.67	5.71	1.74	11	7.0	No Spall	3.2	2.0	No Spall
S2-1-B	2.99	4.13	1.56	5.4	3.9	17	16	1.7	1.3
S2-3-A	4.49	2.09	1.24	5.8	1.6	6.2	5.4	2.3	.65
S2-3-B	4.91	1.50	1.11	3.9	1.8	No Spall	1.8	.81	No Spall
S2-3-C	5.12	1.06	.990	2.7	2.5	8.0	7.3	1.4	1.3
S2-4-B	6.21	.692	.859	2.5	2.3	4.2	4.0	1.5	1.3
S2-4-A	6.82	.721	.871	3.3	3.3	5.8	4.4	1.9	1.09
S2-4-C	7.78	.308	.656	2.9	1.3	No Spall	2.2	.99	No Spall
S2-6-D	9.73	.166	.534	1.9	1.2	Radial Cracks	1.8	1.1	Radial Cracks
S2-6-E	9.96	.104	.457	2.1	.91	No Spall	2.3	1.00	No Spall
S2-6-C	10.7	.0769	.413	2.8	.91	"	3.4	1.1	"
S2-7-D	13.2	.0209	.267	.91	.77	"	1.7	1.4	"
S2-7-B	13.3	.0454	.346	1.7	1.1	"	2.5	1.6	"
S2-7-C	14.5	.0169	.249	.69	.62	"	1.4	1.2	"
S2-8-D	16.1	.0161	.245	1.00	.73	2.5	1.4	2.0	1.5
S2-9-D	22.9	.00638	.180	1.5	.73	No Spall?	4.2	2.0	5.1
									2.9
								No Spall?	

TABLE 12  
DATA FOR OBLIQUE IMPACTS OF LANTHANUM HEXABORIDE PARTICLES ON OLIGOCLASE

Crater Designation	PARTICLE DATA			CRATER DIMENSIONS			NORMALIZED DIMENSIONS				
	Velocity km/s	Mass x 10-14 kgm	Radius (microns)	Central Pit Dia (microns) Length	Spall Dia/ Width	Pit Dia/ Width	Particle Dia (D/d)	Spall Dia/ Width	Particle Dia (D/d)	Length	Width
<u>30°</u>											
S2-1-C	2.43	5.53	1.72	5.8	2.1	No Spall	1.7	.61	No Spall		
S2-6-A	2.69	2.95	1.39	5.1	1.9	9.8	9.7	1.8	.68	3.5	3.5
S2-8-A	4.25	.905	.939	2.5	1.7	5.1	5.4	1.3	.91	2.7	2.9
S2-8-E	5.31	.451	.744	2.4	1.7	?	1.6	1.1	?		
<u>60°</u>											
S2-2-E	3.08	3.76	1.51	5.1	1.5	No Spall	1.7	.50	No Spall		
S2-7-A	3.36	1.39	1.08	3.8	1.9	"	1.8	.88	"		
S2-9-A	5.30	.302	.651	5.1	1.8	3.6	3.6	3.9	1.4	2.8	2.8
S2-9-B	5.86	.715	.868	1.8	1.2	No Spall	1.04	.69	No Spall		
S2-4-D	5.86	.292	.644	4.4	1.2	1.1	4.2	3.4	.93	.85	3.3
S2-5-A	8.18	.158	.525	3.1	1.8	No Spall	3.0	1.7	No Spall		

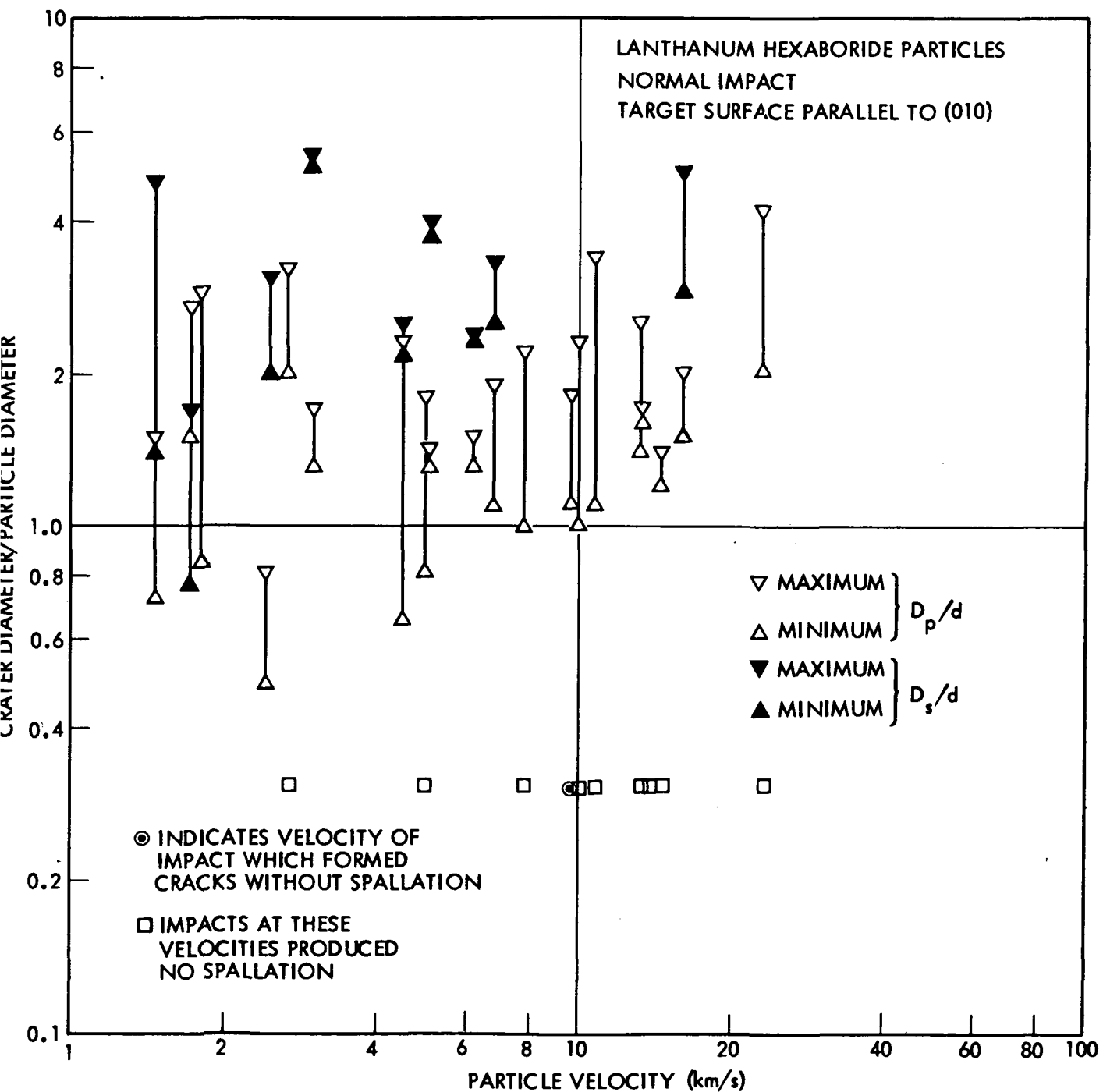


FIGURE 4-4. Crater Diameter/Particle Diameter vs Particle Velocity for Normal Impact of Lanthanum Hexaboride Particles on Oligoclase. Normalized central pit diameter ( $D_p/d$ ) is plotted in the lower part of figure while normalized spall diameter ( $D_s/d$ ) is plotted in the upper part of figure.

The data in Table 12 for both 30° and 60° oblique impacts are presented graphically in Figure 4-5. Again  $D_p/d$  and  $D_s/d$  have been plotted vs particle impact velocity. Note, as for the normal impacts of  $\text{LaB}_6$ , that a considerable number of the impacts failed to produce observable spallation.

#### 4.1.3 Silicon Particle Impacts on Oligoclase

##### 4.1.3.1 Normal Impacts at Different Crystal Orientations

The data contained in Table 13 are for normal impacts of silicon particles on oligoclase with the target surface parallel to the (010) plane as for all previous oligoclase targets. These data extend from 2.40 to 22.4 km/s and are arranged in ascending order of impact velocity as before. The data of Table 13 are shown graphically in Figure 4-6 in the same manner as done previously. The values for  $D_p/d$  and  $D_s/d$  are seen to differ only slightly from those obtained for normal impacts of lanthanum hexaboride which is not surprising since the density of the two materials also differs only slightly.

Table 14 also contains data for normal impact of silicon particles; however, here the target surface has been cut at 45° to both the (010) and (001) planes. Figure 4-7 is a graphical presentation of these data. Note that, although the normalized central pit diameter ( $D_p/d$ ) is essentially the same as in Figure 4-6, the normalized spall diameter  $D_s/d$  is noticeably larger for this target.

Table 15 contains data for normal impact of silicon particles on a surface parallel to the (001) plane. Figure 4-8 is a plot of  $D_p/d$  and  $D_s/d$  for these data. The values of  $D_s/d$  are slightly less than those obtained for either of the other two crystal orientations (Figures 4-6, and 4-7).

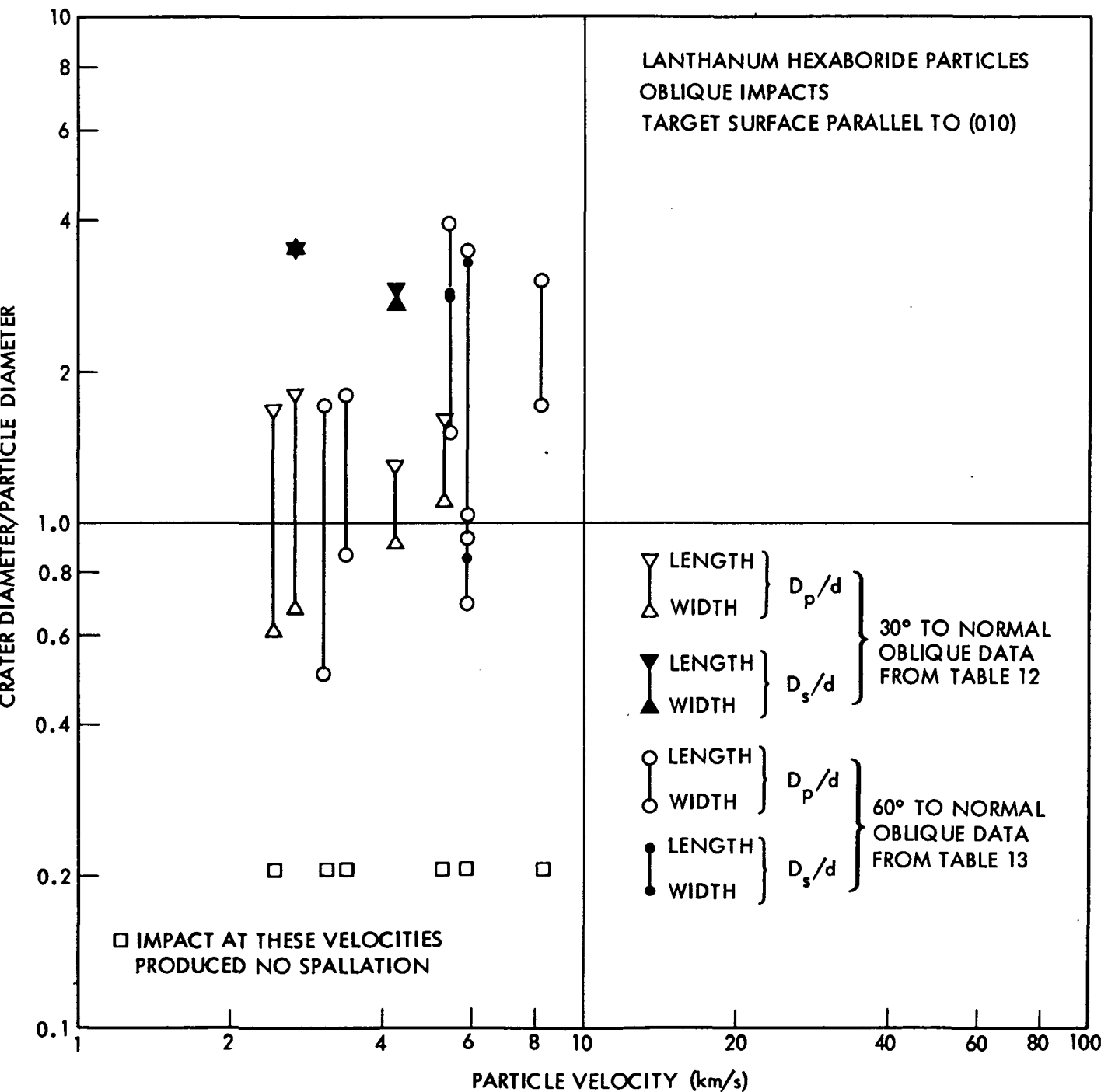


FIGURE 4-5. Crater Diameter/Particle Diameter vs Particle Velocity for Oblique Impacts of Lanthanum Hexaboride Particles on Oligoclase. Normalized central pit diameter ( $D_p/d$ ) is plotted in the lower part of figure while normalized spall diameter is plotted in the upper part of figure.

TABLE 13  
DATA FOR NORMAL IMPACTS OF SILICON PARTICLES ON OLIGOCLASE

Crater Designation	PARTICLE DATA			CRATER DIMENSIONS			NORMALIZED DIMENSIONS		
	Velocity km/s	Mass $\times$ $10^{-14}$ kgm	Radius microns	Central Pit Dia(microns)	Spall Dia (microns)	Pit Dia/ Particle Dia (D <sub>p</sub> /d)	Spall Dia/ Particle Dia (D <sub>s</sub> /d)	Spall Max.	Spall Min.
S6-3-A	2.40	22.3	2.84	No Pit	22	15	No Pit	3.9	2.6
S6-2-A	4.24	9.56	2.14	4.4	2.9	10.2	8.7	1.03	.68
S6-1-E	4.90	2.48	1.36	Undetermined	15	13	Undetermined	5.5	4.8
S6-1-C	5.16	1.55	1.17	3.3	2.2	Spall?	1.4	.94	Spall?
S6-1-B	5.93	3.90	1.59	3.6	3.2	9.7	7.9	1.1	1.0
S6-1-D	7.75	1.01	1.01	4.7	3.6	7.6	6.5	2.3	1.8
S6-1-A	8.25	1.45	1.14	3.3	2.6	12	10.2	1.4	1.1
S6-4-D	8.52	.801	.936	2.7	2.5	8.4	8.0	1.4	1.3
S6-4-A	9.68	.388	.736	2.5	2.1	5.8	5.1	1.7	1.4
S6-4-B	12.1	.469	.783	2.5	2.4	9.1	8.7	1.6	1.5
S6-4-C	13.1	.213	.602	3.3	2.0	5.4	4.0	2.7	1.7
S6-5-A	14.1	.162	.549	2.1	1.8	7.6	6.6	1.9	1.6
S6-5-B	16.8	.0373	.337	1.5	1.1	3.3	2.7	2.2	1.6
S6-5-C	20.6	.0281	.307	1.2	1.2	4.0	3.5	2.0	2.0
S6-10-A	22.4	.0209	.278	3.3	2.5	No Spall	6.3	4.0	No Spall

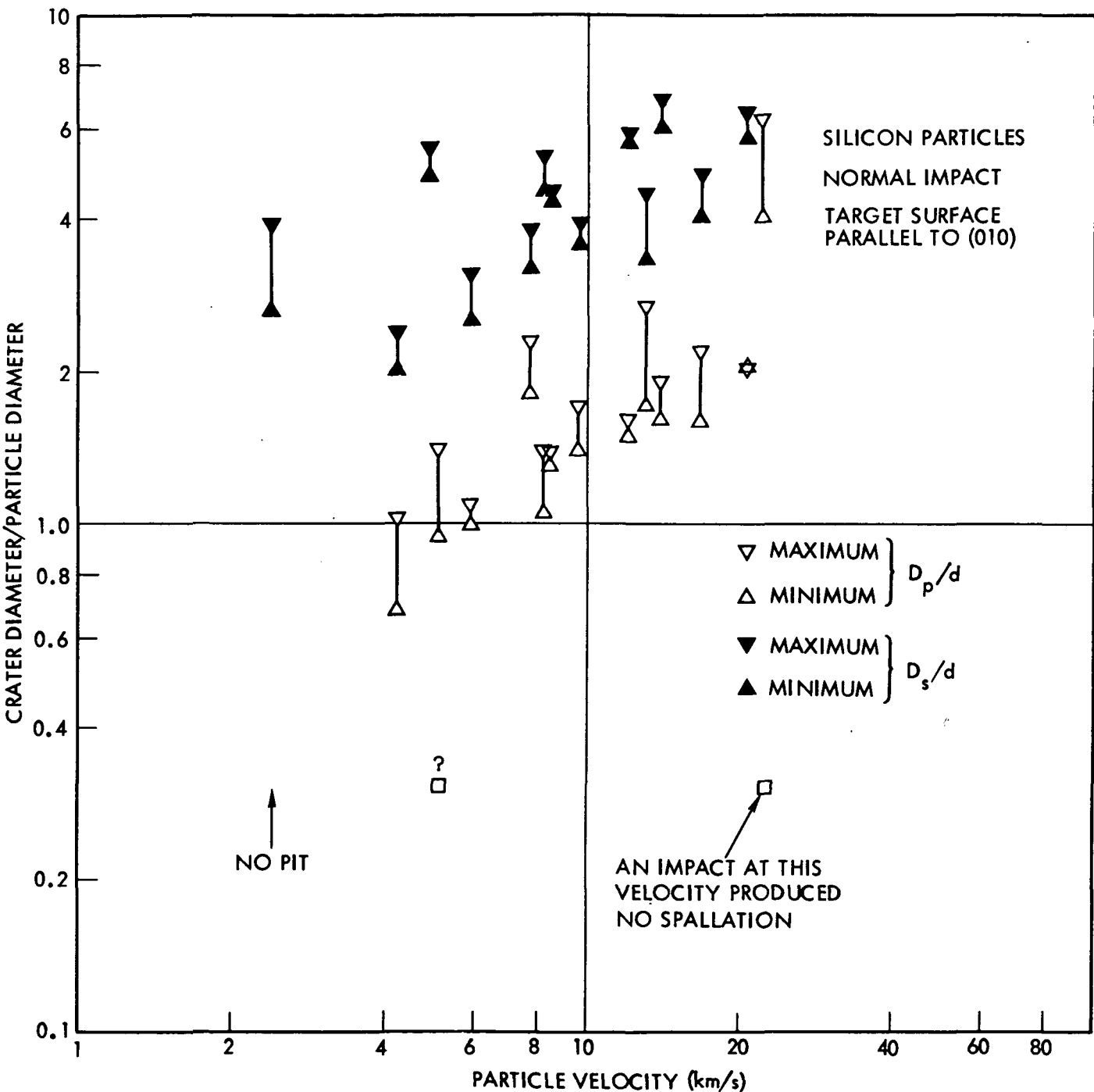


FIGURE 4-6. Crater Diameter/Particle Diameter vs Particle Velocity for Normal Impact of Silicon Particles on Oligoclase, Target Surface Parallel to (010). Normalized central pit diameter ( $D_p/d$ ) is plotted in the lower part of figure while normalized spall diameter ( $D_s/d$ ) is plotted in the upper part of figure.

TABLE 14  
DATA FOR NORMAL IMPACT OF SILICON PARTICLES ON OLIGOCLASE

Crater Designation	Velocity km/s	Mass X 10-14 kgm	Radius (microns)	PARTICLE DATA				CRATER DIMENSIONS				NORMALIZED DIMENSIONS			
				Max.	Min.	Max.	Min.	Central Dia(microns)	Pit Dia (microns)	Spall Dia (microns)	Pit Dia/ Particle Dia (D <sub>p</sub> /d)	Spall Dia/ Particle Dia (D <sub>s</sub> /d)	Max.	Min.	Max.
S9-4-C	2.12	8.35	2.04	No	Pit	11	4.4	No	Pit	2.7	No	Pit	2.7	1.08	
S9-4-A	2.63	5.25	1.75	4.5	2.1	8.4	6.5	1.3	.60	2.4	.60	2.4	1.9		
S9-4-D	2.81	10.9	2.23	Undetermined	27	11	7.6	1.06	1.00	3.5	1.06	6.1	2.5		
S9-4-E	3.09	3.64	1.55	3.3	3.1	11	7.6	1.06	1.00	3.5	1.06	6.1	2.5		
S9-3-B	3.32	5.84	1.82	5.1	3.4	25	11	1.4	.93	6.9	.93	6.9	3.0		
S9-3-C	4.23	2.11	1.29	4.0	2.6	6.2	5.9	1.6	1.00	2.4	1.00	2.4	2.3		
S9-3-A	5.03	3.90	1.59	4.4	3.6	25	17	1.4	1.1	7.9	1.1	7.9	5.3		
S9-3-D	5.25	1.38	1.12	3.1	2.5	20	18	1.4	1.1	8.9	1.1	8.9	8.0		
S9-2-A	5.31	1.61	1.18	3.3	2.0	11	7.4	1.4	.85	4.7	.85	4.7	3.1		
S9-2-B	6.10	1.03	1.02	2.9	1.7	15	12	1.4	.83	7.4	.83	7.4	5.9		
S9-2-C	6.90	1.22	1.08	2.0	2.0	14	9.4	.93	.93	6.5	.93	6.5	4.4		
S9-1-A	7.72	.944	.989	3.1	2.7	19	17	1.6	1.4	9.6	1.4	9.6	8.6		
S9-1-C	7.96	1.34	1.11	Undetermined	20	18	Undetermined	9.0	9.0	8.1	9.0	8.1			
S9-1-B	9.29	.896	.972	2.5	2.4	15	13	1.3	1.2	7.7	1.2	7.7	6.7		
S9-1-D	12.7	.193	.583	2.5	2.4	8.0	7.4	2.1	2.1	6.9	2.1	6.9	6.3		

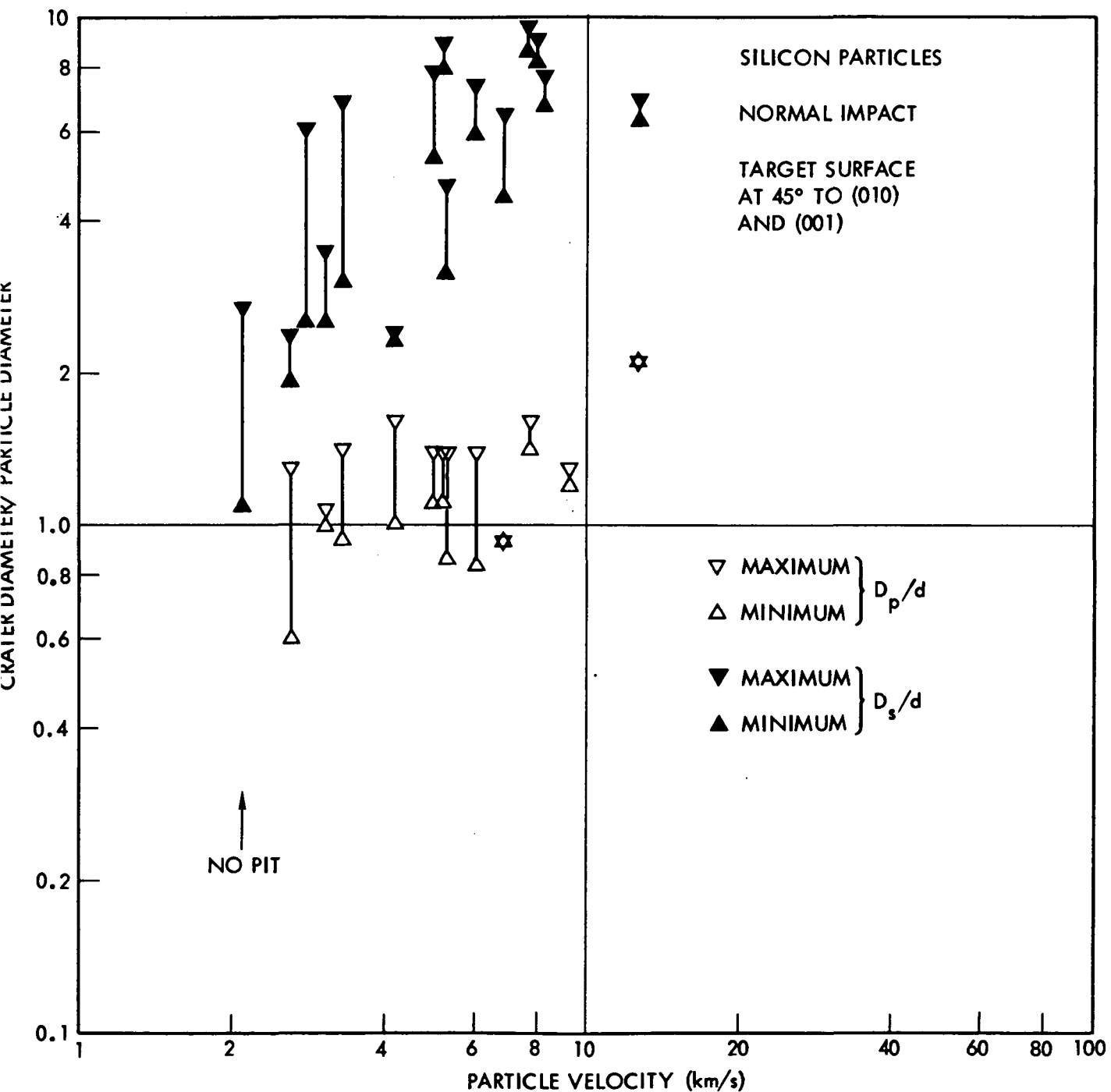


FIGURE 4-7. Crater Diameter/Particle Diameter vs Particle Velocity for Normal Impact of Silicon Particles on Oligoclase, Target Surface at  $45^\circ$  to (010) and (001). Normalized central pit diameter ( $D_p/d$ ) is plotted in the lower part of figure while normalized spall diameter is plotted in the upper part of figure.

TABLE 15  
DATA FOR NORMAL IMPACTS OF SILICON PARTICLES ON OLIGOCLASE

Crater Designation	PARTICLE DATA			CRATER DIMENSIONS			NORMALIZED DIMENSIONS		
	Velocity km/s	Mass $10^{-14}$ kgm	Radius (microns)	Central Dia(microns) Max. Min.	Spall Dia (microns) Max. Min.	Pit Dia/ Particle Dia ( $D_p/d$ )	Spall Dia/ Particle Dia ( $D_s/d$ )	Max. Min.	Max. Min.
S10-3-B	2.82	16.2	2.55	Undetermined	6.8	6.2	Undetermined	1.3	1.2
S10-3-A	3.57	3.78	1.57	4.1	4.0	12	8.7	1.3	3.8
S10-3-C	3.58	3.44	1.52	Undetermined	3.4	1.9	Undetermined	1.1	.63
S10-2-B	4.96	4.83	1.70	"	5.8	3.5	"	1.7	1.05
S10-2-A	5.03	4.57	1.67	"	5.4	5.3	"	1.6	1.6
S10-2-D	5.60	1.94	1.26	2.3	2.1	8.3	5.8	.91	.83
S10-1-D	7.47	.622	.860	2.7	1.6	6.1	4.4	1.6	.93
S10-1-E	10.6	.524	.813	3.1	2.6	11	7.8	1.9	1.6
S10-1-B	10.6	.281	.661	1.8	1.7	3.8	3.1	1.4	1.3
S10-1-C	10.7	.311	.683	2.4	2.0	3.7	3.6	1.8	1.5
S10-2-C	11.5	.242	.628	1.8	1.6	5.8	4.4	1.4	1.3
S10-1-A	12.4	.204	.593	1.7	1.6	3.8	3.6	1.4	1.3

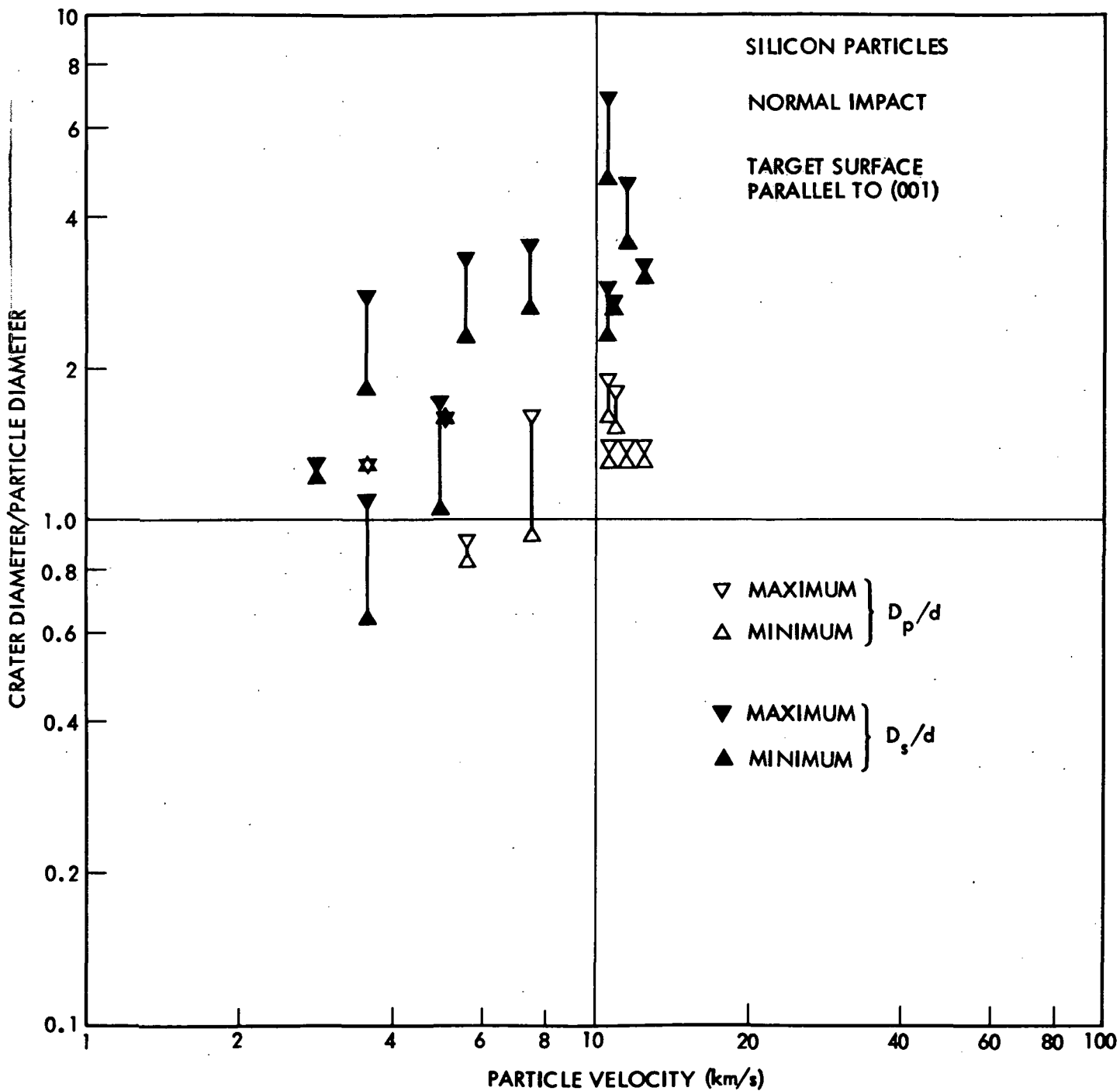


FIGURE 4-8. Crater Diameter/Particle Diameter vs Particle Velocity for Normal Impact of Silicon Particles on Oligoclase, Target Surface Parallel to (001). Normalized central pit diameter ( $D_p/d$ ) is plotted in the lower part of figure while normalized spall diameter ( $D_s/d$ ) is plotted in the upper part of figure.

#### 4.1.3.2 Oblique Impacts

The data for 30° to normal oblique impacts of silicon particles on oligoclase are shown in Table 16. These data extend from 2.31 to 20.6 km/s and are arranged in ascending order of impact velocity. The target surface is parallel to (010) as is true for Table 17 which follows and all other oligoclase targets except two presented in Section 4.1.3.1. The data of Table 16 are presented graphically in Figure 4-9 in the same manner as was done previously. The values of  $D_p/d$  and  $D_s/d$  are seen to be substantially the same as those found for normal impacts shown in Figure 4-6.

Table 17 contains 60° to normal oblique impact data. These data are graphically shown in Figure 4-10. There are a considerable number of the 60° to normal impacts which did not produce observable spallation. These have been so indicated by small squares placed at the appropriate velocity. Note that all impacts above 12 km/s produced no observable spallation and that the value of  $D_s/d$  is substantially less at the lower velocities than was obtained at normal and 30° to normal impact.

TABLE 16  
DATA FOR 30° OBLIQUE IMPACTS OF SILICON PARTICLES ON OLIGOCLASE

Crater Designation	PARTICLE DATA			CRATER DIMENSIONS			NORMALIZED DIMENSIONS		
	Velocity km/s	Mass x 10-14 kgm	Radius microns	Central Pit Length	Pit Dia/ Width	Spall Dia/ Width	Pit Dia/ Length	Particle Dia/ Width	Spall Dia/ Length
S5-13-D	2.31	14.1	2.44	1.5	2.7	Cracks	.31	.55	Cracks
S5-13-B	3.12	9.73	2.15	6.5	1.4	"	1.5	.33	"
S5-16-A	4.58	2.55	1.38	6.2	4.0	1.9	9.7	2.2	1.4
S5-11-B	4.78	2.47	1.36	4.7	3.0	9.1	6.0	1.7	1.1
S5-11-C	4.88	2.03	1.28	7.6	1.9	1.3	8.6	3.0	.74
S5-4-B	5.91	1.30	1.10	2.9	3.1	6.2	5.4	1.3	1.4
S5-4-A	6.53	1.33	1.11	4.0	2.7	1.3	7.0	1.8	1.2
S5-9-A	7.55	1.46	1.14	4.4	2.7	1.3	12	1.9	1.2
S5-4-C	8.18	1.28	1.09	4.0	2.7	1.3	7.0	1.8	1.2
S6-8-A	10.5	.389	.736	2.7	2.5	5.8	5.0	1.8	1.7
S6-13-C	10.6	.680	.887	3.3	3.7	9.8	8.1	1.9	2.1
S6-13-B	11.7	.299	.674	2.7	2.3	1.8	4.6	2.0	1.7
S6-8-B	14.3	.255	.613	2.7	1.6	1.1	6.6	2.2	1.3
S6-6-D	16.2	.0404	.346	1.5	1.3	2.4	2.7	2.2	1.9
S6-6-B	16.9	.0459	.361	1.6	1.8	No Spall	2.2	2.5	No Spall
S6-6-A	19.6	.0318	.319	1.3	1.1	2.7	3.3	2.0	1.7
S6-6-C	20.6	.0252	.296	1.3	1.2	2.9	2.2	2.2	2.0

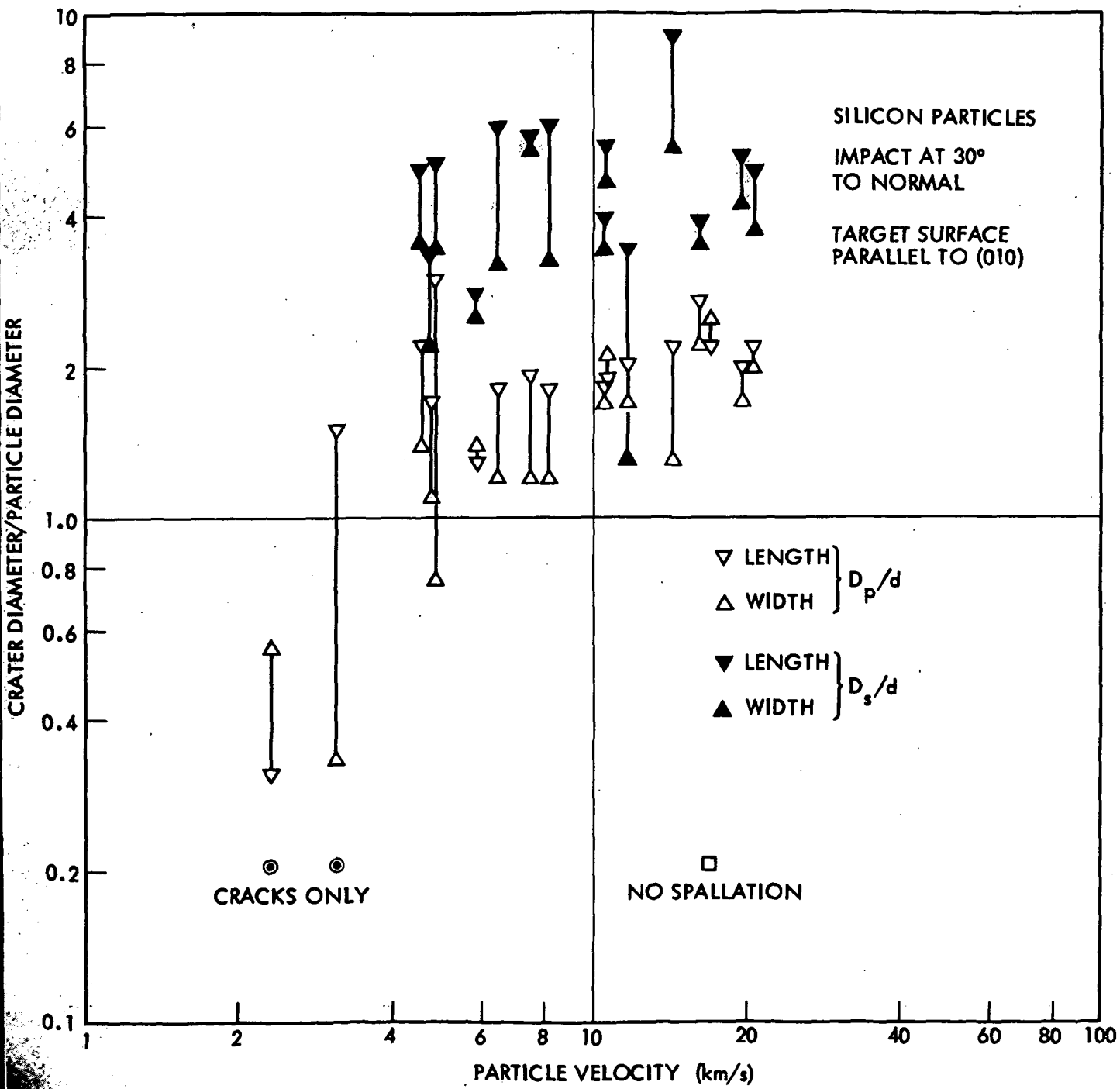


FIGURE 4-9. Crater Diameter/Particle Diameter vs Particle Velocity for 30° to Normal Oblique Impact of Silicon Particles on Oligoclase. Normalized central pit diameter ( $D_p/d$ ) is plotted in the lower part of figure while normalized spall diameter ( $D_s/d$ ) is plotted in the upper part of figure.

TABLE 17  
DATA FOR 60° OBLIQUE IMPACTS OF SILICON PARTICLES ON OLIGOCLASE

Crater Designation	PARTICLE DATA			CRATER DIMENSIONS			NORMALIZED DIMENSIONS		
	Velocity km/s	Mass x 10-14 kgm	Radius (microns)	Central Pit Length	Spall Dia (microns) Width	Spall Dia Length	Pit Dia/ Particle Dia (Dp/d)	Pit Dia/ Particle Dia (Ds/d)	Spall Dia/ Particle Dia (Ds/d)
S5-19-A	2.18	11.6	2.28	No Pit	No Spall	No Pit	.57	.39	"
S5-12-C	3.23	7.12	1.94	2.2	1.5	"	"	"	"
S5-12-A	3.66	10.1	2.18	No Pit	"	No Pit	.52	.66	2.2
S5-12-D	4.57	2.89	1.44	1.5	1.9	6.2	7.6	.95	2.6
S5-10-A	7.18	1.72	1.21	5.8	2.3	Cracks	2.4	"	Cracks
S5-15-D	8.18	.620	.860	3.6	1.5	No Spall	2.1	.87	No Spall
S5-5-A	8.56	1.42	1.13	3.6	2.3	5.8	5.0	1.6	1.02
S5-5-C	9.08	1.14	1.05	5.8	2.3	7.6	5.0	2.8	1.1
S6-14-B	10.6	.288	.666	5.3	1.5	No Spall	4.0	1.1	3.6
S6-9-B	12.1	.210	.599	4.0	1.2	4.4	3.1	3.3	2.4
S6-14-A	12.2	.231	.619	3.4	2.3	No Spall	2.7	1.9	No Spall
S6-9-A	14.2	.144	.527	4.0	1.7	"	3.8	1.6	"
S6-12-A	17.5	.0345	.328	1.6	1.2	"	2.4	1.8	"
S6-7-A	17.9	.0401	.345	2.5	.97	"	3.6	1.4	"
S6-12-B	19.3	.0253	.296	1.8	1.2	"	3.0	2.0	"
S6-12-C	19.5	.0298	.312	1.6	.97	"	2.6	1.6	"

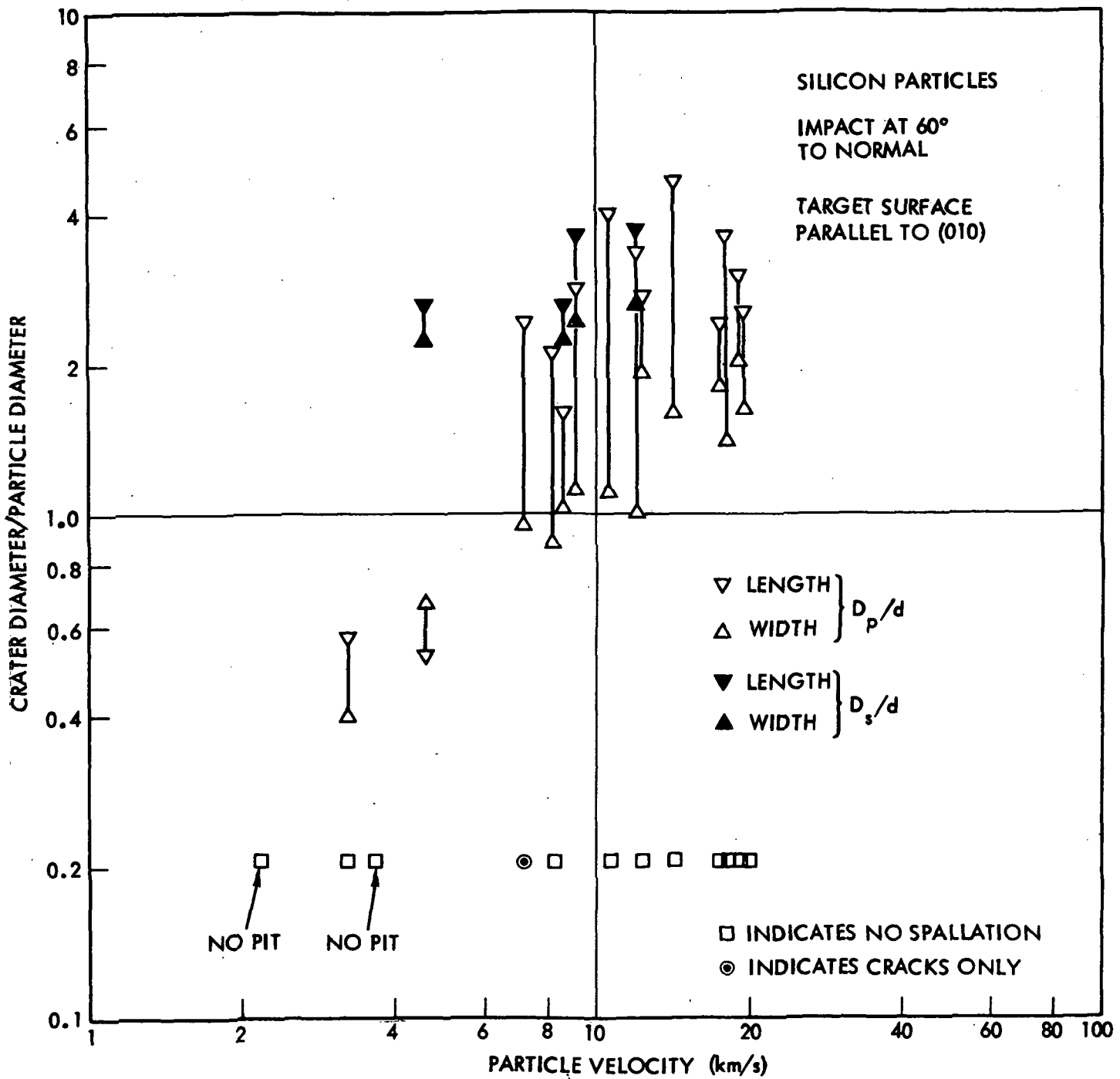


FIGURE 4-10. Crater Diameter/Particle Diameter vs Particle Velocity for 60° to Normal Oblique Impact of Silicon Particles on Oligoclase. Normalized central pit diameter ( $D_p/d$ ) is plotted in the lower part of figure while normalized spall diameter is plotted in the upper part of figure.

4.2 Photographs of Impact Craters in Minerals

Three different particle materials were used during the course of the program to impact oligoclase at three different impact angles. In addition, two different crystal orientations of oligoclase and six other minerals were used with one particle material. The result is eighteen sets of crater photographs with each set displaying somewhat different characteristics. These photographic data have been arranged according to particle material with the different impact angles, crystal orientations, and target materials subgrouped under these major headings.

The order of presentation will be by decreasing particle density which is iron, lanthanum hexaboride, and silicon. A brief description will be given with each set of photographs which will include impact parameters as well as typical crater characteristics where such can be noted.

In order for the reader to have complete information regarding the impact parameters, each crater photograph will be accompanied by its unique crater designation number so that numerical data concerning the crater or impact particle may be readily found in Tables 1 through 17 in Section 4.1. Recall that the tables are organized according to particle material, impact angle, target material, and finally in terms of increasing velocity.

All crater photographs in this report were taken by scanning electron microscope using secondary electron emission as the imaging source. In order to enhance the photographic quality of the crater photographs obtained, the target has been generally tilted by some angle less than 30°. The tilt angle is measured from the target surface normal vector and defines the angle at which the observer views the target surface. To achieve the tilt angle, the target is rotated about an axis running left-right through the center of the photograph. The target surface at the lower edge of the picture is raised from its normal

position sufficient to cause the target surface to move through an angle equal to the tilt angle. The tilt angle for each photograph will be included in the figure caption where the photo appears.

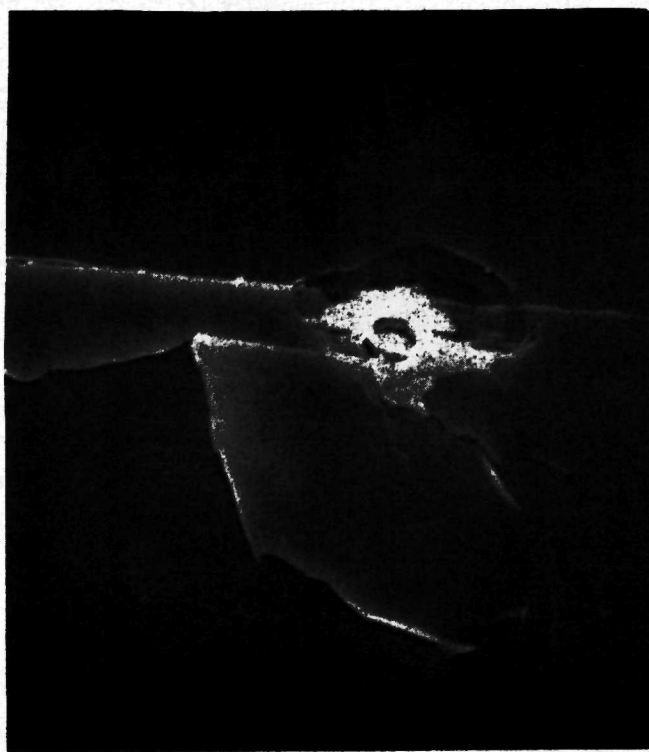
#### 4.2.1 Iron Particle Impact Craters

##### 4.2.1.1 Photographs of Normal Impact Craters in Oligoclase

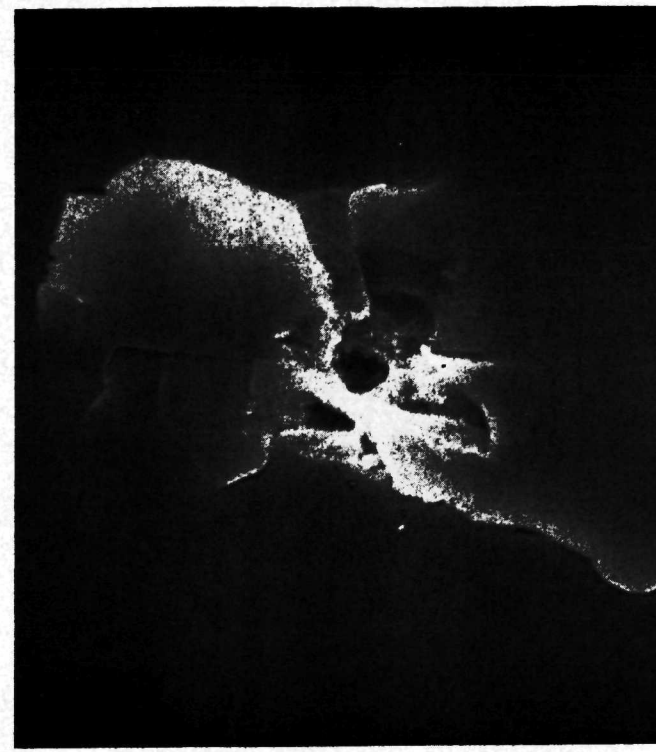
The impact velocity range for this set of photographs extends from 2.75 to 11.5 km/s. The photos are arranged in the order of increasing impact velocity. Each crater photograph has been given a set of index marks whose spacing indicates the approximate magnification. The spacing of the index marks for each crater photograph will be given in the figure caption where the photo appears and will not be given in the text of the report.

Figure 4-11a shows the impact crater obtained at 2.85 km/s. Here one sees extensive development of spall plates; however, only a small fraction of these have been ejected from the surface. There has been no attempt made to distinguish between spall plates developed and those ejected. Generally speaking, only a few of the spall plates formed are ejected. In the quantitative section (4.1) the spallation dimensions given refer to the total damage area where well developed spall plates exist. In Figure 4-11a the central pit lip structure is small and partially broken away. Below this the impact particle can apparently be seen still residing in the crater.

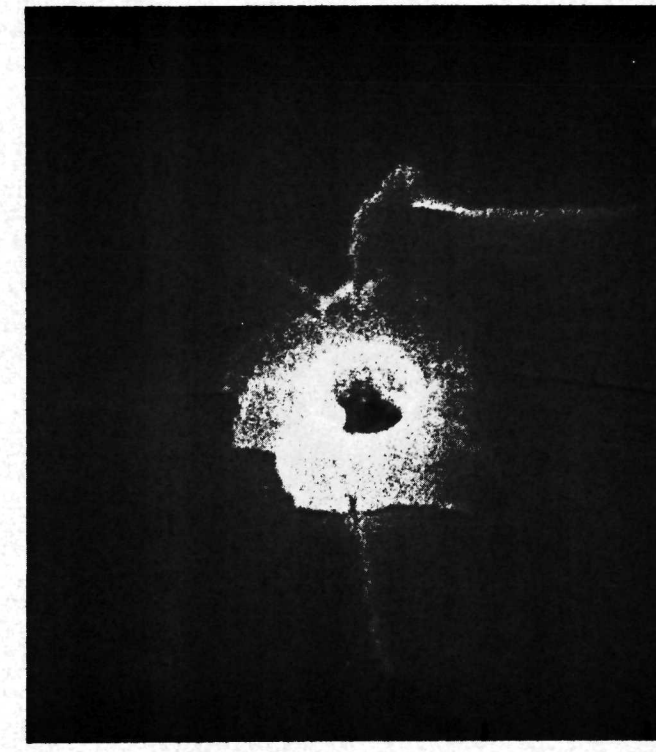
The velocity of impact increases from Figure 4-11a through h. The crater shown in (h) was formed at an impact velocity of 5.47 km/s. There is essentially no ejected spall at this velocity although there is still an extensive development of spall plates. Note that a well defined lip structure exists on all impacts except (b) at 3.08 km/s which has spalled away. Also note that the extensive production of droplets within the central crater which adhere to the walls of the crater. The size of the droplets generally increase with impact velocity and their absolute



(a)



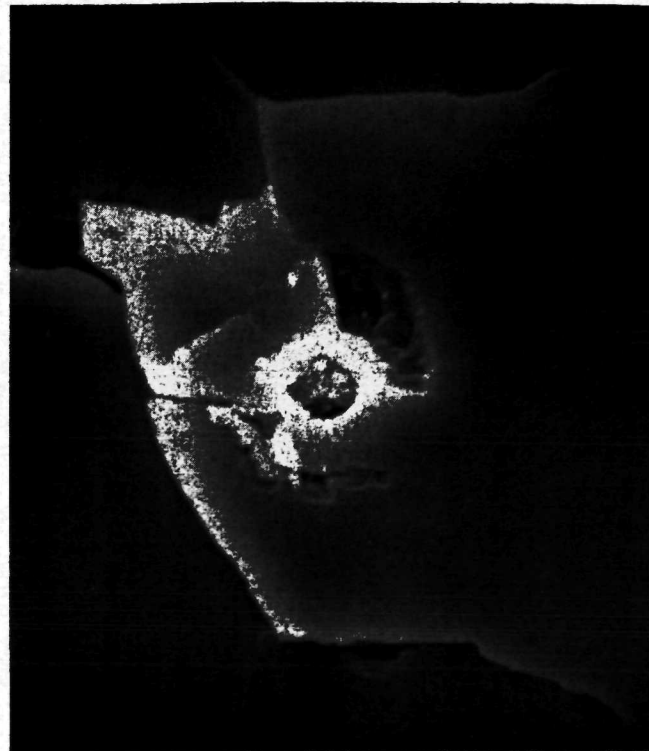
(b)



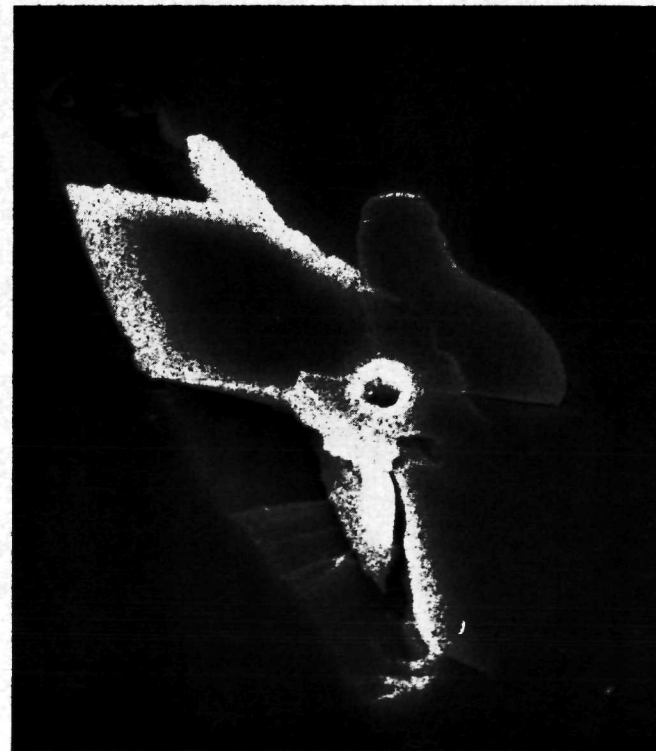
(c)



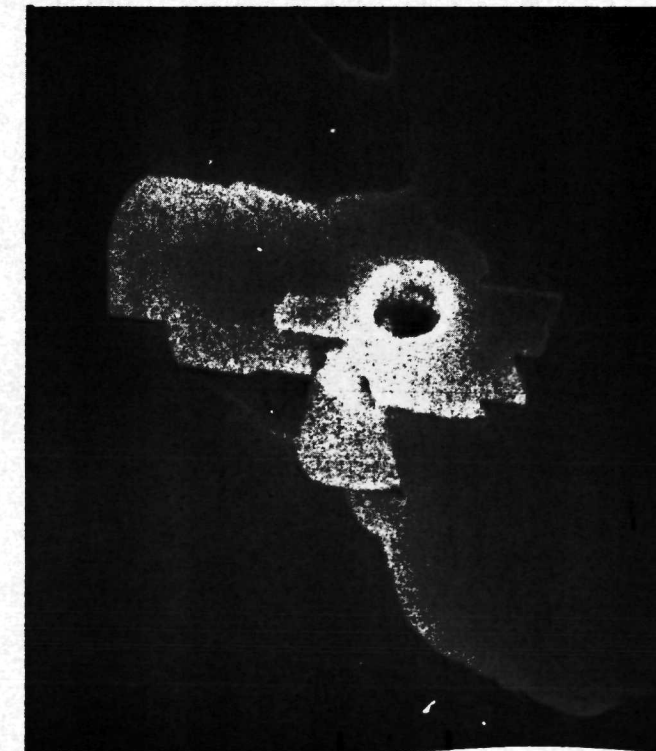
(d)



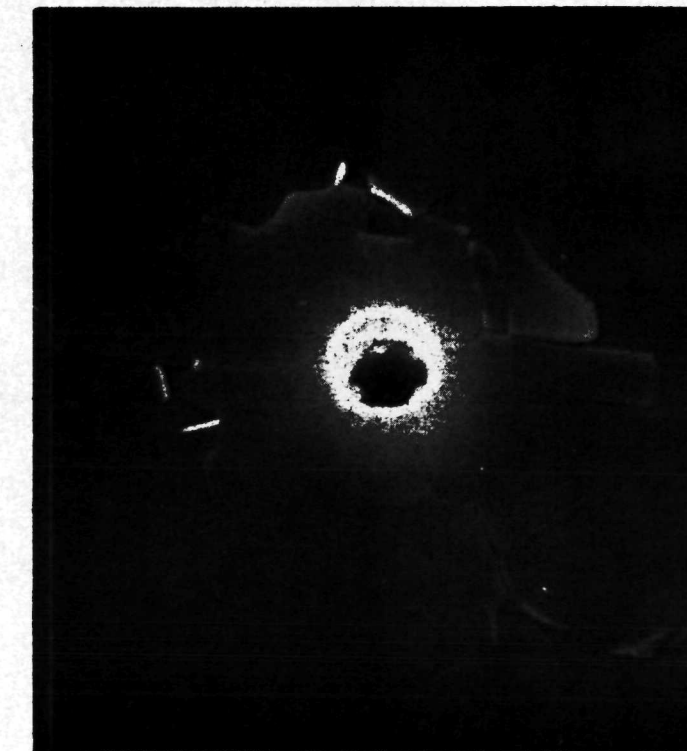
(e)



(f)



(g)



(h)

FIGURE 4-11. Photographs of Craters from Normal Impacts of Iron Particles on Oligoclase, 2.86 to 5.47 km/s:  
(a); crater S4-13-D, 2.86 km/s, 10 micron index marks. (b); crater S4-13-B, 3.08 km/s, 10 micron index marks. (c); crater S4-13-A, 3.33 km/s, 5 micron index marks. (d); crater S4-14-B, 4.09 km/s, 5 micron index marks. (e); crater S4-14-A, 4.39 km/s, 5 micron index marks. (f); crater S4-15-B, 4.44 km/s, 10 micron index marks. (g); crater S4-15-A, 4.82 km/s, 5 micron index marks. (h); crater S4-15-C, 5.47 km/s, 5 micron index marks. All have 20° tilt angles.

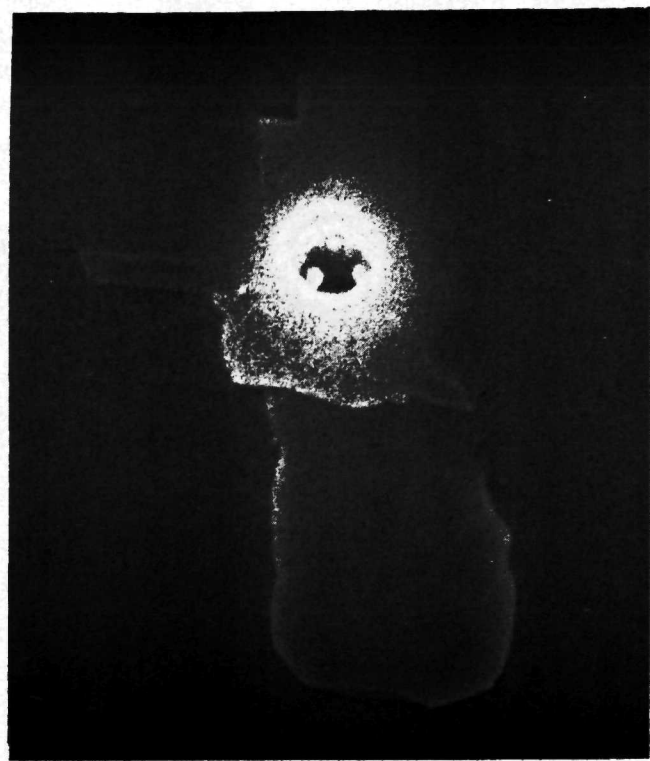
number diminishes. This will be more apparent when the higher velocity impacts of this set are viewed. In (f) is a photograph which is a good example of the tendency for the target to fracture along the cleavage planes of the crystal.

Figure 4-12 is a continuation of the photographic set of normal impact of iron particles on oligoclase. The velocity of impact ranges from 6.16 km/s in (a) to 11.4 km/s in (h). It can be easily seen that the extent of spallation is decreasing to where it has essentially vanished at the higher velocities. Note also that the droplets mentioned previously grow in size as the impact velocity is increased from (a) through (h). In (f), (g) and (h) there appears to be only one massive droplet near the bottom of the crater pit. The lip size relative to the pit diameter increases slightly. The surface pattern seen around the crater in (e) through (h) is the result of the thin aluminum film being ejected from the surface.

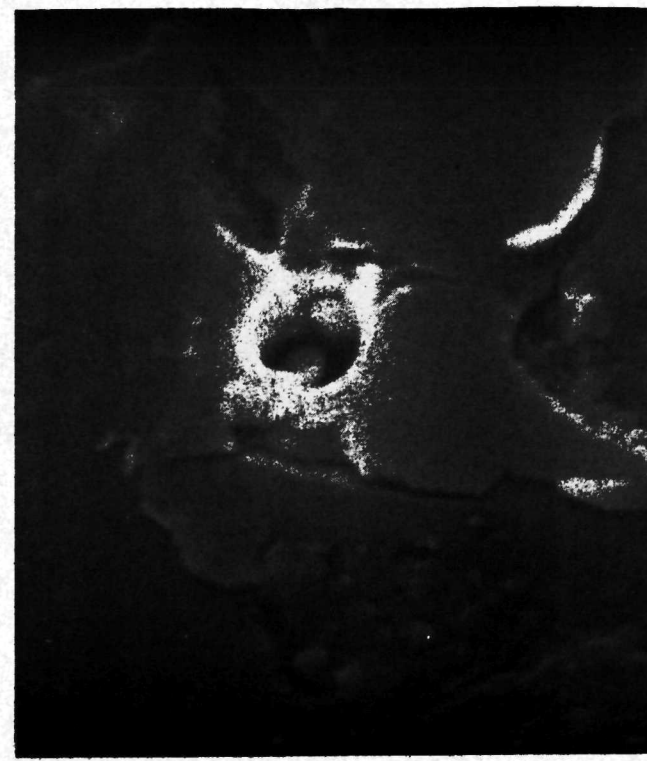
#### 4.2.1.2 Photographs of Craters from Normal Impact on Miscellaneous Minerals

Figure 4-13 contains photographs of six craters in oligoclase produced by particles with controlled parameters. The average impact velocity was  $3.06 \pm .11$  km/s. These data are described quantitatively in Table 2. These craters show very close agreement as to central pit diameter. The impacting particles are apparently still stuck in the craters shown in (c) and (d).

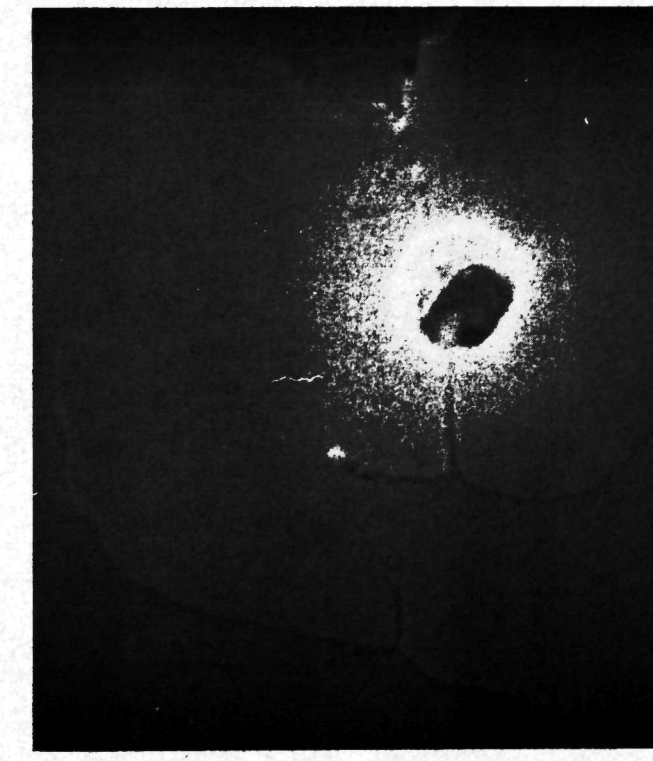
Figure 4-14 contains six impact crater photographs formed in diopside at 3.06 km/s. There is very little lip structure seen in these photos which is due to the lip being carried away by spallation. A well developed crystal structure is evidenced by the cleavage planes exposed by spallation.



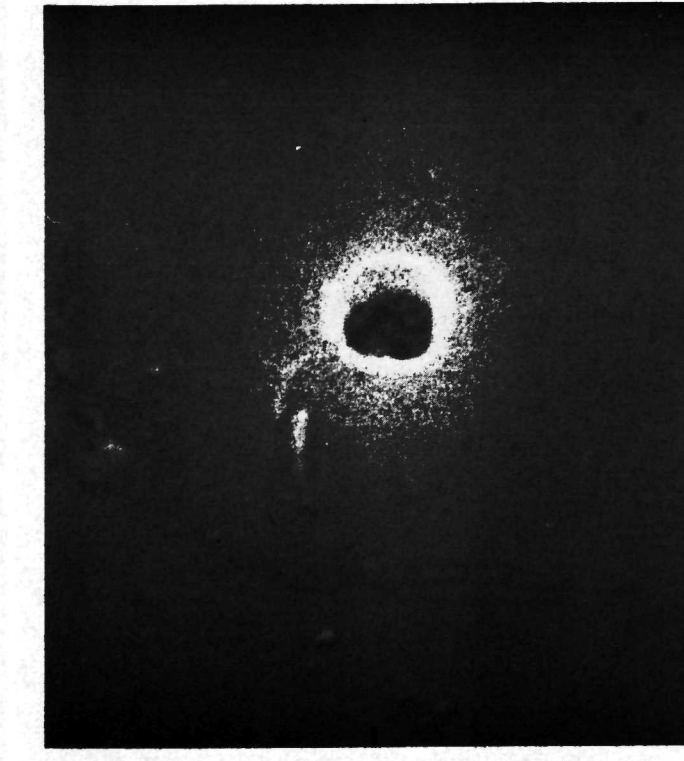
(a)



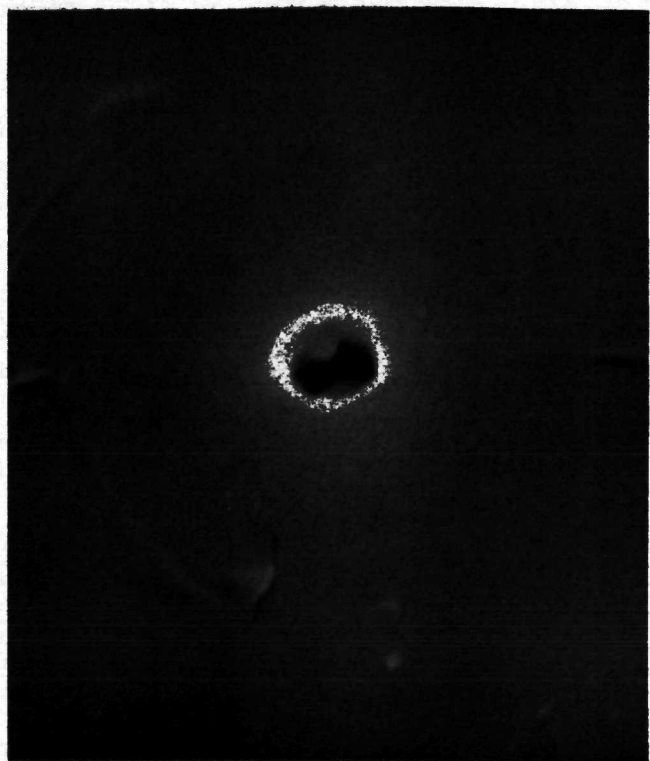
(b)



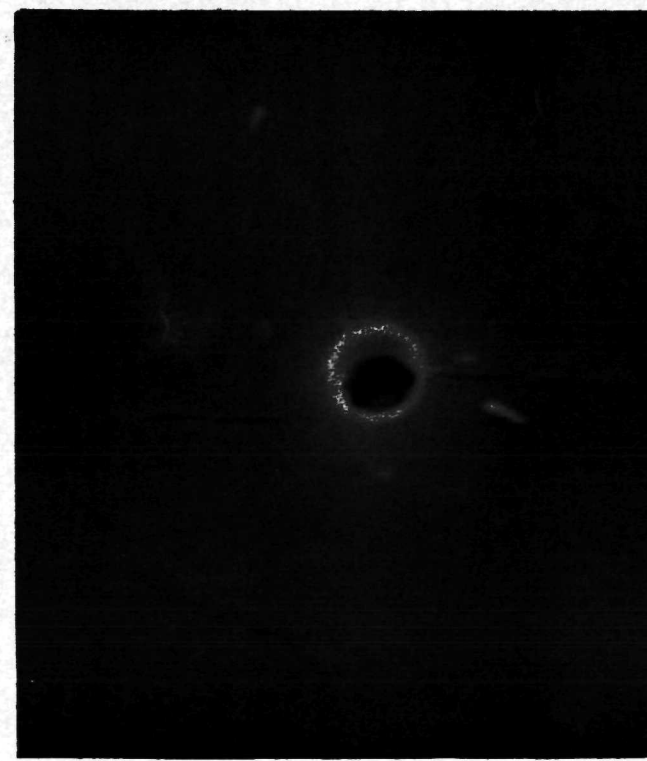
(c)



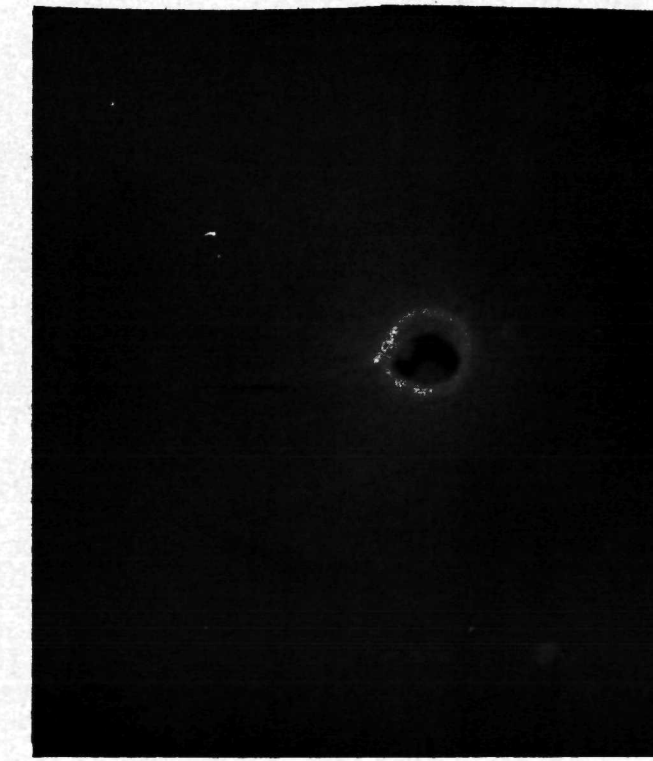
(d)



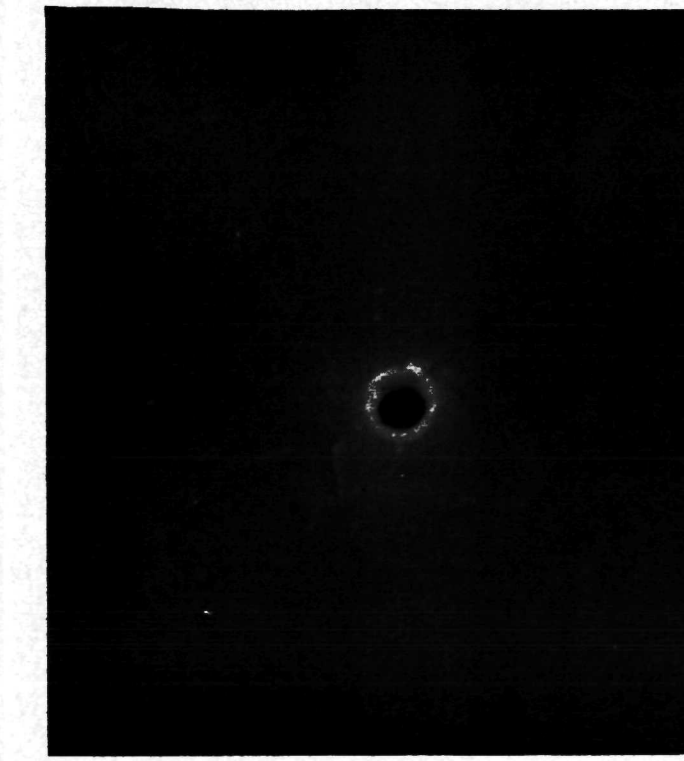
(e)



(f)



(g)

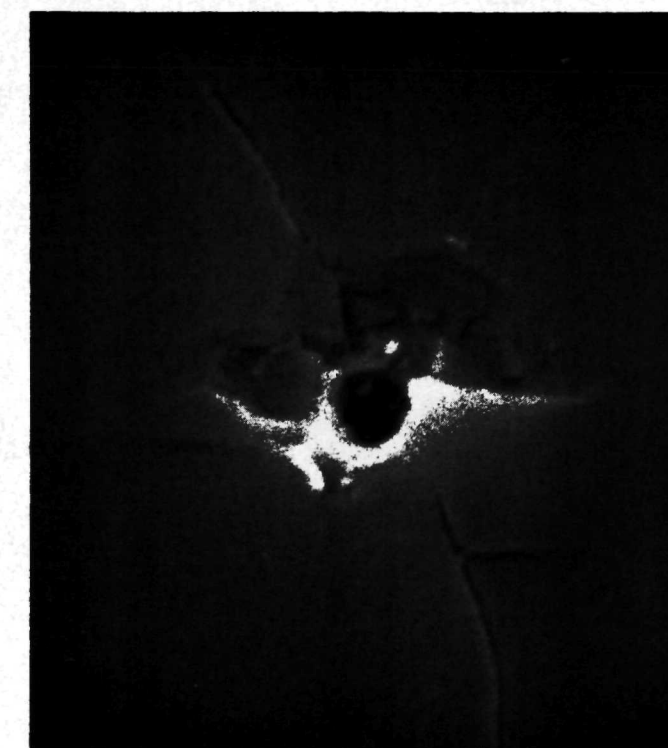


(h)

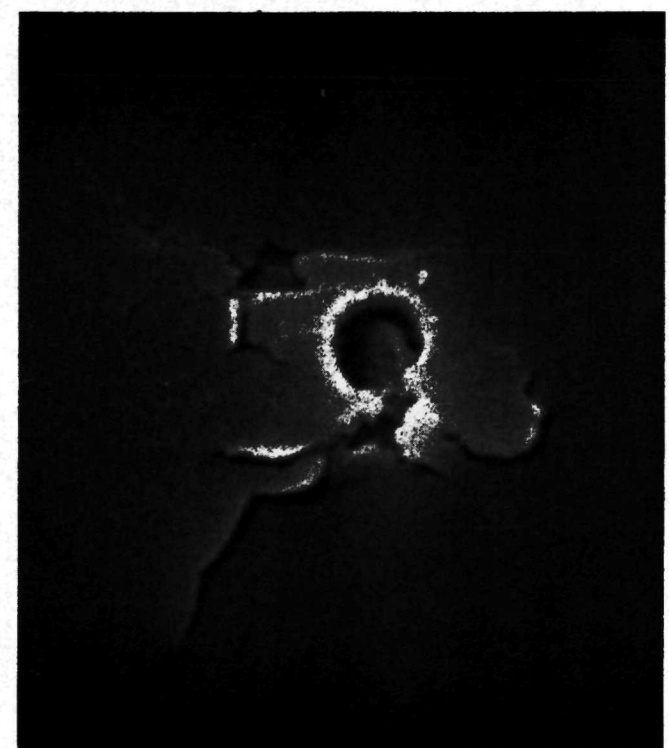
FIGURE 4-12. Photographs of Craters from Normal Impacts of Iron Particles on Oligoclase, 6.16 to 11.4 km/s:  
(a); crater S4-15-D, 6.16 km/s. (b); crater S3-1-C, 6.99 km/s. (c); crater S4-14-C, 7.11 km/s.  
(d); crater S3-17-B, 7.53 km/s. (e); crater S3-17-A, 7.87 km/s. (f); crater S3-18-B, 8.74 km/s.  
(g); crater S3-18-A, 9.37 km/s. (h); crater S3-19-A, 11.4 km/s. (a) has 5 micron indexes, all  
others have 2 micron indexes. All have 20° tilt angles.



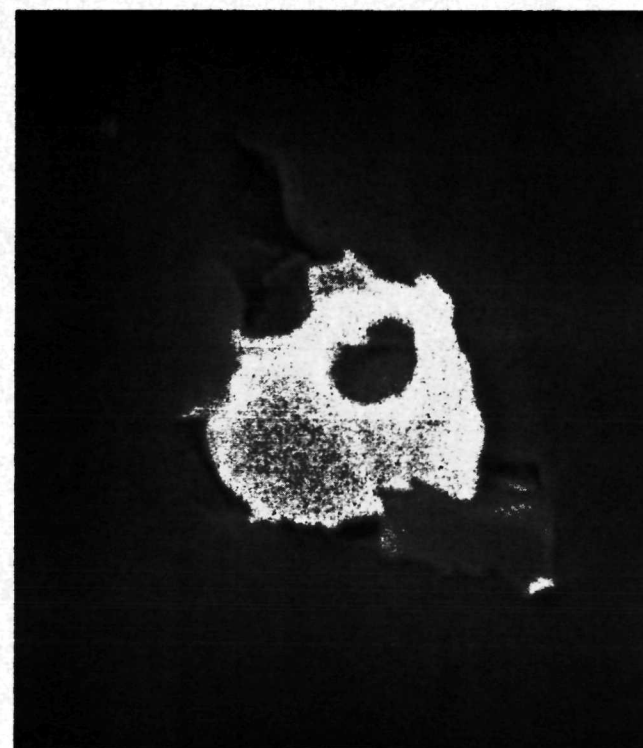
(a)



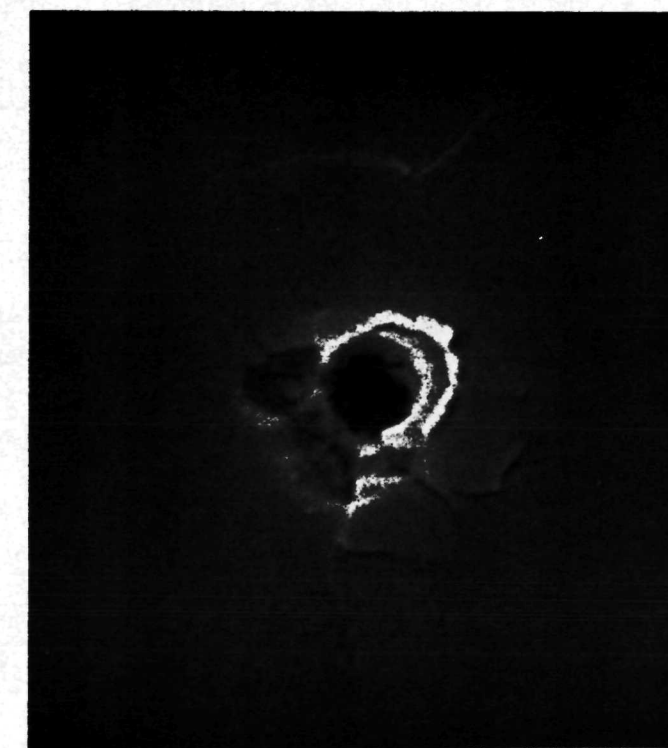
(b)



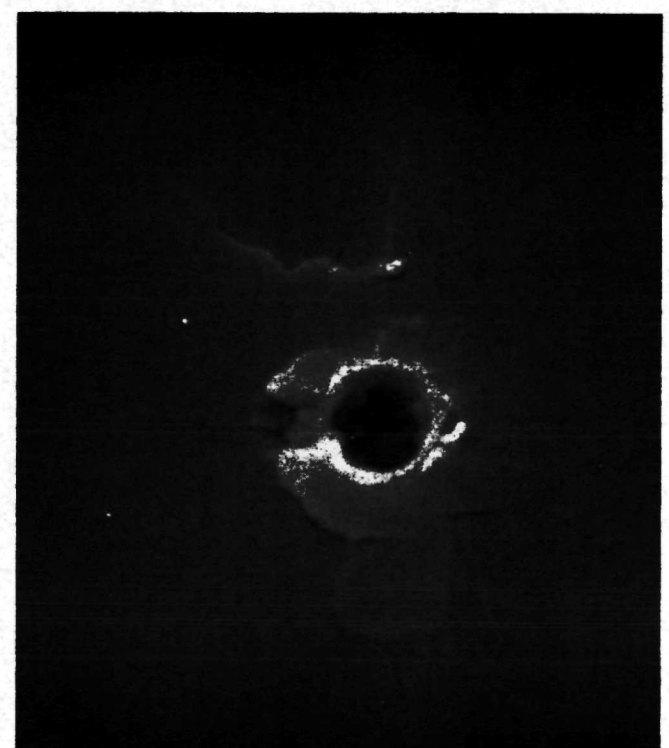
(c)



(d)

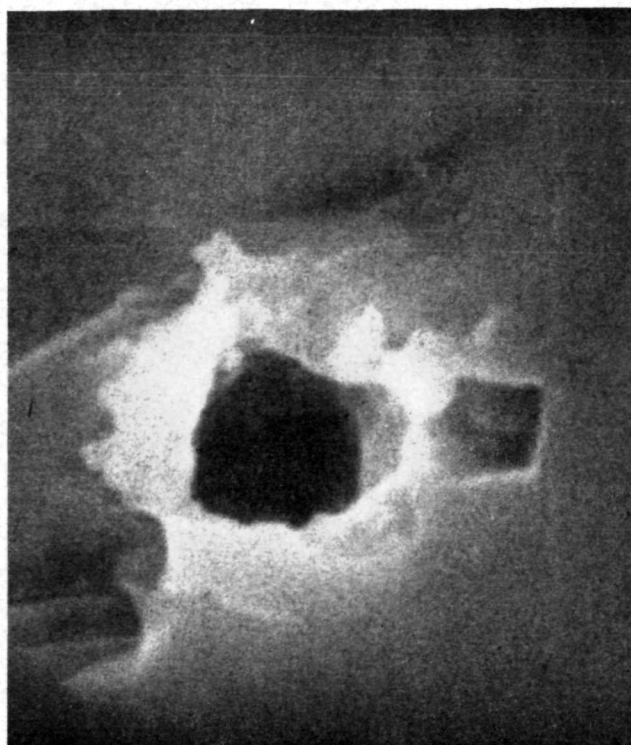


(e)

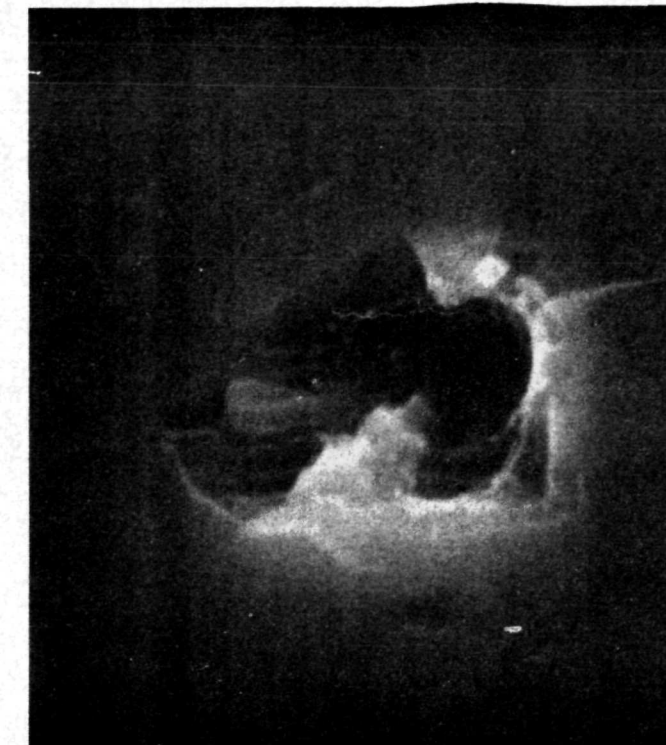


(f)

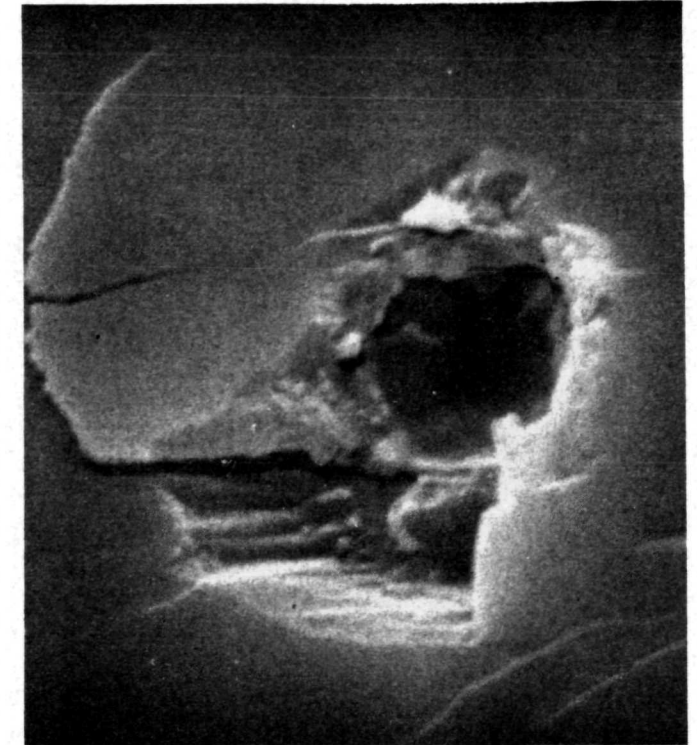
FIGURE 4-13. Photographs of Craters from Normal Impacts of Iron Particles on Oligoclase at 3.06 km/s: (a) through (f) correspond to craters S5-3-1 to S5-3-6, respectively, all with 2 micron index mark separation and 20° tilt angle.



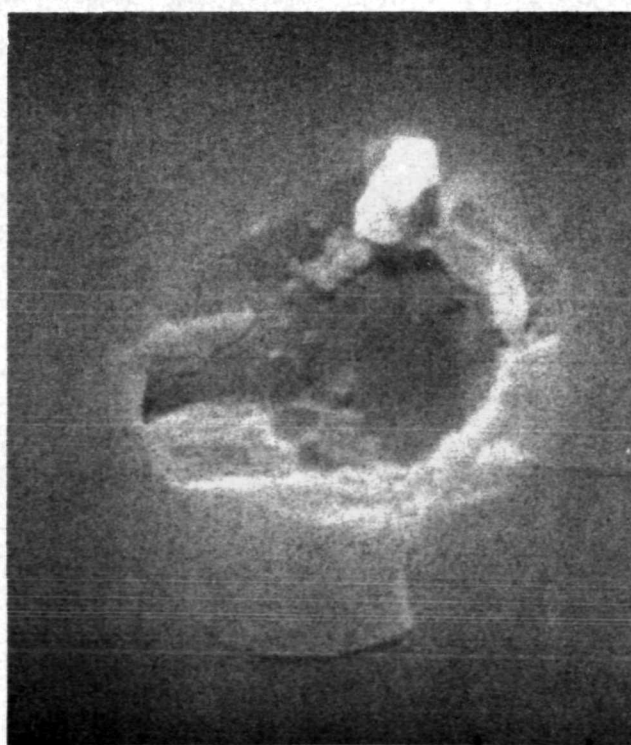
(a)



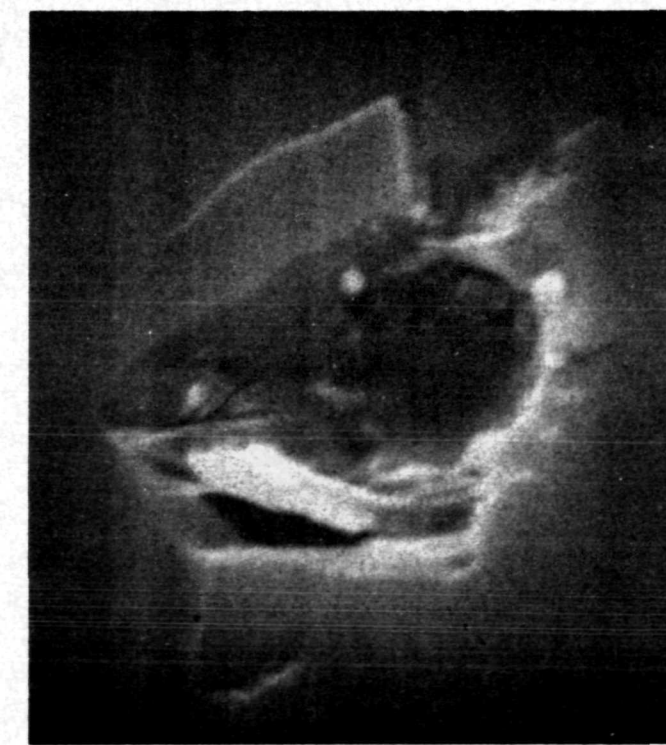
(b)



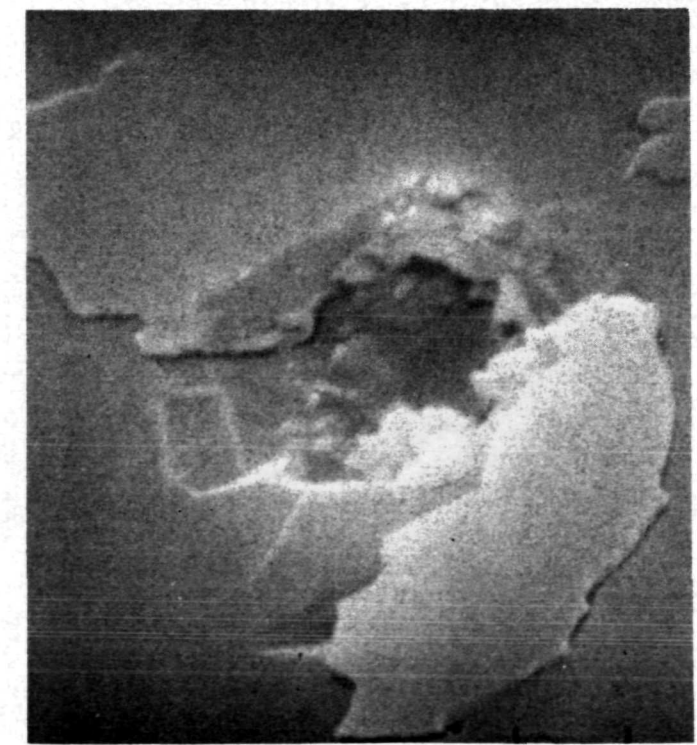
(c)



(d)



(e)



(f)

FIGURE 4-14. Photographs of Craters from Normal Impacts of Iron Particles on Diopside at 3.06 km/s:  
(a); crater D-1. (b); crater D-6. (c); crater D-7. (d); crater D-8. (e); crater D-9. (f); crater D-11.  
All have one micron index separation and 25° tilt angles.

Figure 4-15 shows six craters in biotite mica produced at the same 3.06 km/s average velocity. The crater structure is made very interesting in these photos due to the laminar structure of the mica. The impacting particles are believed to be in the bottoms of the crater pits. A considerable amount of melt is in evidence by the number of droplets seen on the crater walls.

Figure 4-16 illustrates the craters obtained in hedenbergite at 3.06 km/s.. Note that more extensive spallation occurs with this material and that a considerable fraction of the spall plates developed are ejected from the surface. Again, droplets may be seen on the interior of the crater.

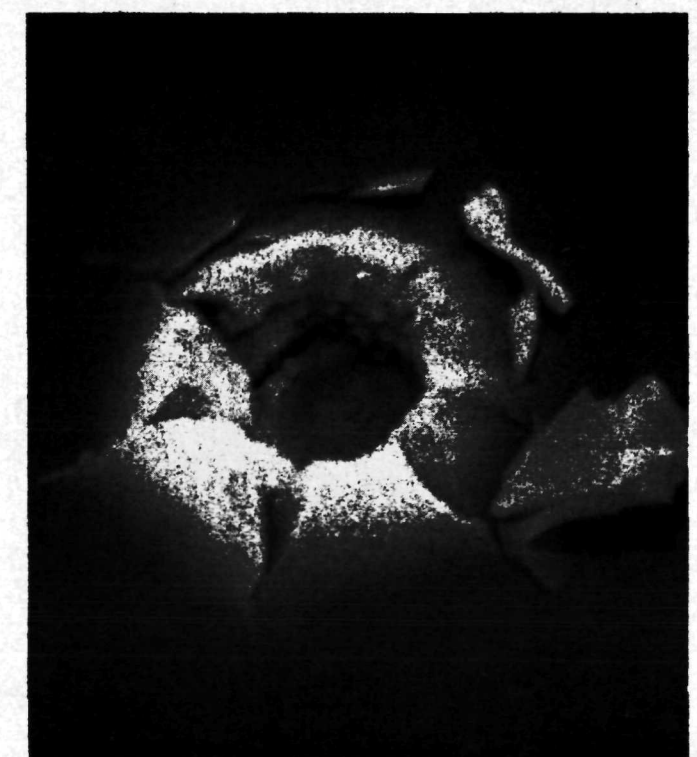
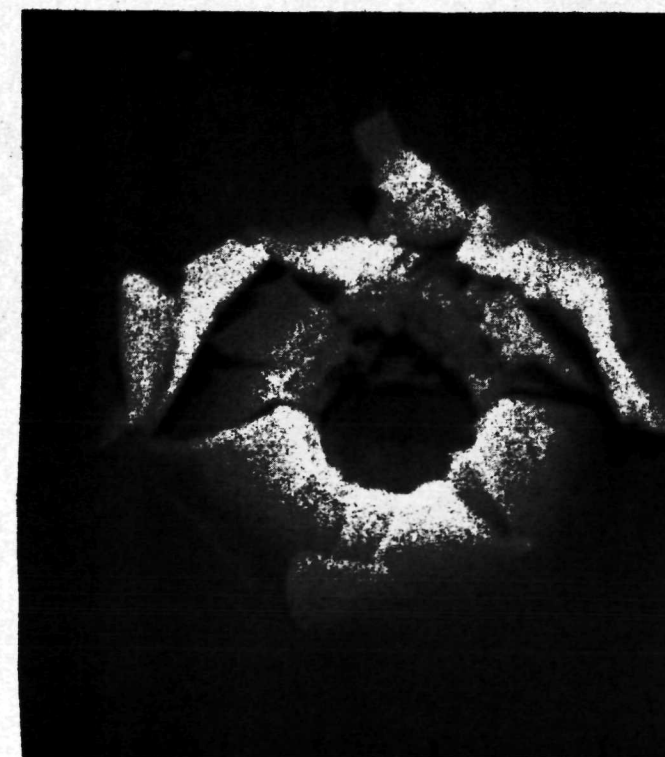
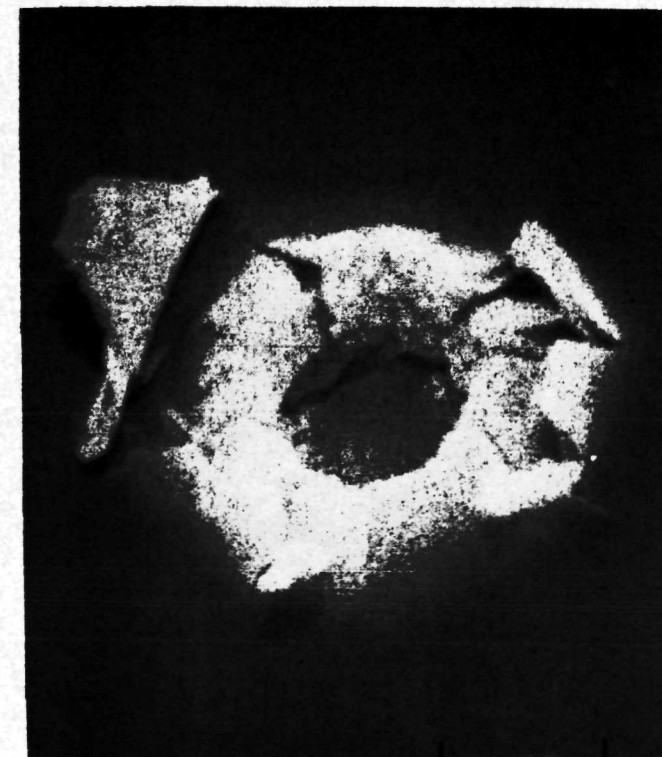
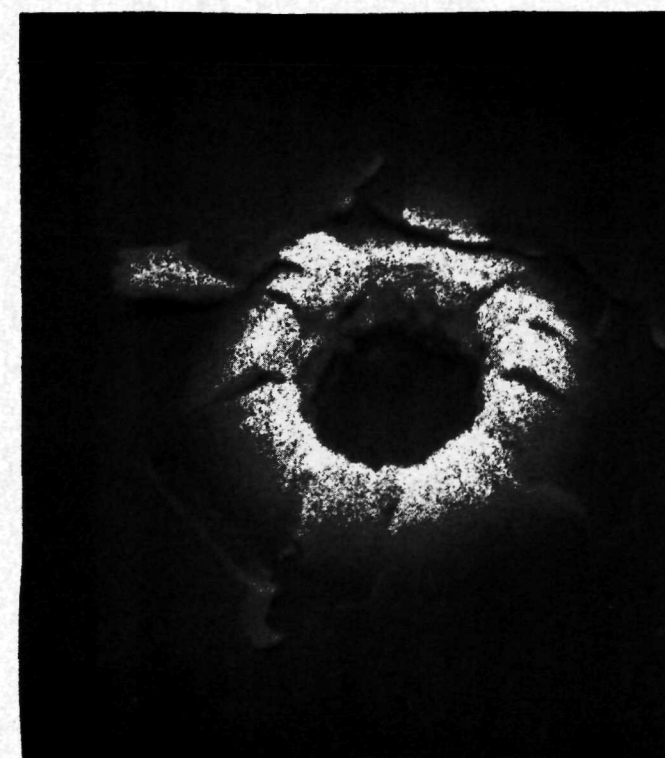
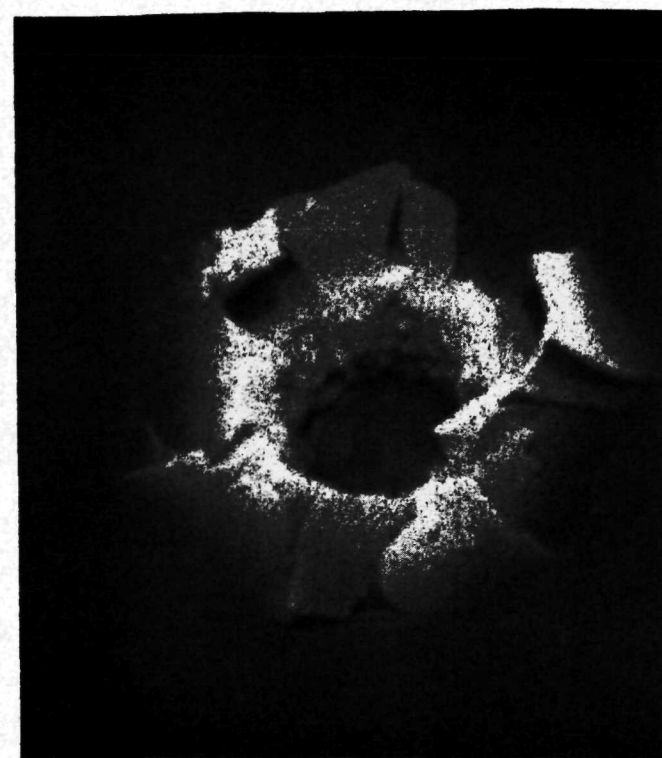
Photographs of six craters in ilmenite are shown in Figure 4-17. Again, the impact velocity was 3.06 km/s. Much less spallation occurs in this higher density material. No lip structure is seen probably because it has been spalled away. Also, there is very little evidence of melt in the crater.

Figure 4-18 contains photographs of six craters in monticellite formed at an impact velocity of 3.06 km/s. Whatever lip structure which may have been developed has been spalled away for the six craters shown. In addition to the small amount of spall around the central pit, much larger spall plates have been developed which apparently run quite deep into the material.

Figure 4-19 shows the results of six impacts in orthoclase at 3.06 km/s. Very large spallation plates were developed for each of the impacts shown. A well defined lip structure is present on all craters and large numbers of droplets may be seen in the interior.

#### 4.2.1.3 Photographs of 30° to Normal Oblique Impacts on Oligoclase

Particles having the same parameters as those used on the several minerals just described were also impacted into oligoclase at 30° to normal. Photographs for six of the craters produced (at 3.06 km/s) are

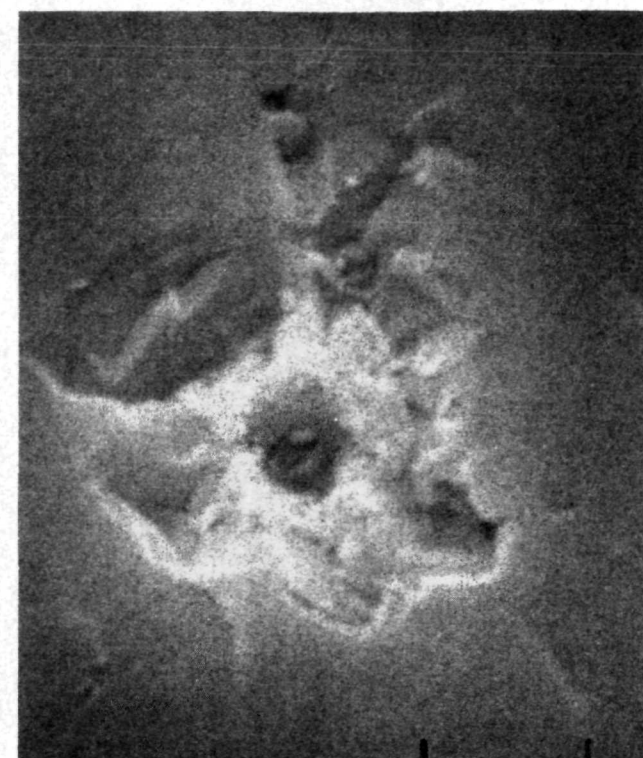


(d)

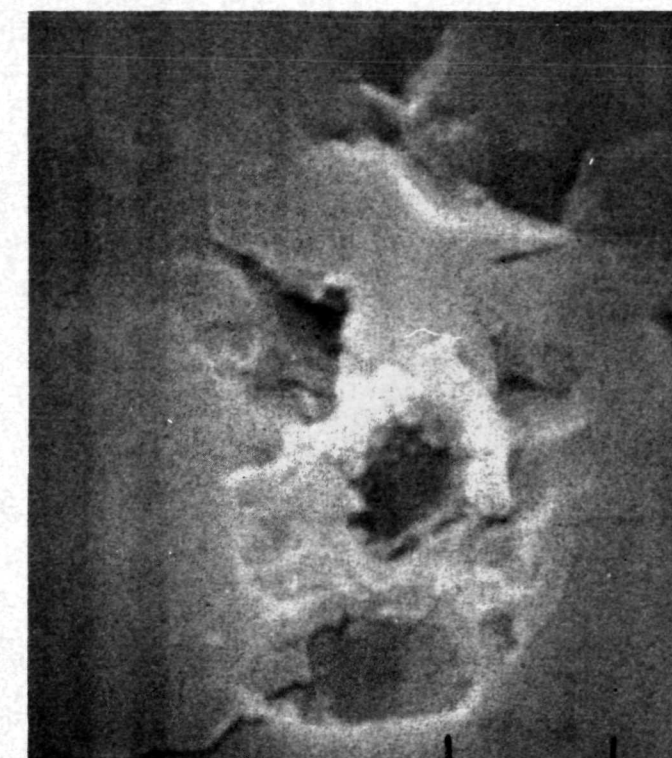
(e)

(f)

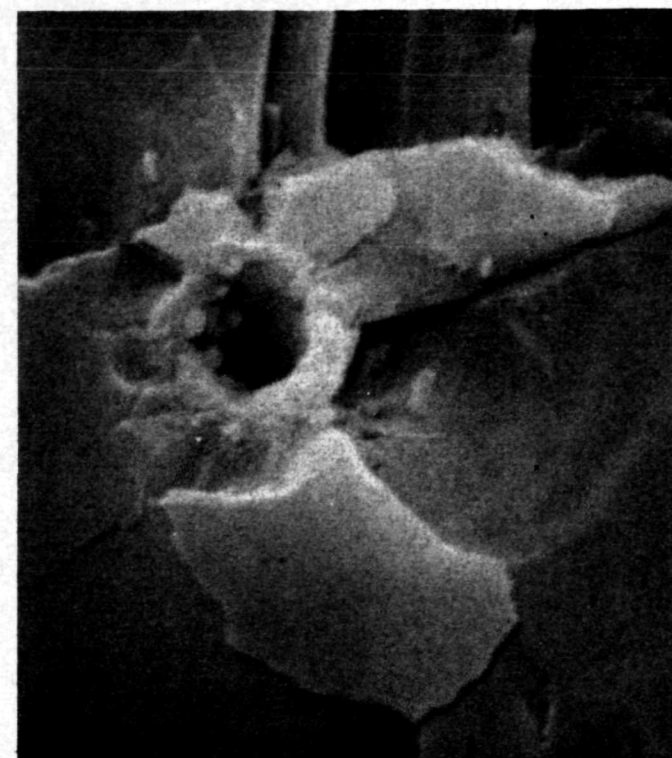
FIGURE 4-15. Photographs of Craters from Normal Impacts of Iron Particles on Biotite Mica at 3.06 km/s: (a) through (f) correspond to craters B-1 through B-6, respectively, all with 2 micron index mark separation and 25° tilt angle.



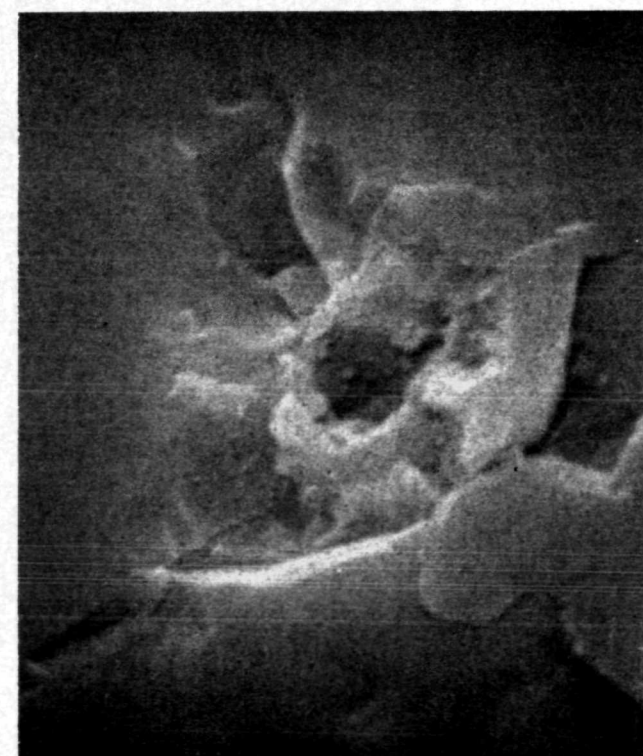
(a)



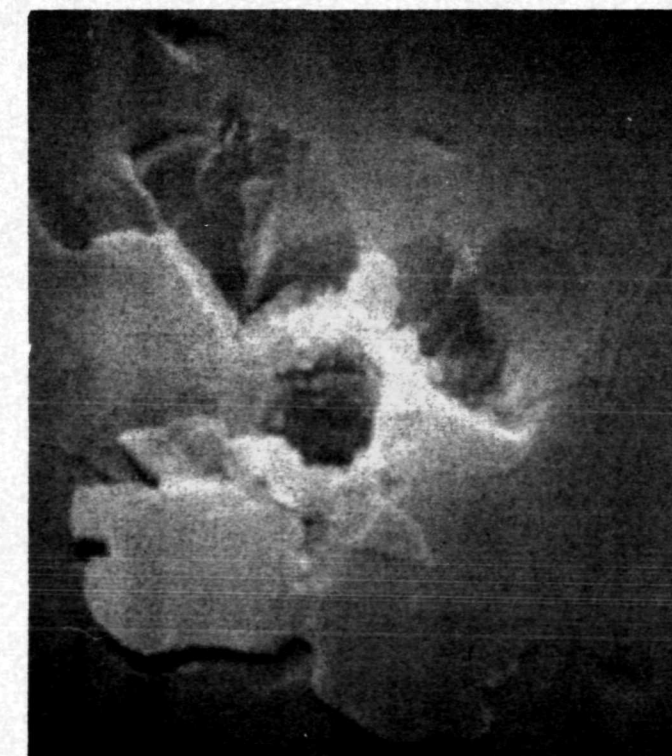
(b)



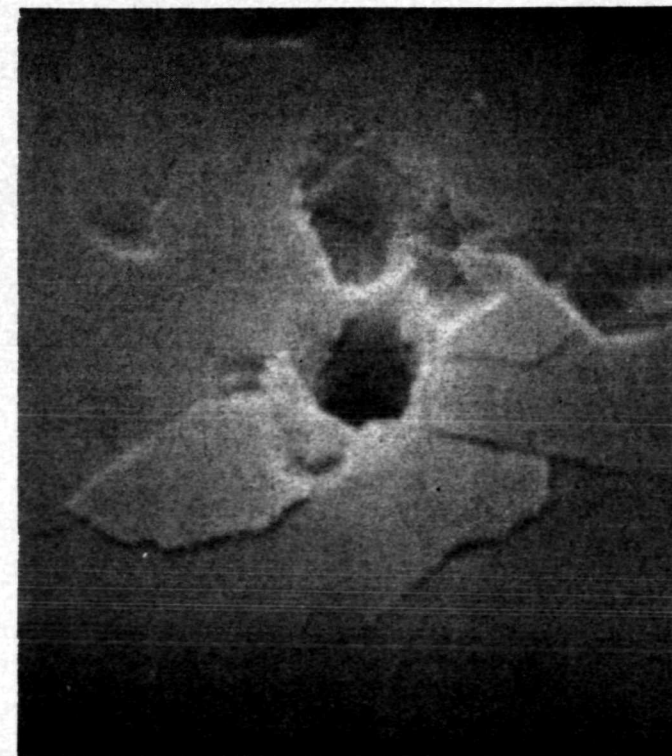
(c)



(d)

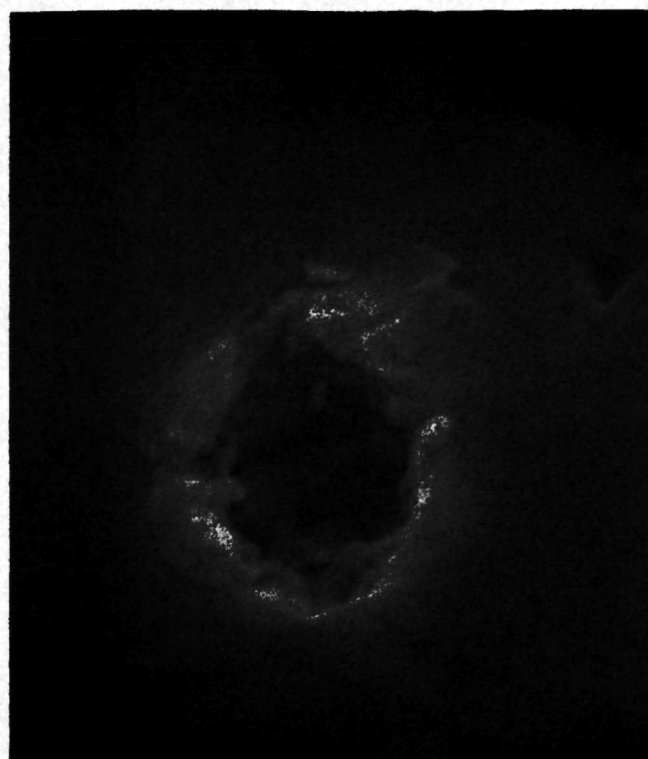


(e)

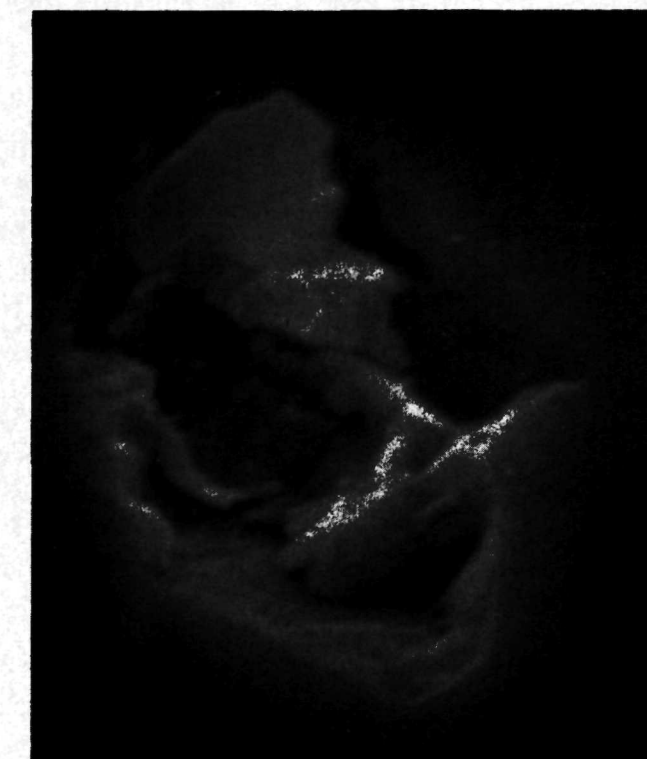


(f)

FIGURE 4-16. Photographs of Craters from Normal Impacts of Iron Particles on Hedenbergite at 3.06 km/s:  
(a) through (f) correspond to craters H-1 through H-6, respectively, all with 2 micron index  
mark separation and 25° tilt angle.



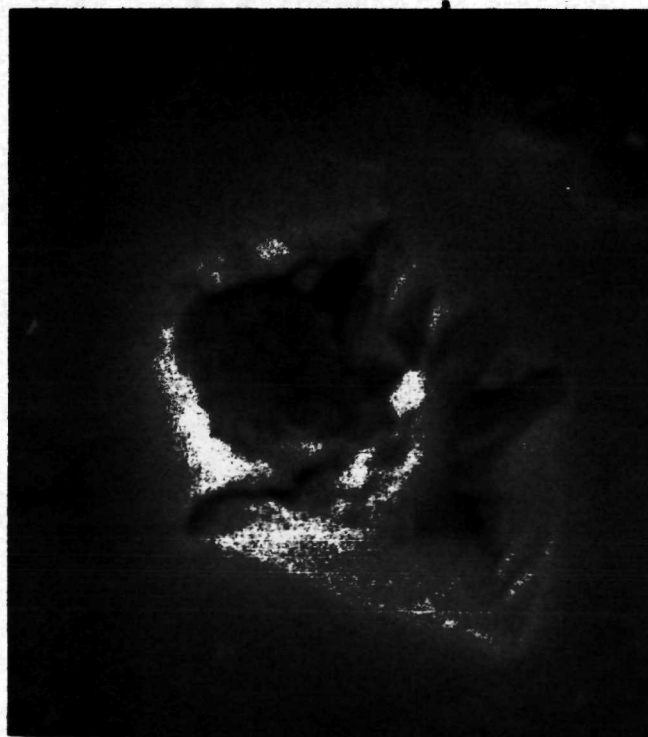
(a)



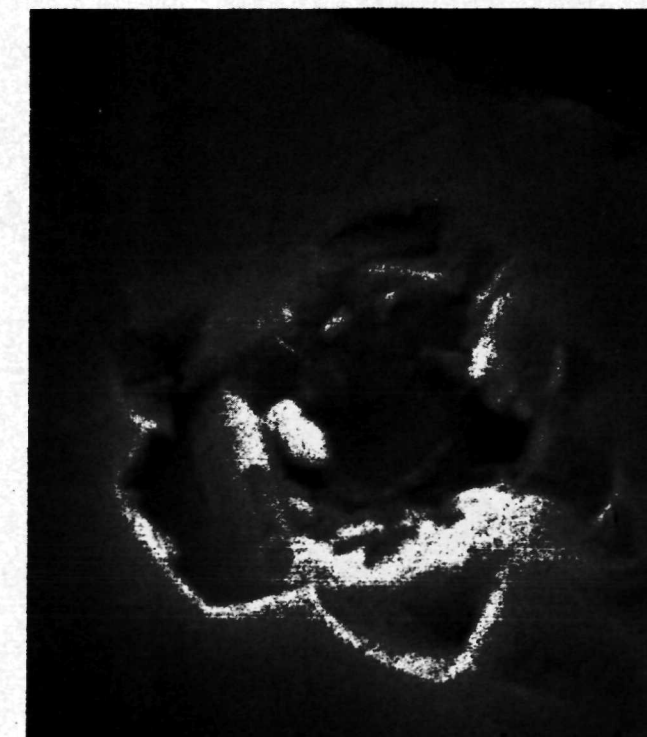
(b)



(c)



(d)

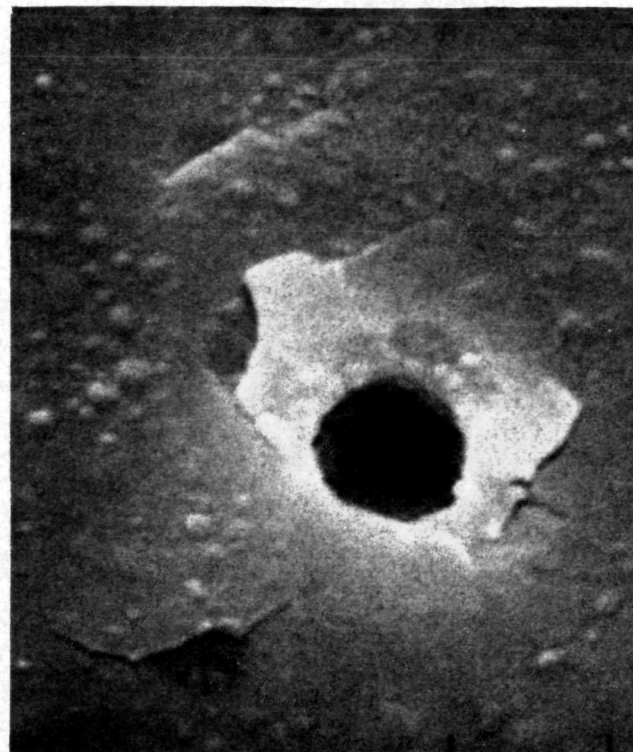


(e)

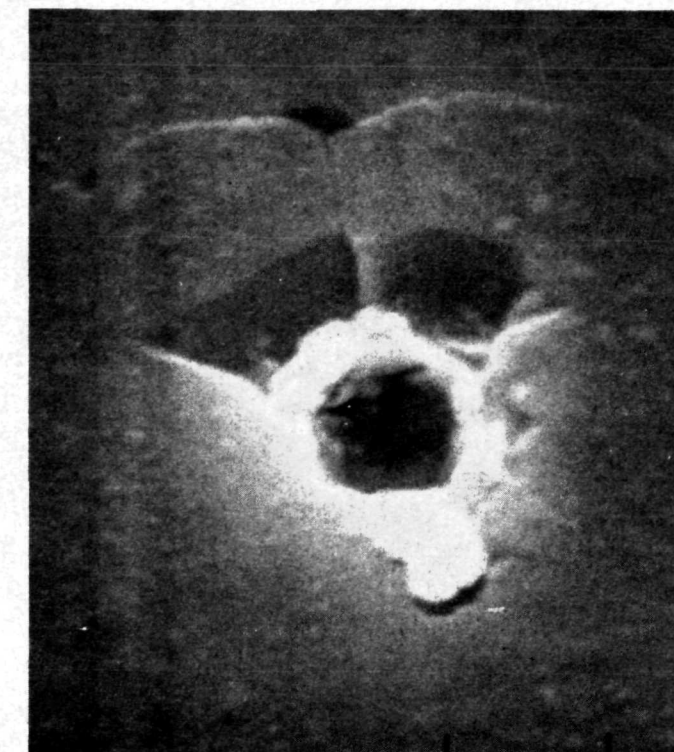


(f)

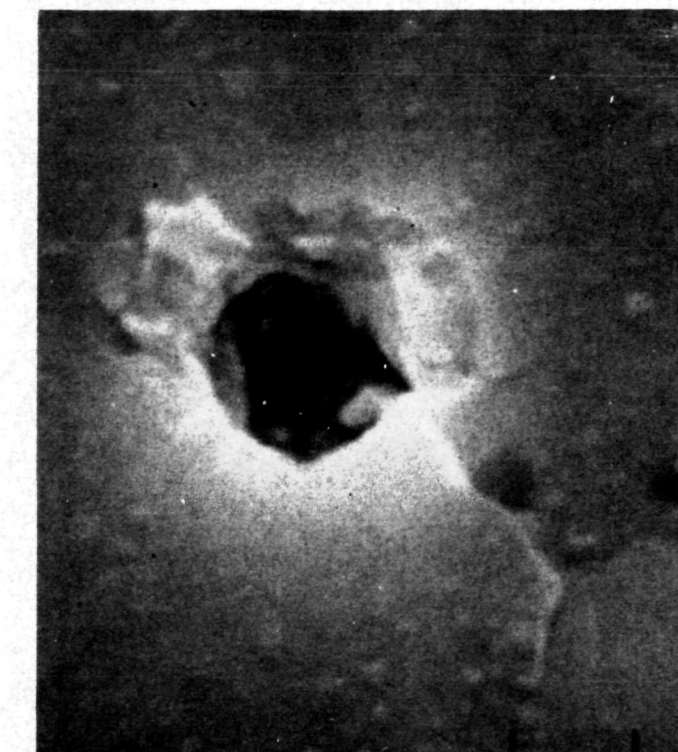
FIGURE 4-17. Photographs of Craters from Normal Impacts of Iron Particles on Ilmenite at 3.06 km/s: (a) through (e) correspond to craters I-1 through I-5, respectively. (f); crater I-7. All have one micron index mark separation and 25° tilt angle.



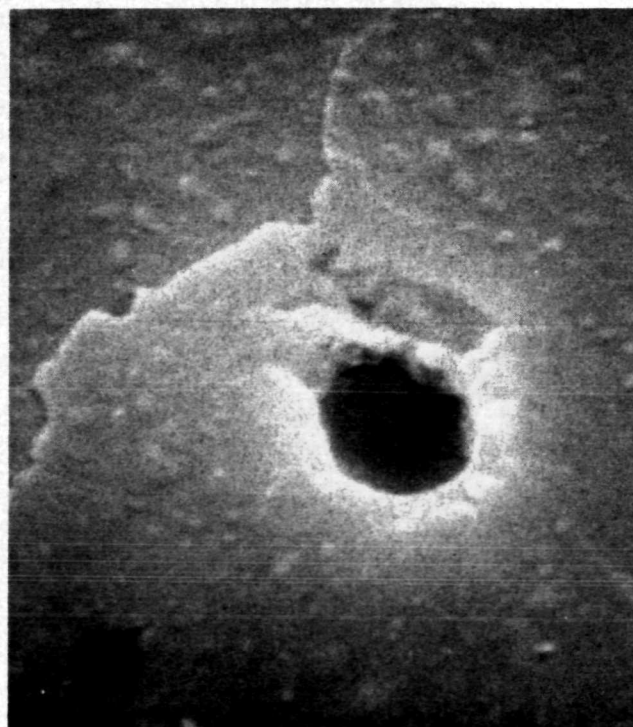
(a)



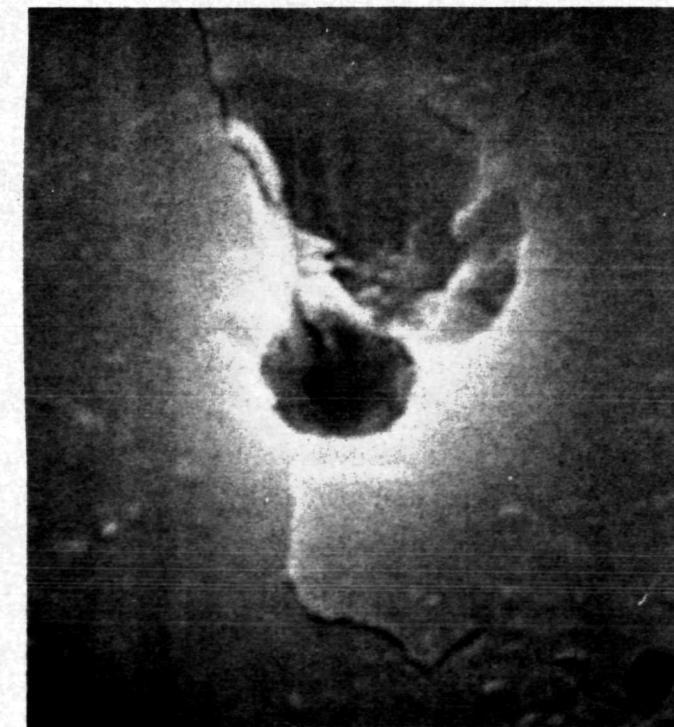
(b)



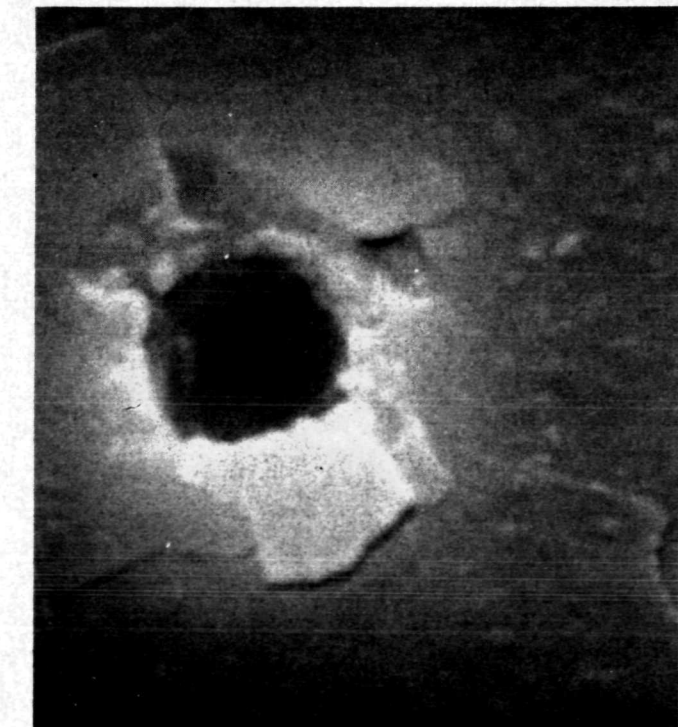
(c)



(d)

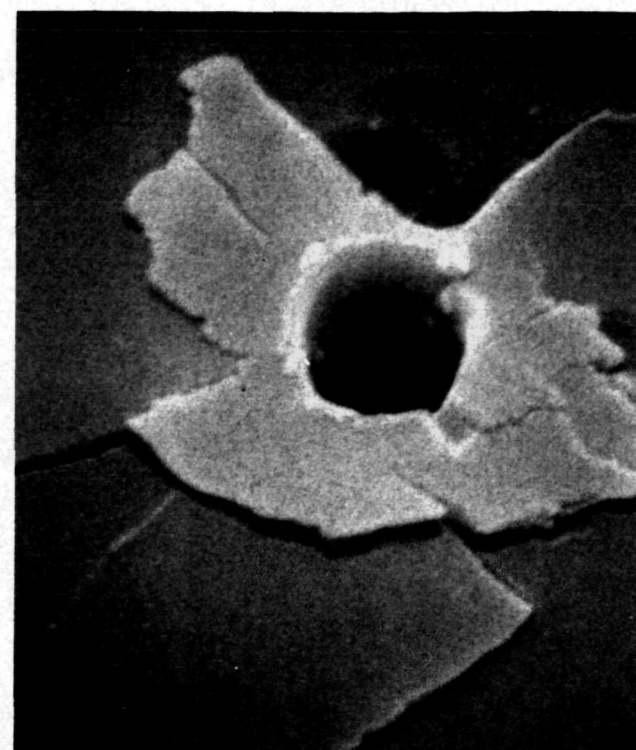


(e)

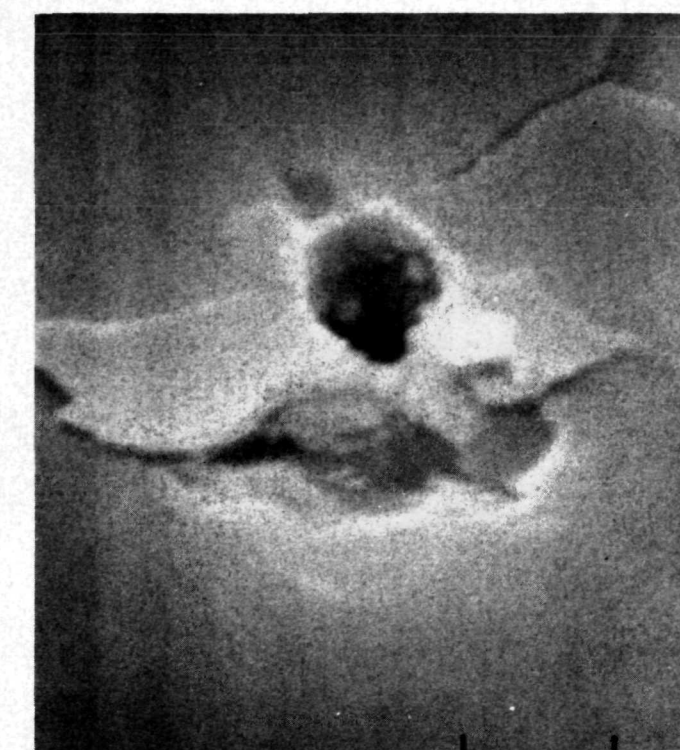


(f)

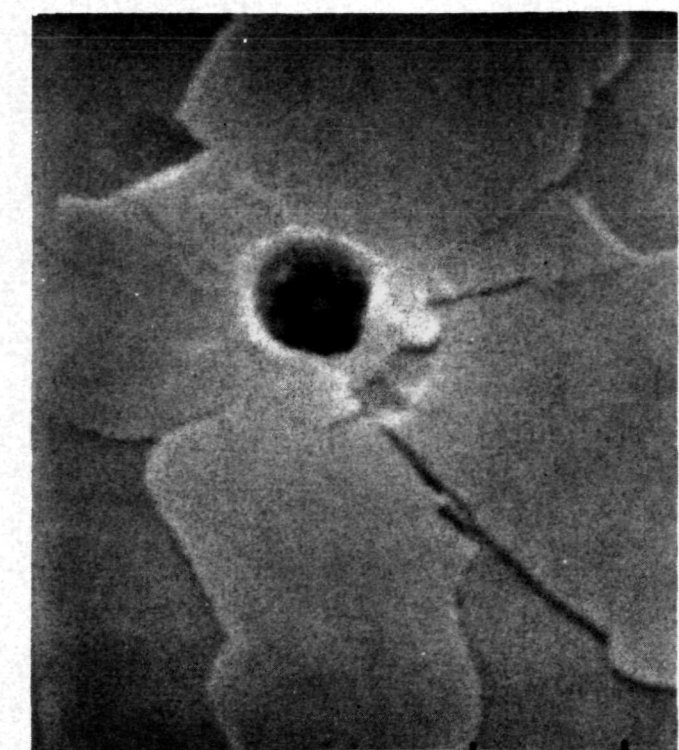
FIGURE 4-18. Photographs of Craters from Normal Impacts of Iron Particles on Monticellite at 3.06 km/s: (a) through (f) correspond to craters M-1 through M-6, respectively. (c) and (f) have one micron index marks while (a), (b), (d), and (e) have 2 micron index marks. All have 25° tile angles.



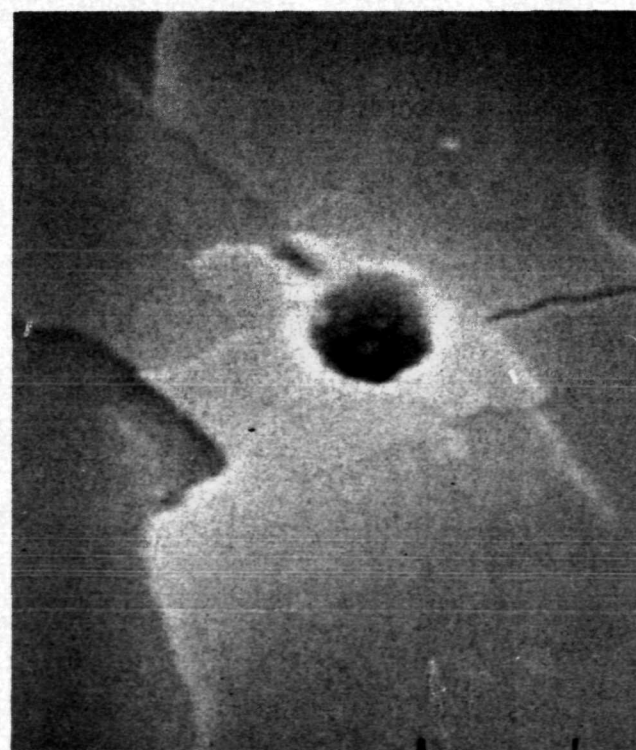
(a)



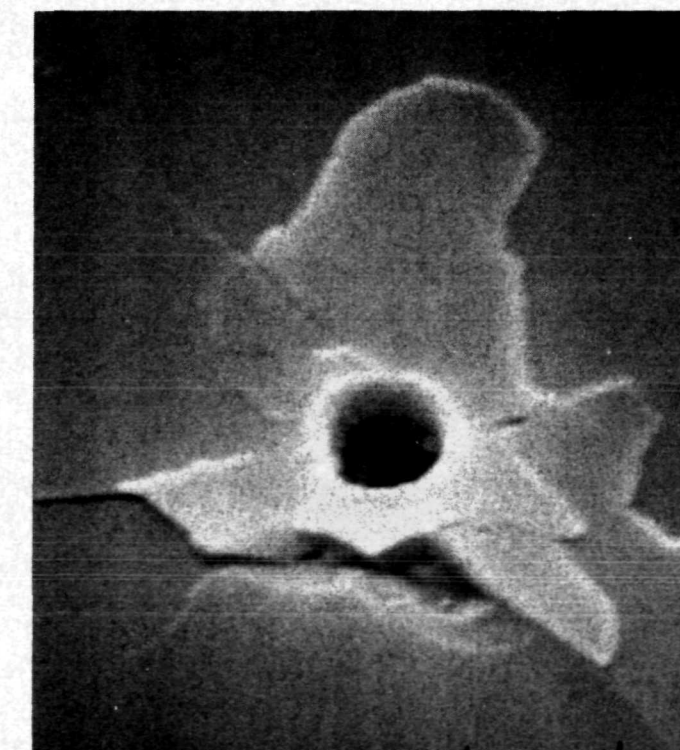
(b)



(c)



(d)



(e)



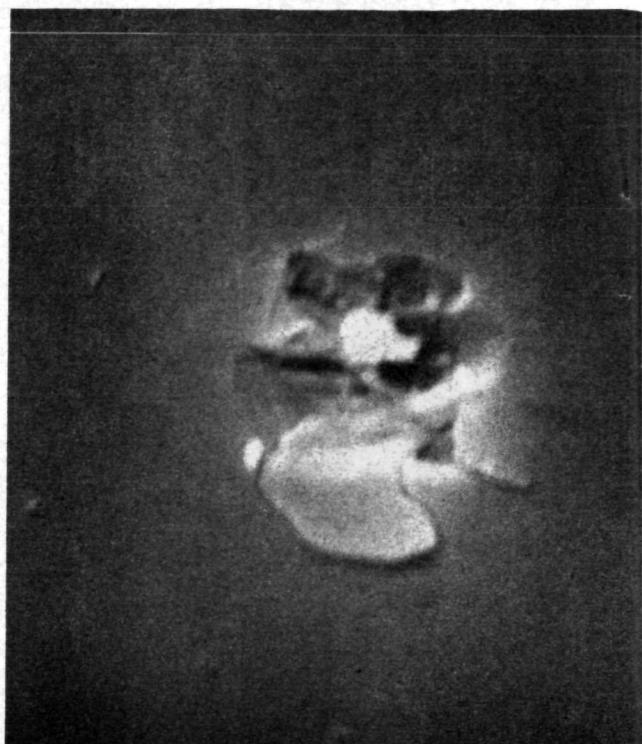
(f)

FIGURE 4-19. Photographs of Craters from Normal Impacts of Iron Particles on Orthoclase at 3.06 km/s:  
(a) through (f) correspond to craters 0-1 through 0-6, respectively. (a) has one micron  
index marks, all others have 2 micron index marks. All have 25° tilt angle.

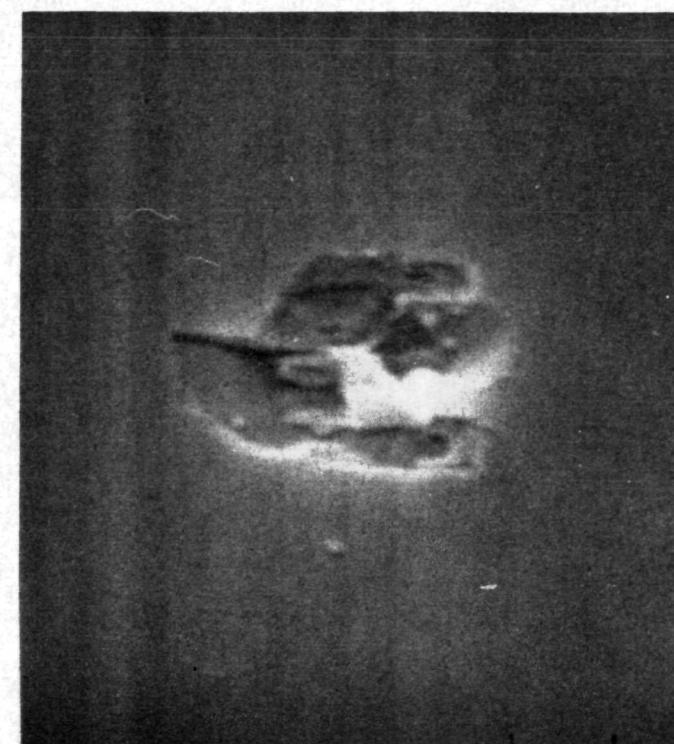
shown in Figure 4-20. These craters show a remarkable degree of consistency in the crater morphology. The direction of particle impact is from right to left on all oblique impact crater photographs. The particle impact direction and approximate angle may be easily deduced from the crater photos. Note that very little lip structure appears at the point of first contact and that spallation is clearly biased "downstream" as would be expected.

Representative examples of the data contained in Table 8, which are impacts at 30° to normal in oligoclase, are shown in Figure 4-21 and 4-22. The eight craters shown in Figure 4-21 span the velocity range 2.45 to 4.93 km/s and are arranged in order of ascending velocity. Extensive spallation occurred for all impacts in this figure. Note that the spall is biased "downstream" (toward the left) in all cases and that the degree of obliqueness of the particle impact is shown quite clearly by the angle at which the remains of the central pit enter the target. Spherules from the impact may be seen around several of the craters being most prominent around the crater in (c) which was an impact at 2.95 km/s.

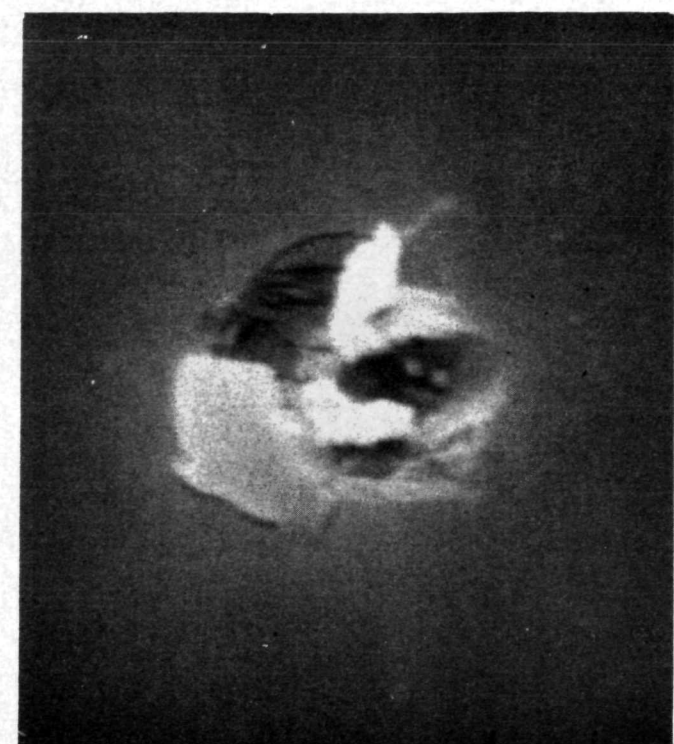
Figure 4-22 shows more 30° to normal oblique impacts. The impact velocity of this group ranges from 5.93 km/s in (a) to 27.9 km/s in (h). Spallation clearly diminishes with increasing velocity in this group. However, this may be a size effect and not a velocity effect since the size of the impacting particle diminishes dramatically with velocity. In Figure 4-22a, b, c, d, and e a large amount of spallation is present and is clearly biased in the direction of particle impact. In (f), (g), and (h) it is no longer obvious that these impacts are oblique. The outline around the crater is the result of the aluminum film being spalled away. The three higher velocity impacts exhibit a large melted lip structure and what appears to be smooth interior walls.



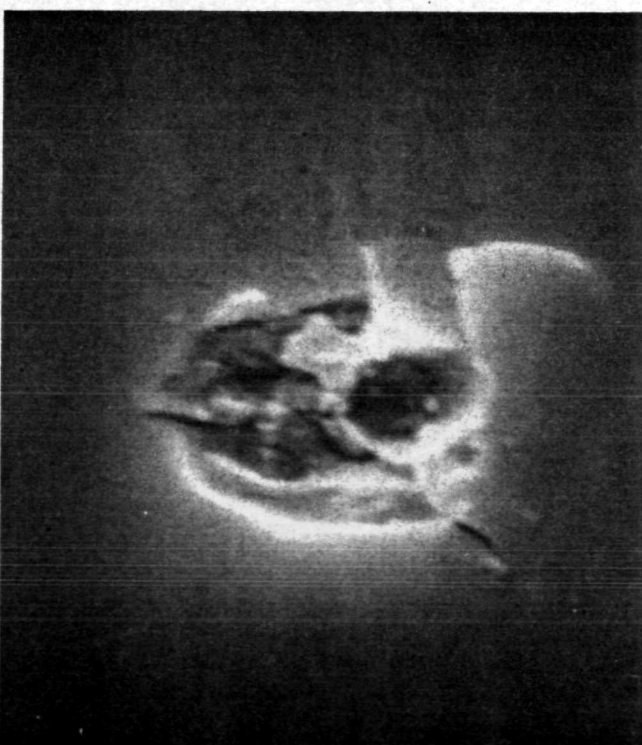
(a)



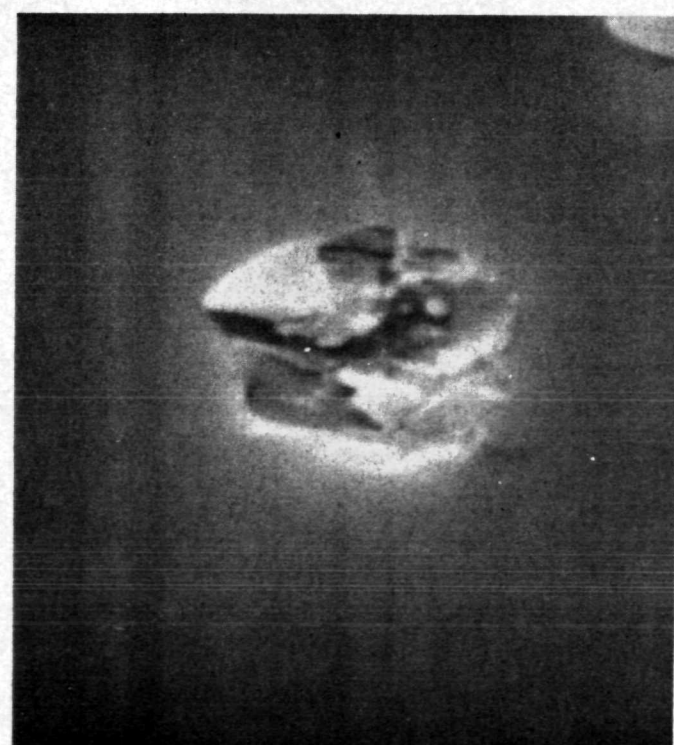
(b)



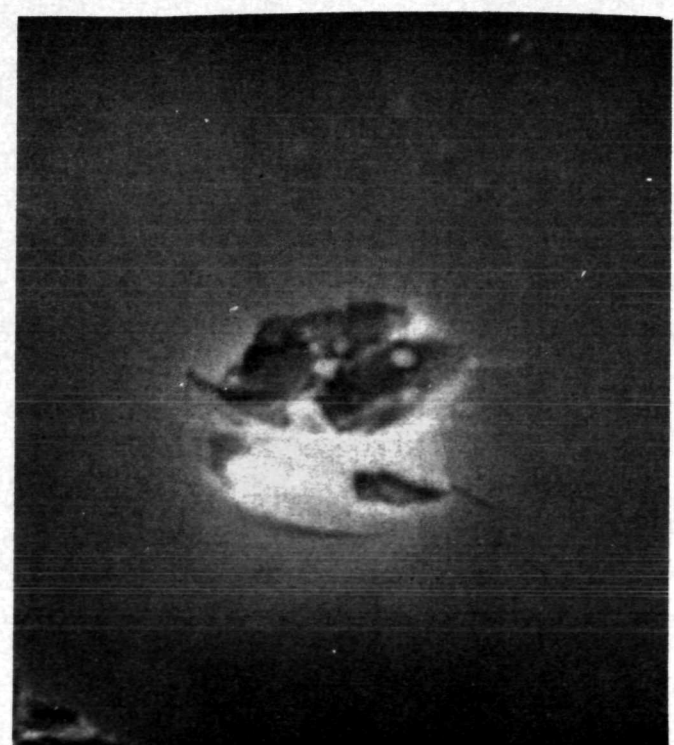
(c)



(d)



(e)

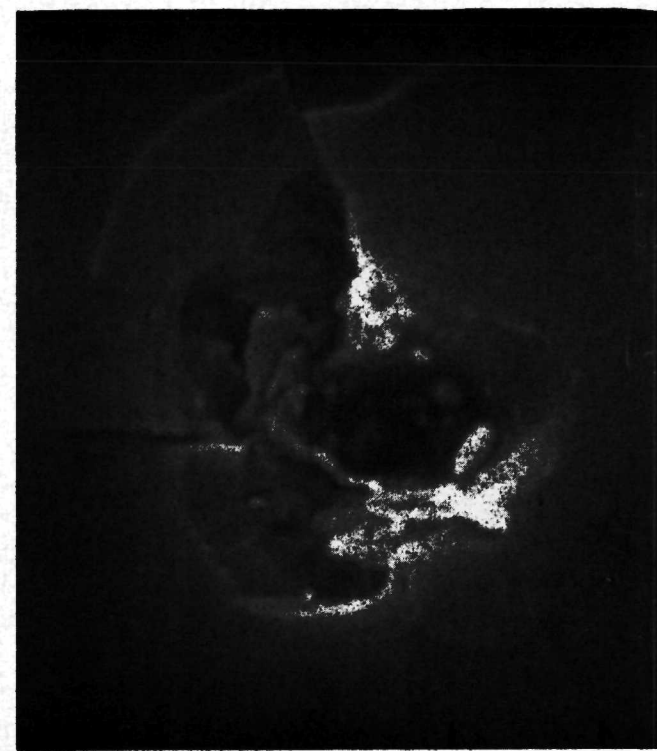


(f)

FIGURE 4-20. Photographs of Craters from  $30^\circ$  to Normal Oblique Impacts of Iron Particles on Oligoclase at 3.06 km/s: (a) through (f) correspond to craters S5-2-1 through S5-2-6, respectively. All have 2 micron index mark separation and  $20^\circ$  tilt angles.



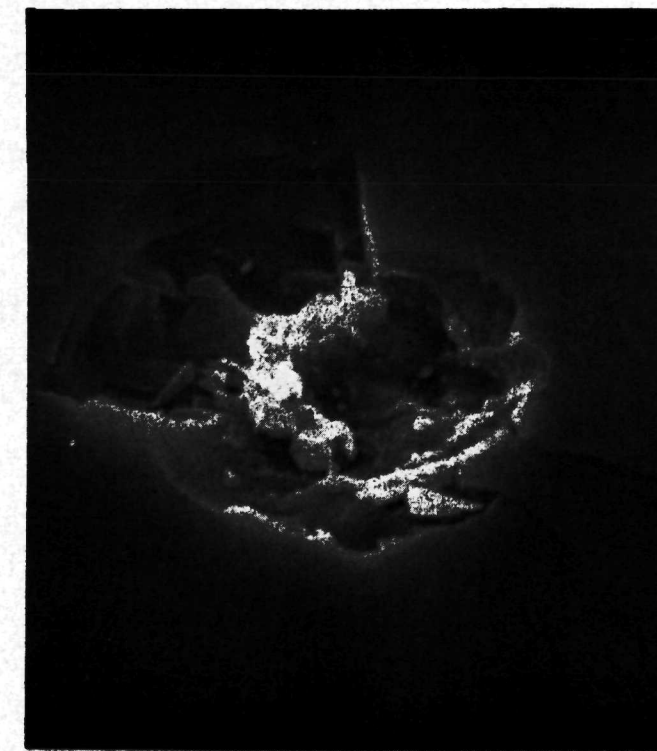
(a)



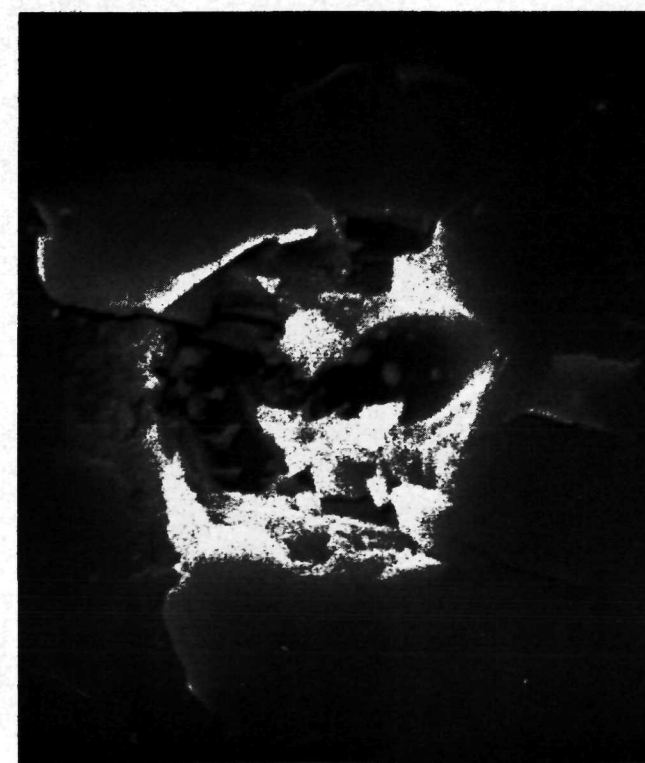
(b)



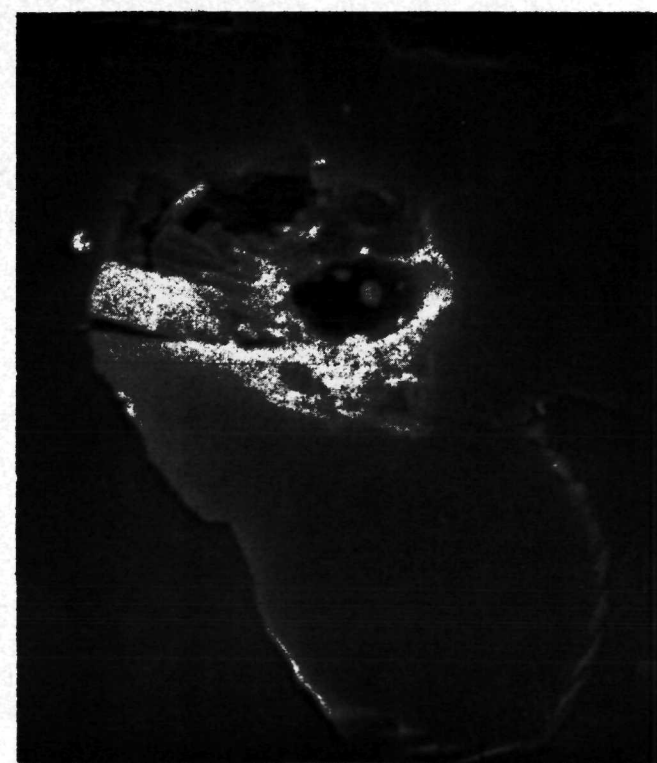
(c)



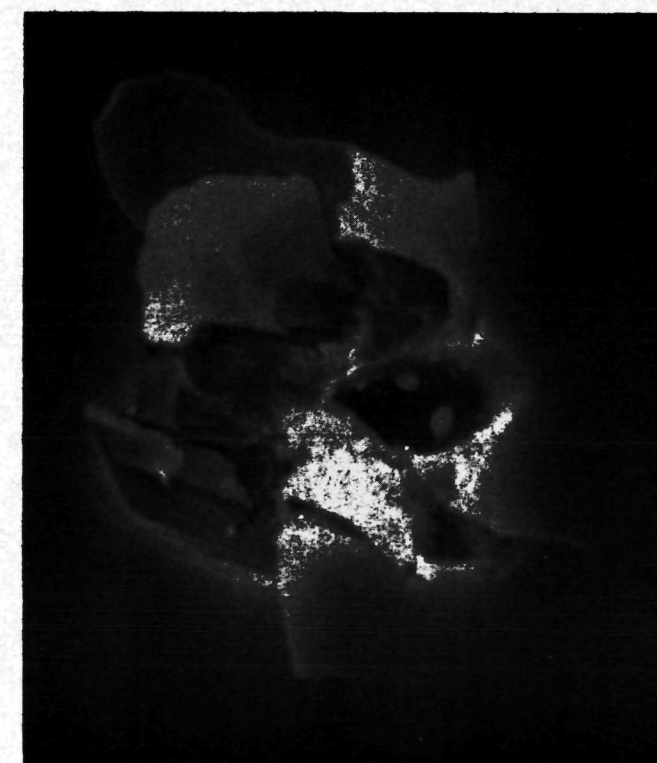
(d)



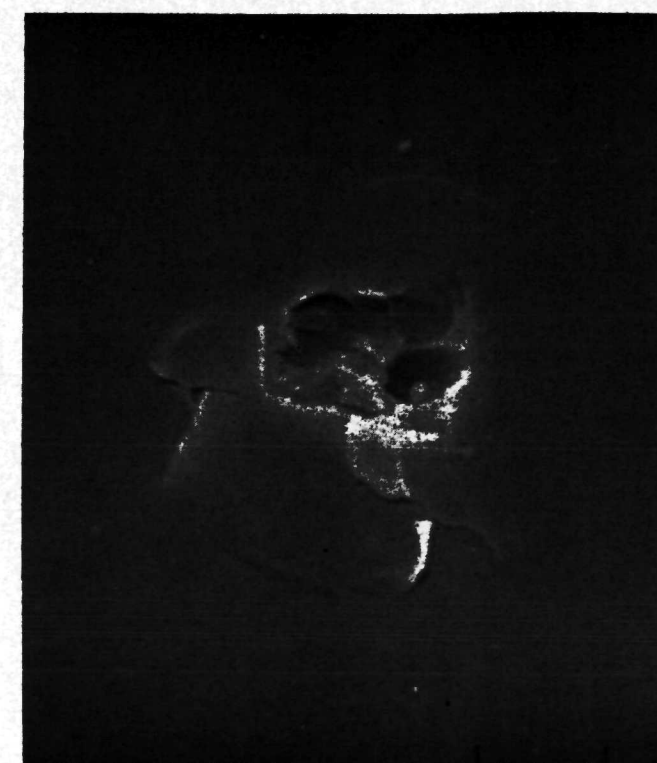
(e)



(f)

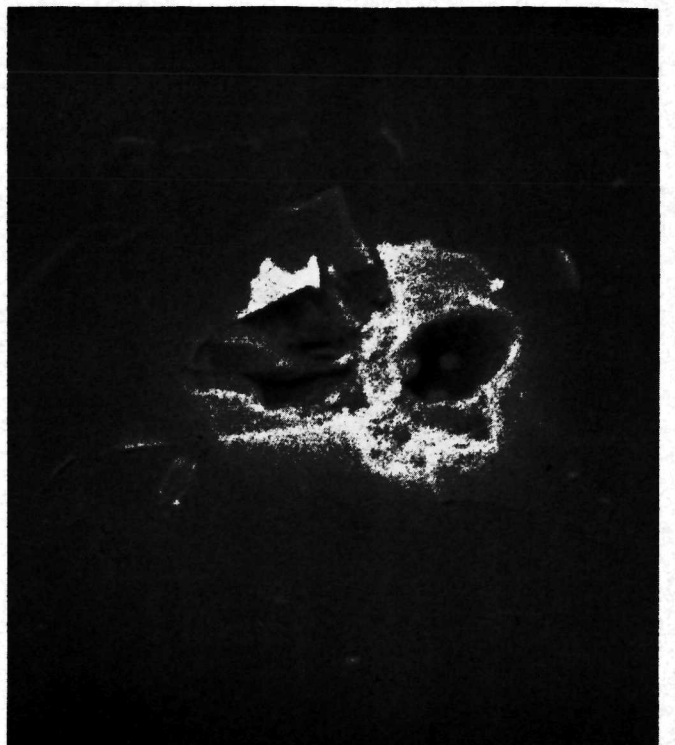


(g)

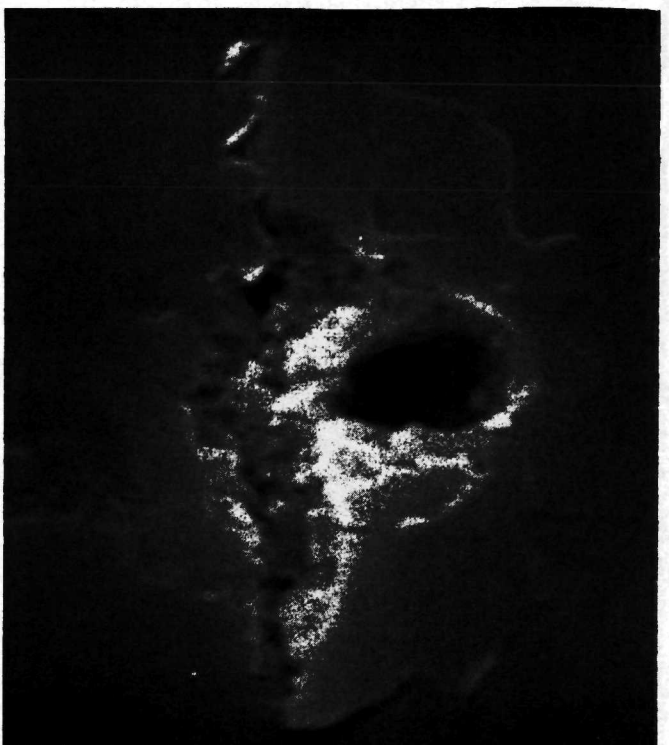


(h)

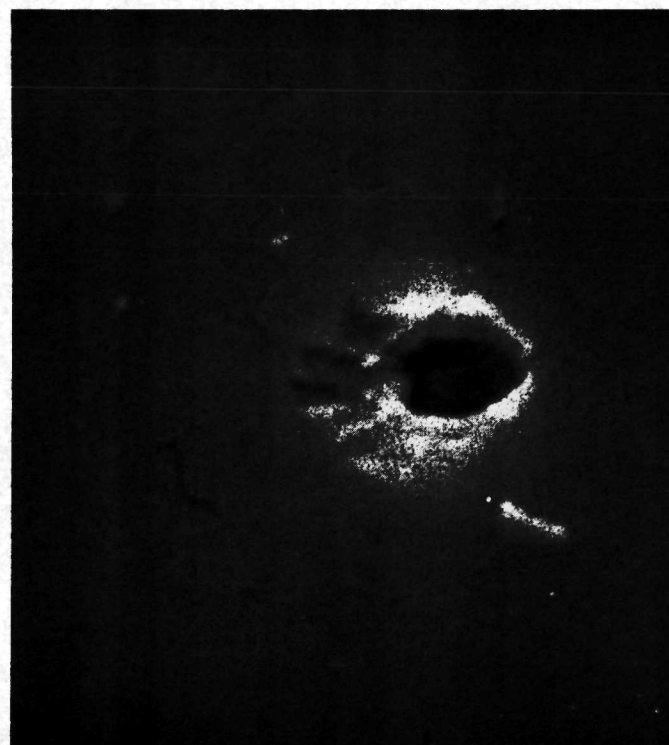
FIGURE 4-21. Photographs of Craters from 30° to Normal Oblique Impacts of Iron Particles on Oligoclase, 2.45 to 4.93 km/s: (a); crater S4-10-B, 2.45 km/s, 5 micron index marks. (b); crater S4-10-A, 2.52 km/s, 2 micron indexes. (c); crater S4-17-C, 2.95 km/s, 2 micron indexes. (d); crater S4-8-A, 3.21 km/s, one micron indexes. (e); crater S4-3-A, 4.22 km/s, 2 micron indexes. (f); crater S4-17-D, 4.35 km/s, one micron indexes. (g); crater S4-5-A, 4.38 km/s, one micron indexes. (h); crater S3-6-A, 4.93 km/s, one micron indexes. All have 20° tilt angles.



(a)



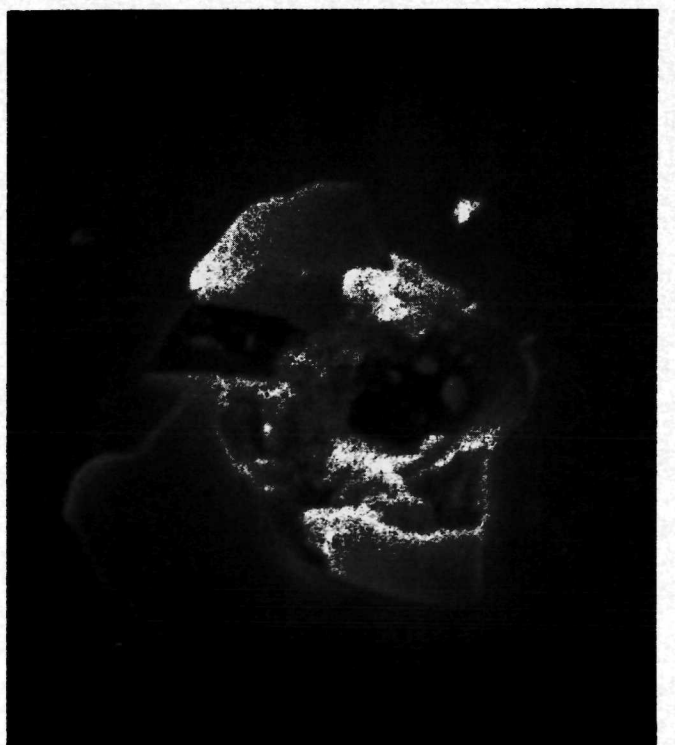
(b)



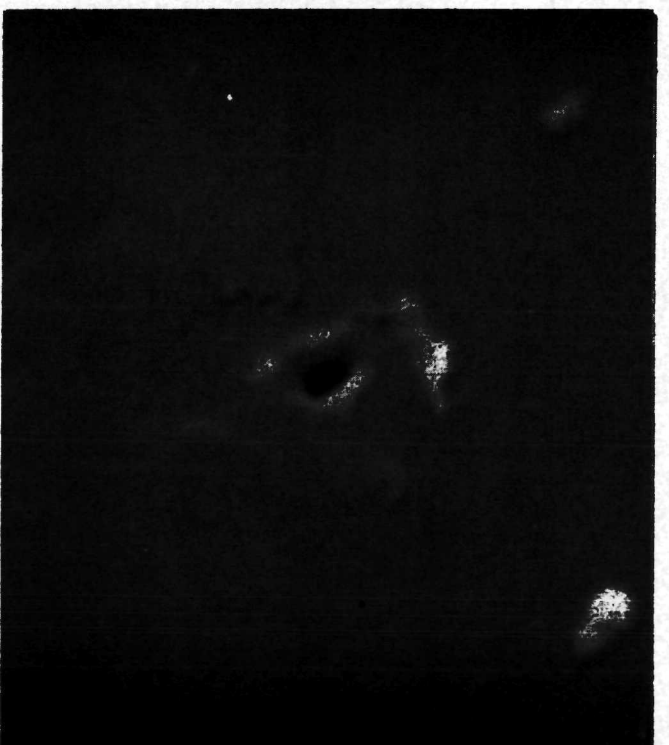
(c)



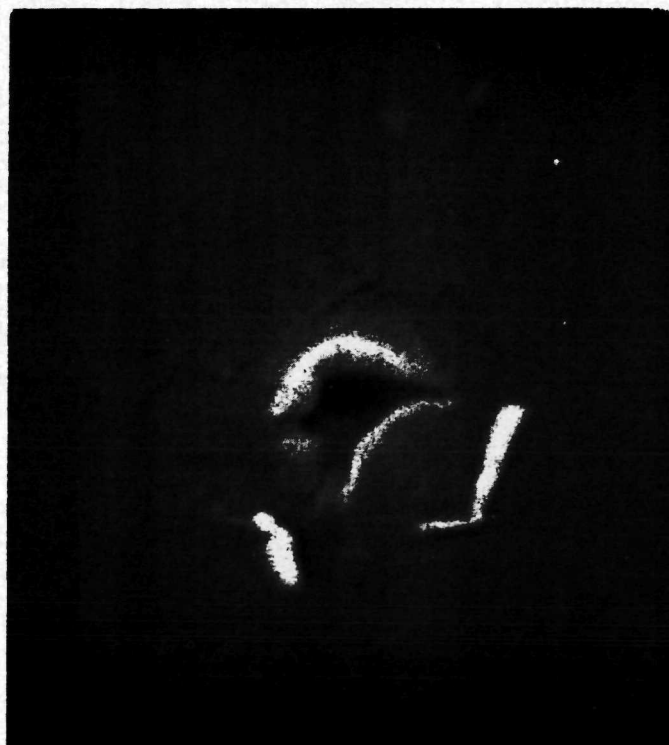
(d)



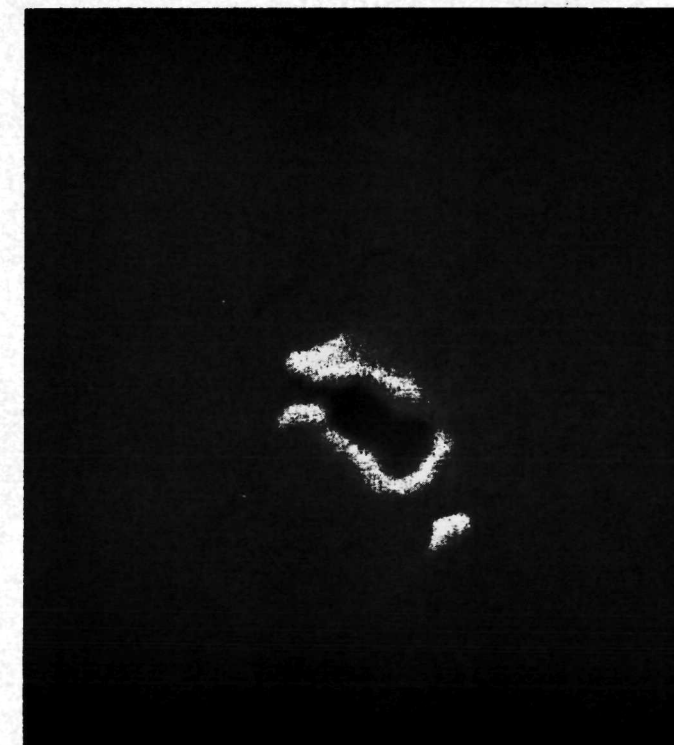
(e)



(f)



(g)



(h)

FIGURE 4-22. Photographs of Craters from  $30^\circ$  to Normal Oblique Impacts of Iron Particles on Oligoclase, 5.93 to 27.9 km/s: (a); crater S3-6-C, 5.93 km/s. (b); crater S3-11-A, 6.76 km/s. (c); crater S3-13-B, 8.35 km/s. (d); crater S3-10-A, 12.0 km/s. (e); crater S3-15-B, 13.1 km/s. (f); crater S4-1-C, 23.4 km/s. (g); crater S4-1-D, 23.4 km/s. (h); crater S4-1-E, 27.9 km/s. (b), (c), and (h) have 2 micron indexes, all others have 5 micron indexes. All have  $20^\circ$  tilt angles except (f), (g), and (h) which have  $12^\circ$  tilt angles.

#### 4.2.1.3 Photographs of 60° to Normal Impact Craters in Oligoclase

Figure 4-23 shows six craters produced by particles impacting at 3.06 km/s and at 60° to the target surface normal. These are the photo set for the data in Table 9. Increasing the angle of impact has materially reduced the degree of spallation which is biased strongly downstream. The shallow impact is easily deduced from the central pit structure.

Representative examples of the 60° oblique data of Table 10 are shown in Figures 4-24 and 4-25. Figure 4-24(a) shows a crater produced at 1.91 km/s while (h) shows an impact at 5.20 km/s. The intervening craters are arranged in order of ascending impact velocity. Almost no droplets are visible in (a) but are quite evident in the remaining pictures. Spallation is clearly biased downstream as for the previous set.

Table 4-25 covers the velocity range 6.57 to 26.1 km/s. The craters clearly show evidence of an oblique impact up to (e) which is 9.42 km/s. The craters shown in (f), (g), and (h) are all in the 20 km/s range and do not show as much of the oblique impact characteristics as do the lower velocity impacts.

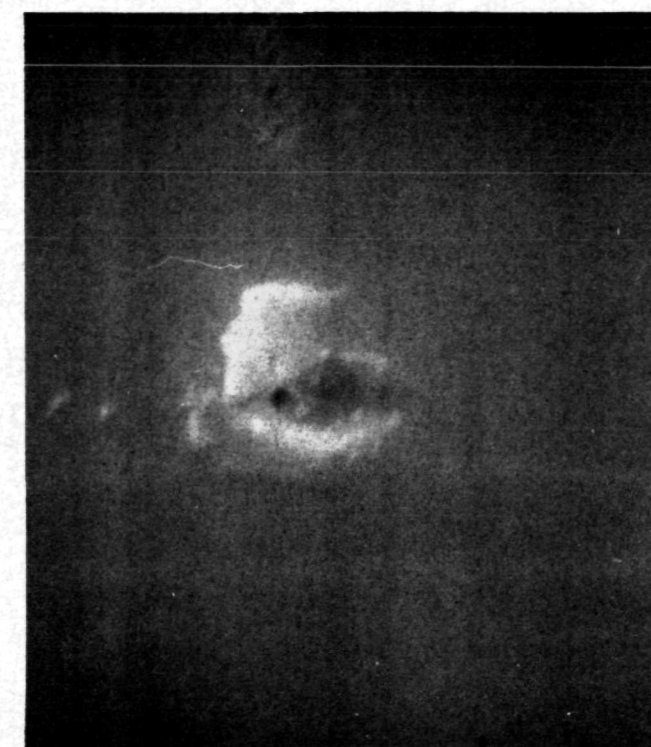
#### 4.2.2 Lanthanum Hexaboride Particle Impact Craters in Oligoclase

##### 4.2.2.1 Photographs of Normal Impact Craters

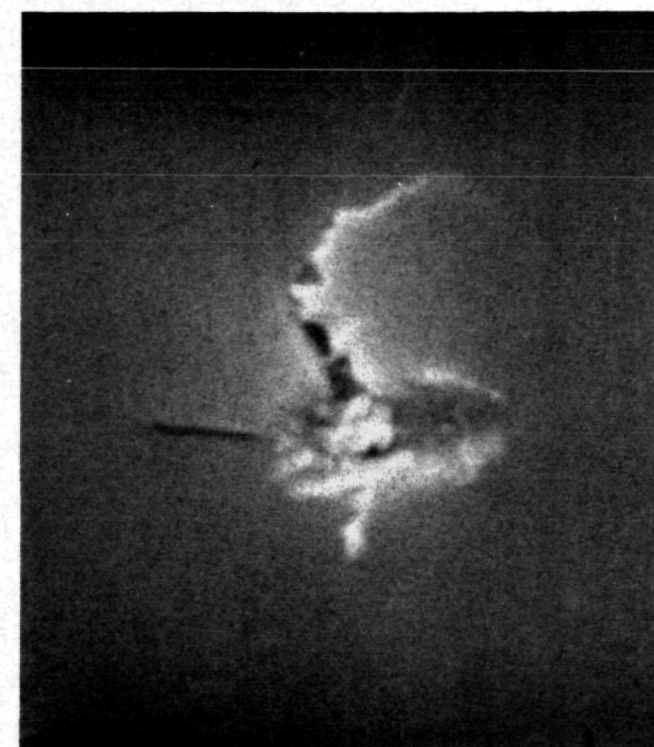
Representative crater photographs from the data set of Table 11 are shown in Figures 4-26 and 4-27. Figure 4-26 covers the velocity range from 1.46 km/s to 5.12 km/s. A much lower degree of spallation is immediately evident from these low density particle impacts. Also the general irregularity of the particle shape can be seen in several of the photographs. The well defined lip structures and droplets seen for the iron particle impacts are not present here.



(a)



(b)



(c)



(d)

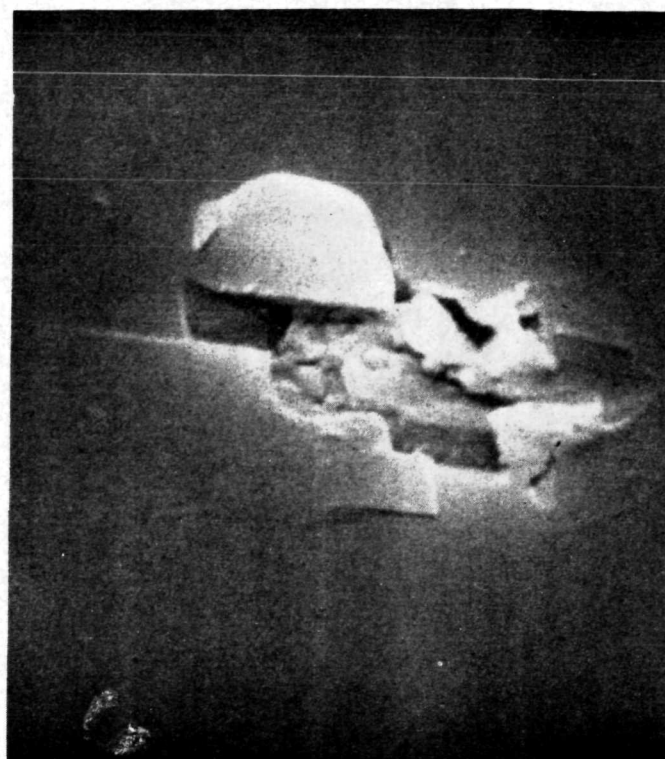


(e)

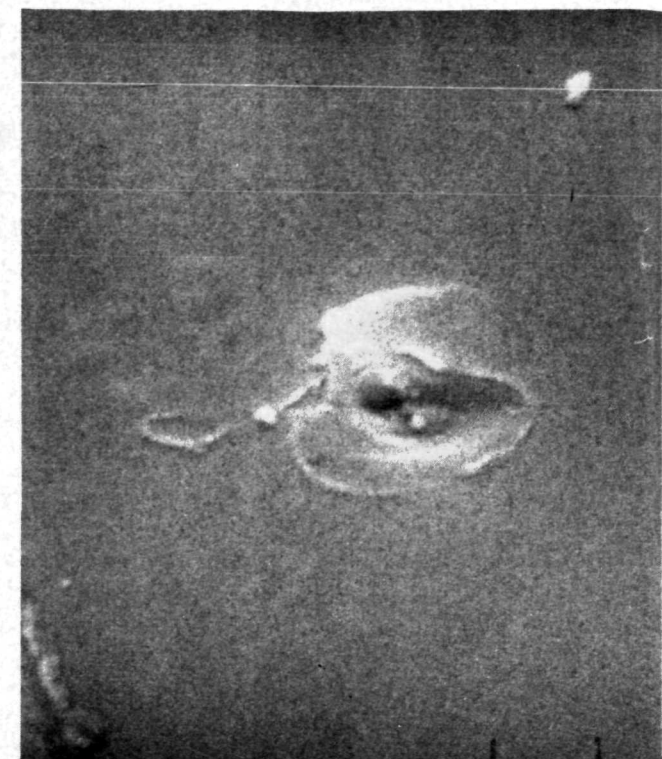


(f)

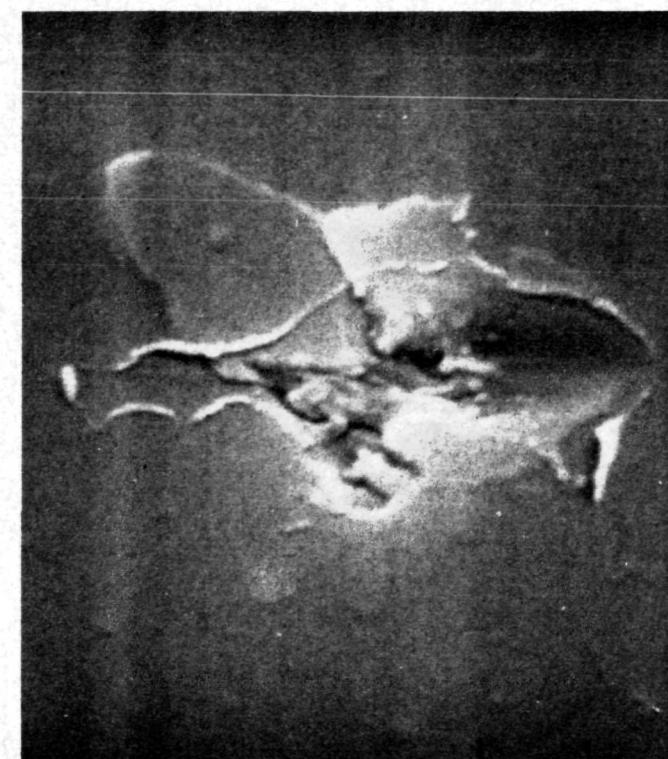
FIGURE 4-23. Photographs of Craters from  $60^\circ$  to Normal Oblique Impacts of Iron Particles on Oligoclase at 3.06 km/s. (a) through (f) correspond to craters S5-1-1 through S5-1-6, respectively. All have 2 micron index mark separation and  $9^\circ$  tilt angles.



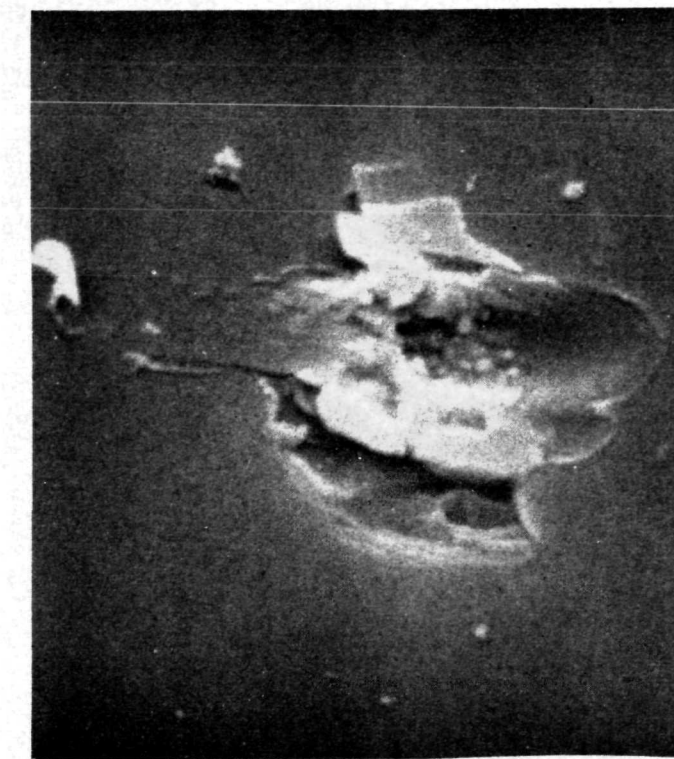
(a)



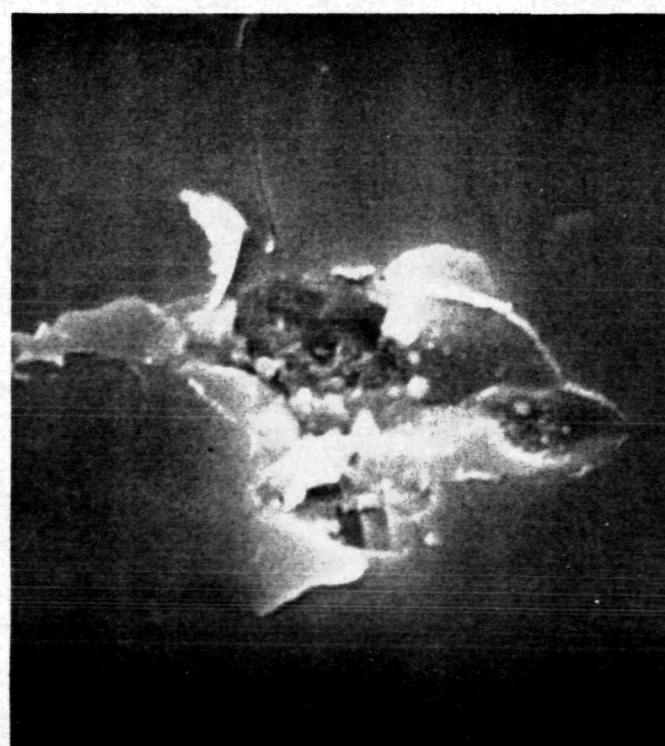
(b)



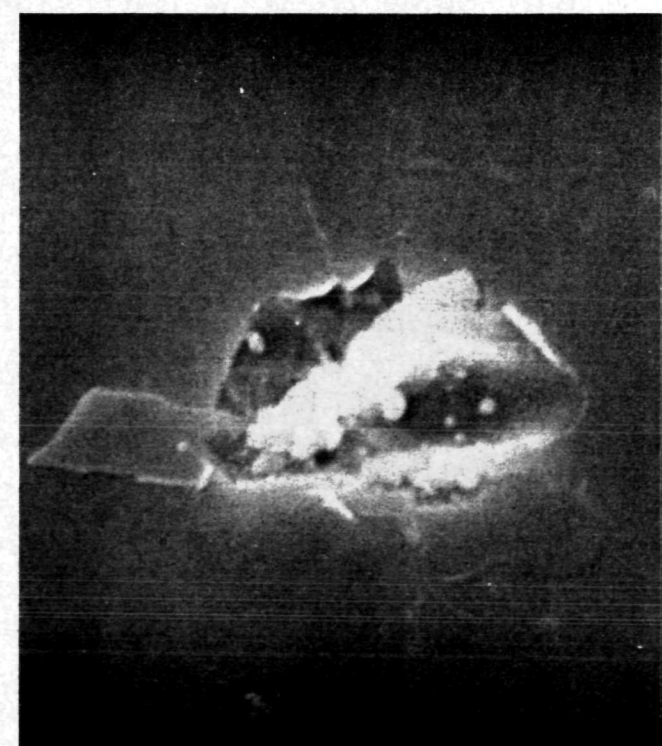
(c)



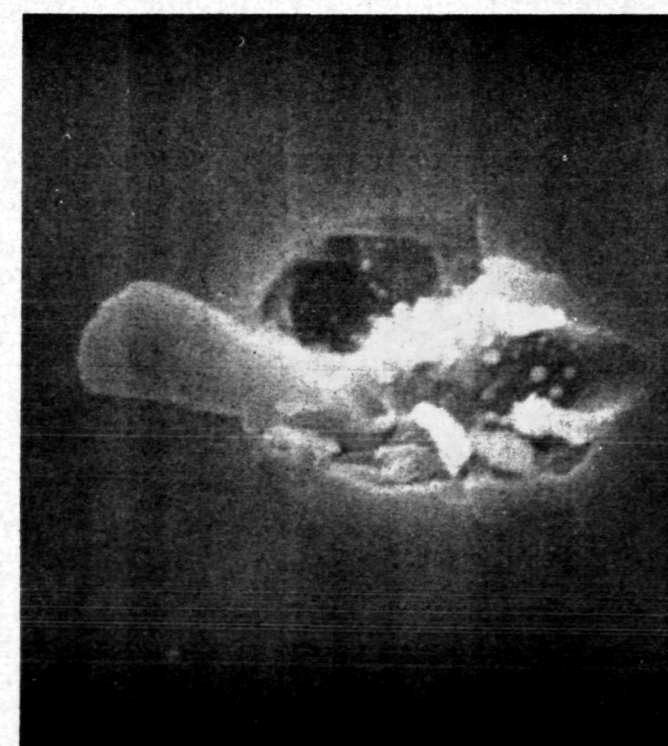
(d)



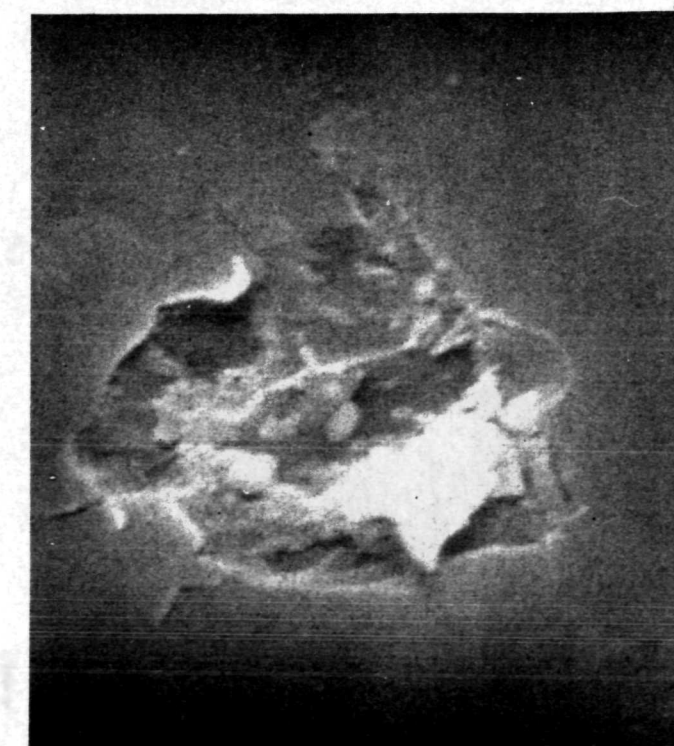
(e)



(f)



(g)

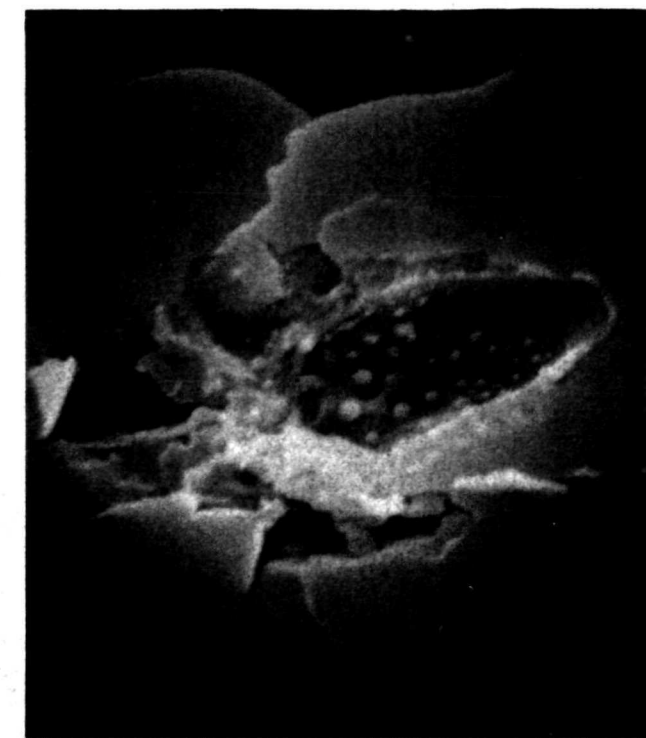


(h)

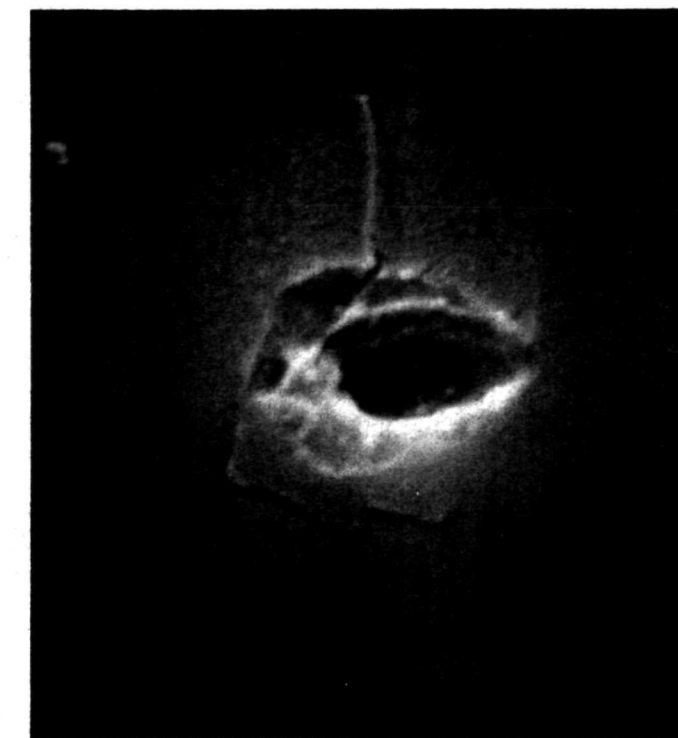
FIGURE 4-24. Photographs of Craters from 60° to Normal Oblique Impacts of Iron Particles on Oligoclase, 1.91 to 5.20 km/s: (a); crater S4-16-B, 1.91 km/s. (b); crater S4-16-c, 2.35 km/s. (c); crater S4-16-A, 2.64 km/s. (d); crater S4-11-A, 2.71 km/s. (e); crater S4-9-A, 3.16 km/s. (f); crater S4-4-A, 4.23 km/s. (g); crater S4-4-B, 4.50 km/s. (h); crater S3-12-A, 5.20 km/s. (b), (c), and (h) have 2 micron index marks, all others have 5 micron indexes. (d) has a 15° tilt angle, all others have 20° tilt angles.



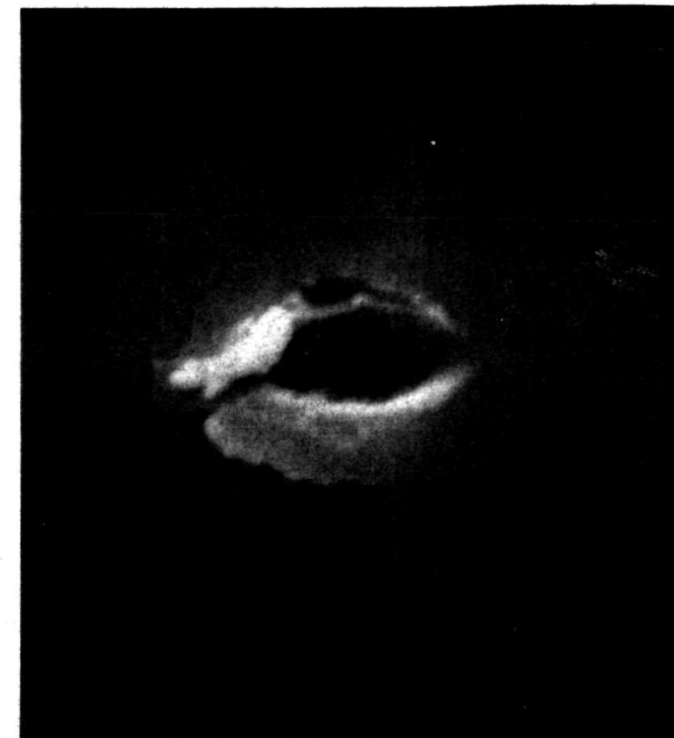
(a)



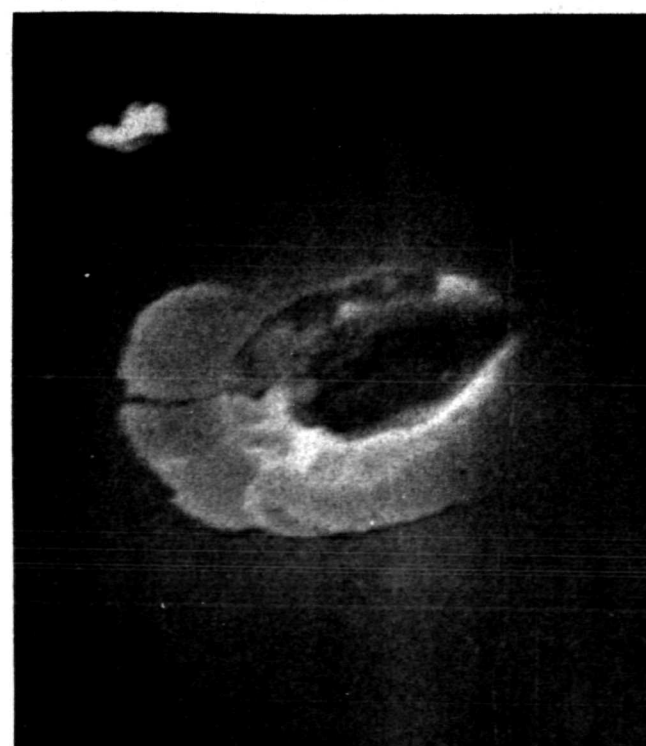
(b)



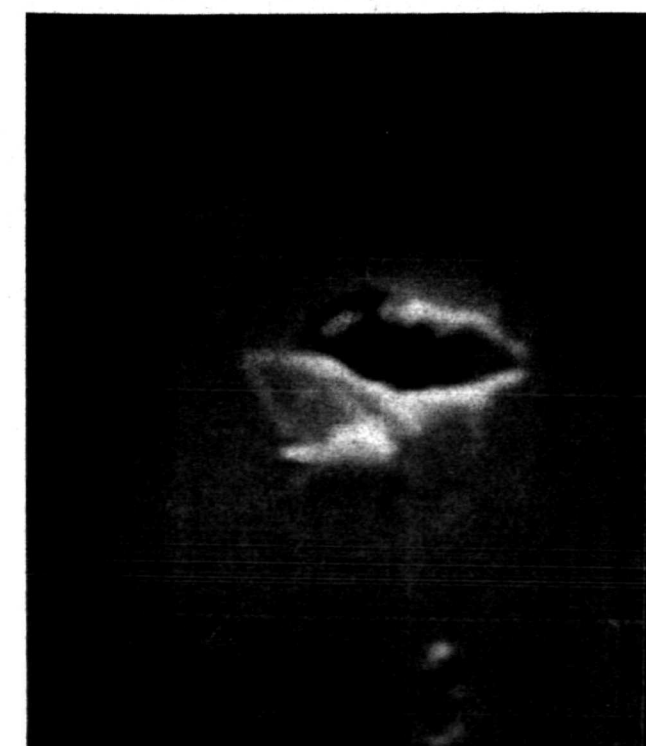
(c)



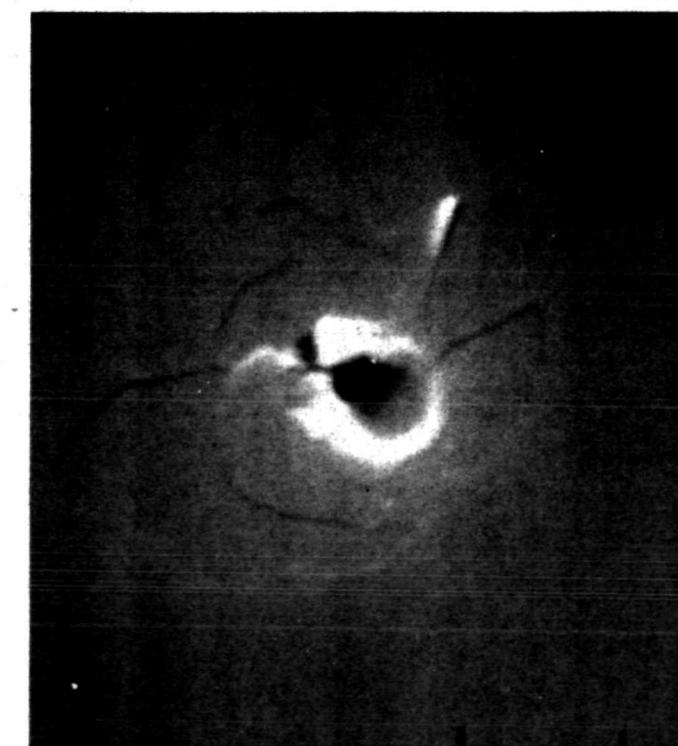
(d)



(e)



(f)



(g)

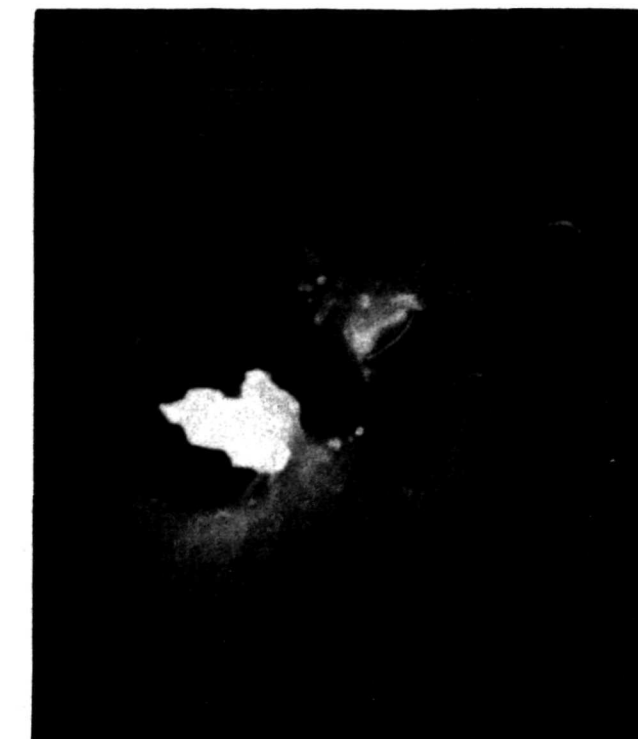


(h)

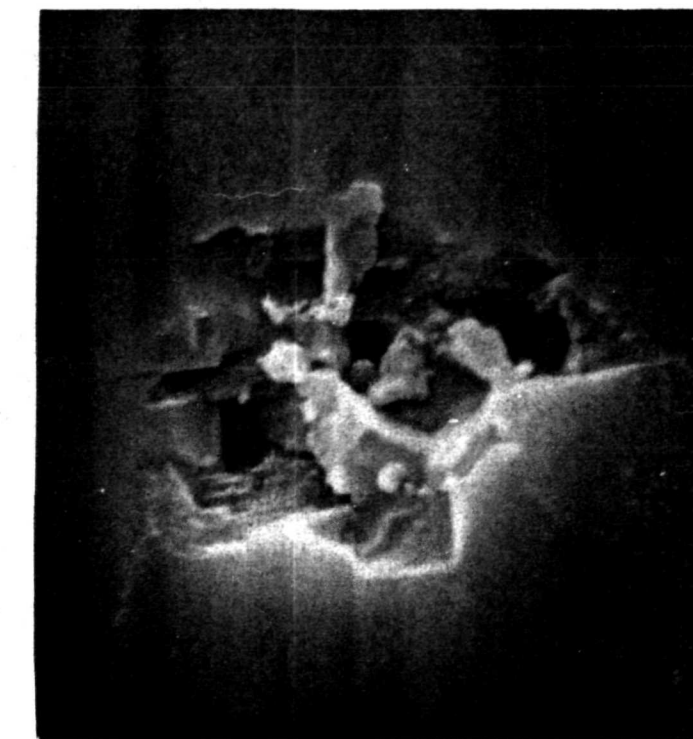
FIGURE 4-25. Photographs of Craters from 60° to Normal Oblique Impacts of Iron Particles on Oligoclase, 6.57 to 26.1 km/s: (a); crater S3-7-C, 6.57 km/s. (b); crater S3-7-B, 6.85 km/s. (c); crater S3-14-A, 9.08 km/s. (d); crater S3-14-B, 9.37 km/s. (e); crater S3-9-A, 9.42 km/s. (f); crater S4-2-A, 20.6 km/s. (g); crater S4-2-B, 23.7 km/s. (h); crater S4-2-C, 26.1 km/s. (a) has 5 micron indexes, (f) has one micron indexes, and all others have 2 micron indexes. All have a 20° tilt angle.



(a)



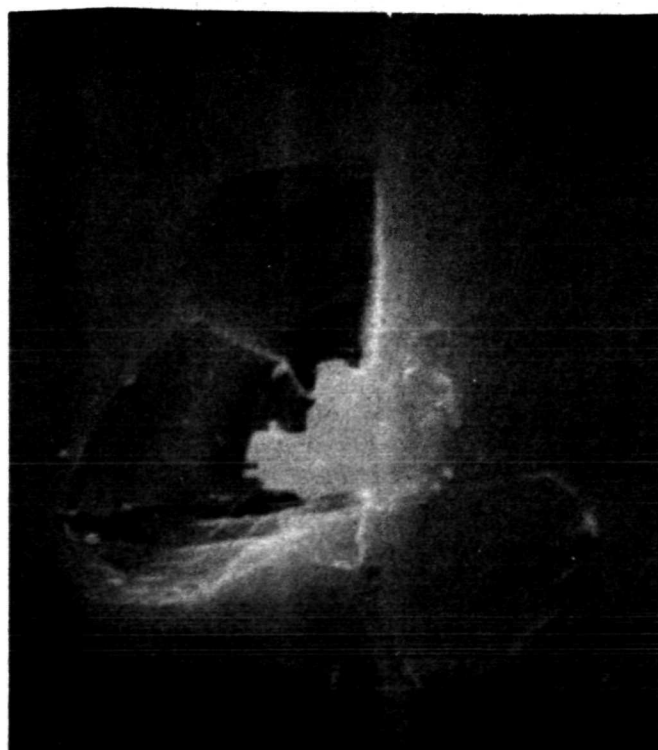
(b)



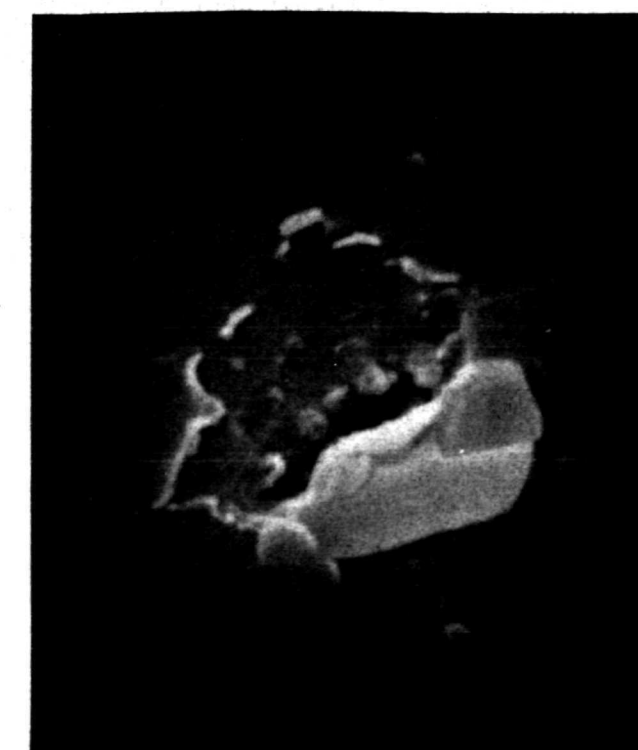
(c)



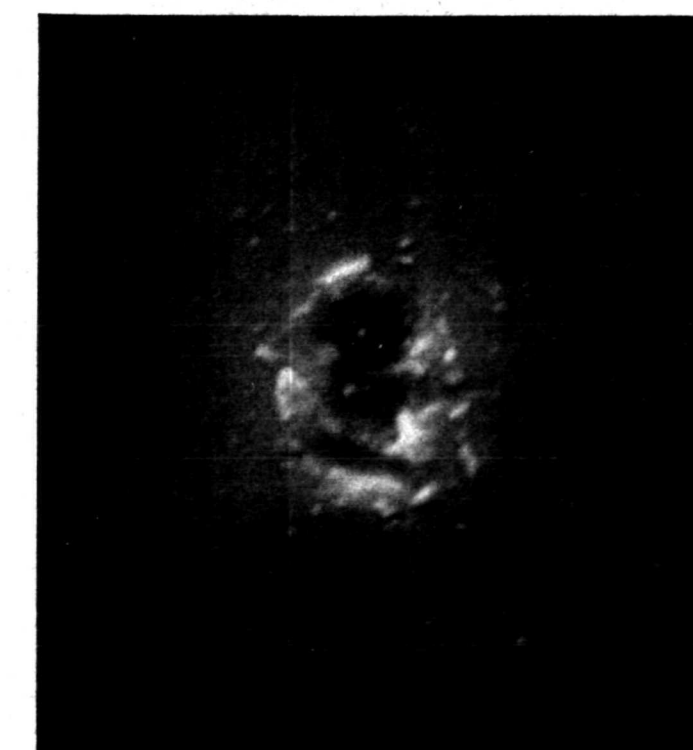
(d)



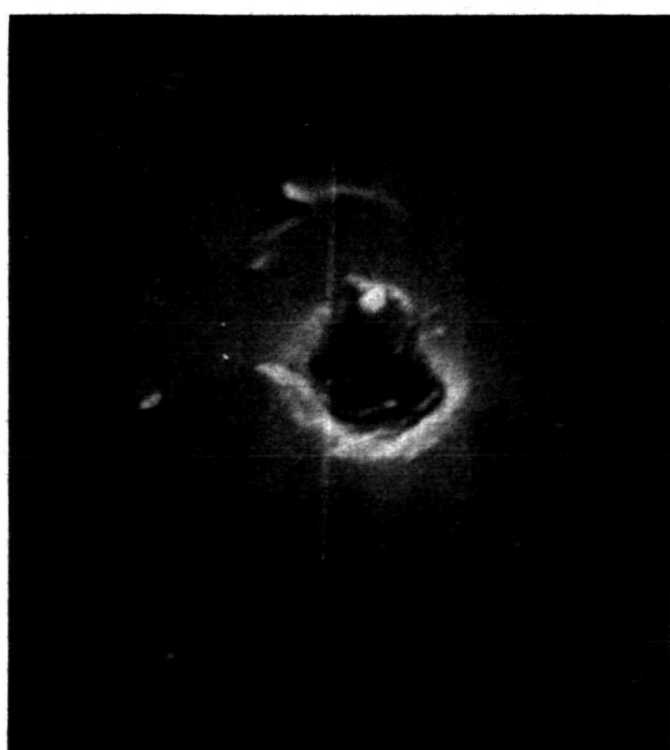
(e)



(f)

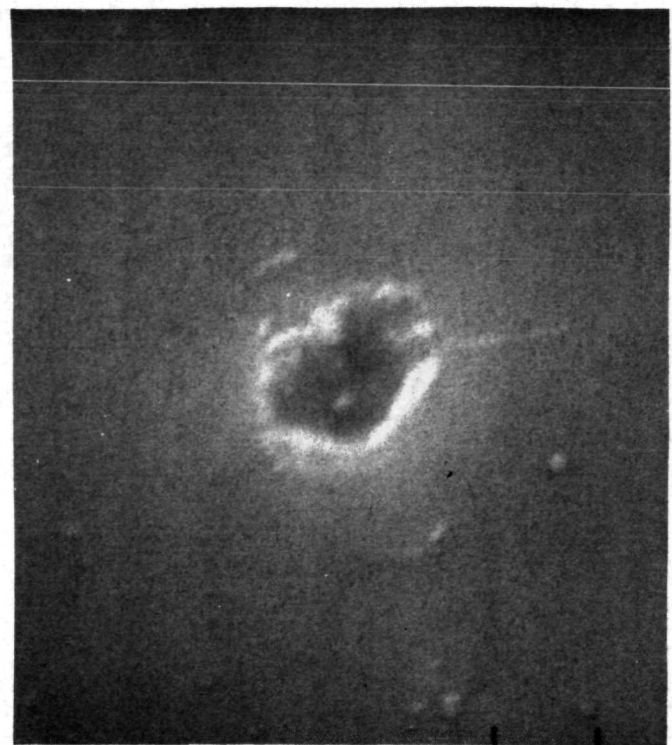


(g)



(h)

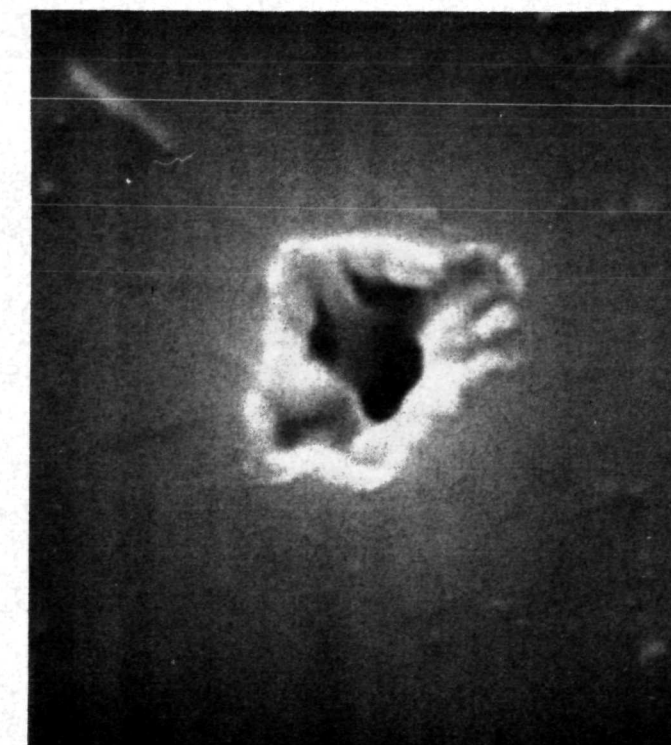
FIGURE 4-26. Photographs of Craters from Normal Impacts of Lanthanum Hexaboride Particles on Oligoclase, 1.46 to 5.12 km/s: (a); crater S2-2-A, 1.46 km/s. (b); crater S2-2-B, 1.73 km/s. (c); crater S2-1-A, 2.44 km/s. (d); crater S2-2-C, 2.67 km/s. (e); crater S2-1-B, 2.99 km/s. (f); crater S2-3-A, 4.49 km/s. (g); crater S2-3-B, 4.91 km/s. (h); crater S2-3-C, 5.12 km/s. (a), (b), (d), and (e) have 5 micron indexes, all others have 2 micron indexes. (c) has a 14° tilt angle, all others tilted at 20°.



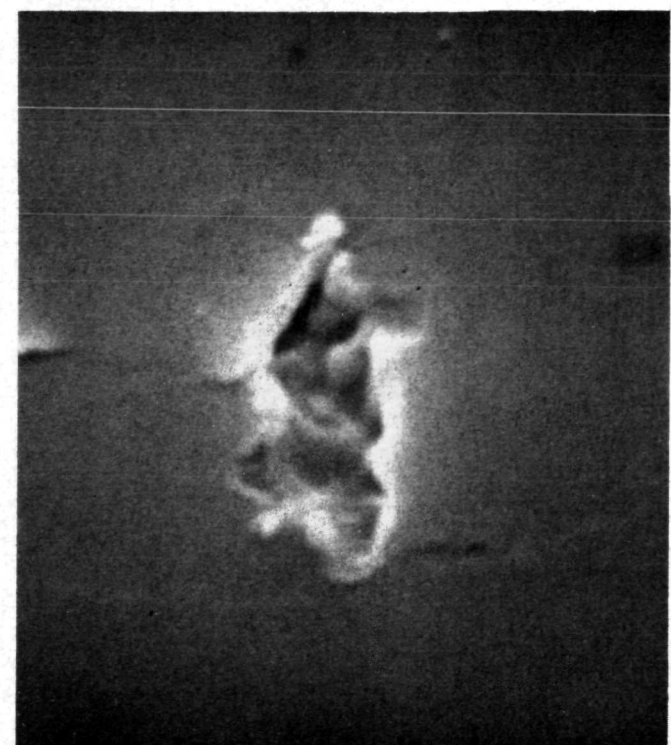
(a)



(b)



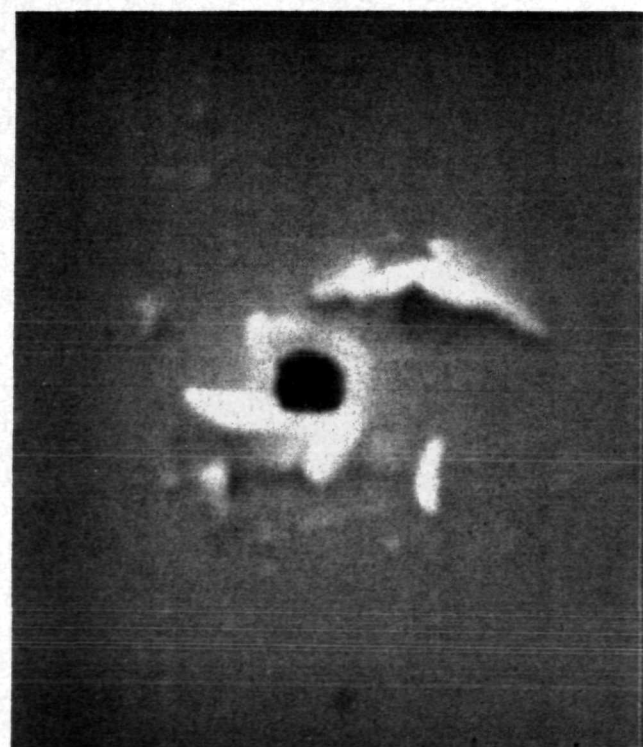
(c)



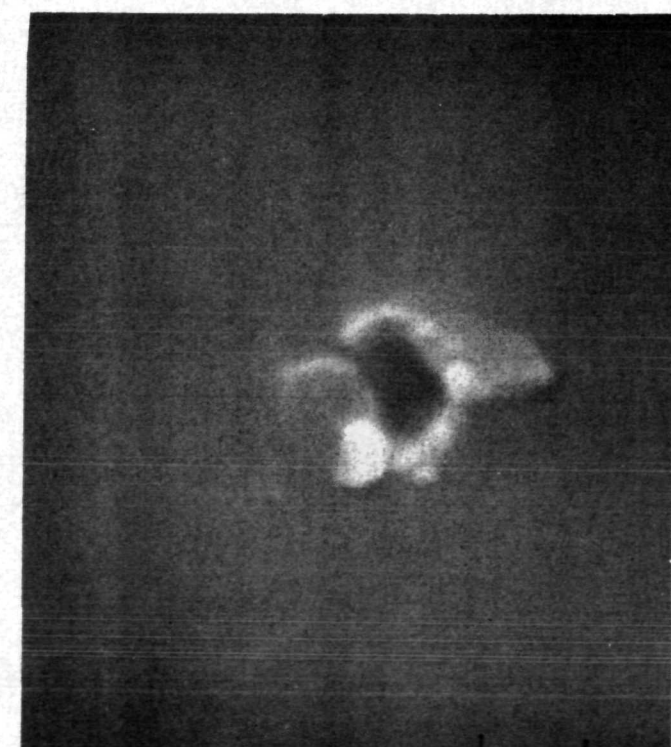
(d)



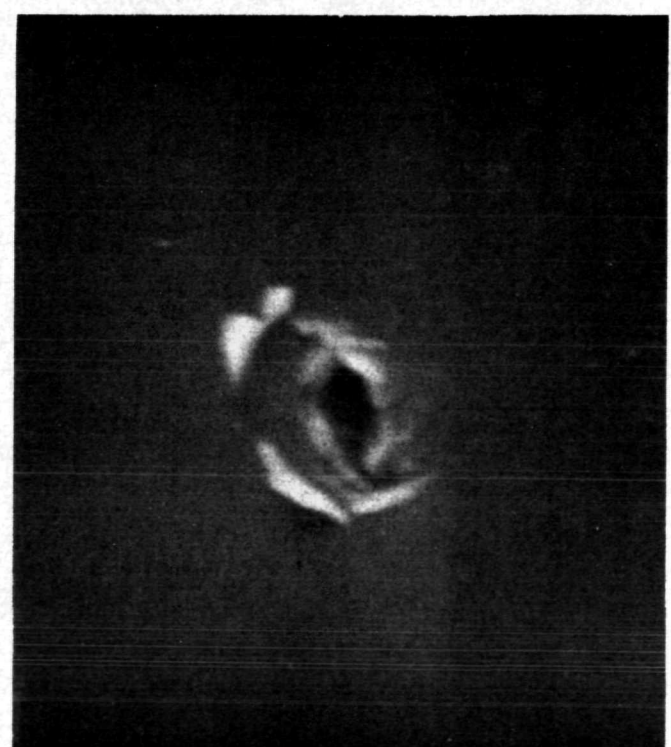
(e)



(f)



(g)



(h)

FIGURE 4-27. Photographs of Craters from Normal Impacts of Lanthanum Hexaboride Particles on Oligoclase, 6.21 to 22.9 km/s: (a); crater S2-4-B, 6.21 km/s. (b); crater S2-4-A, 6.82 km/s. (c); crater S2-6-D, 9.73 km/s. (d); crater S2-6-C, 10.7 km/s, (e); crater S2-7-B, 13.3 km/s. (f); crater S2-7-C, 14.5 km/s. (g); crater S2-8-D, 16.1 km/s. (h); crater S2-9-D, 22.9 km/s. (a), (b), and (h) have 2 micron indexes, all others have one micron indexes. (d) has a 14° tilt, all others are tilted at 20°.

Figure 4-27 shows craters obtained from 6.21 km/s in (a) to 22.9 km/s in (h). Very little spallation is seen on any of these impacts; however, a well defined lip structure appears at velocities higher than (b) which was at 6.82 km/s. Strong evidence of "jetting" from the interior of the crater pit are suggested in (c) and (e).

#### 4.2.2.2 Photographs of Oblique Impacts

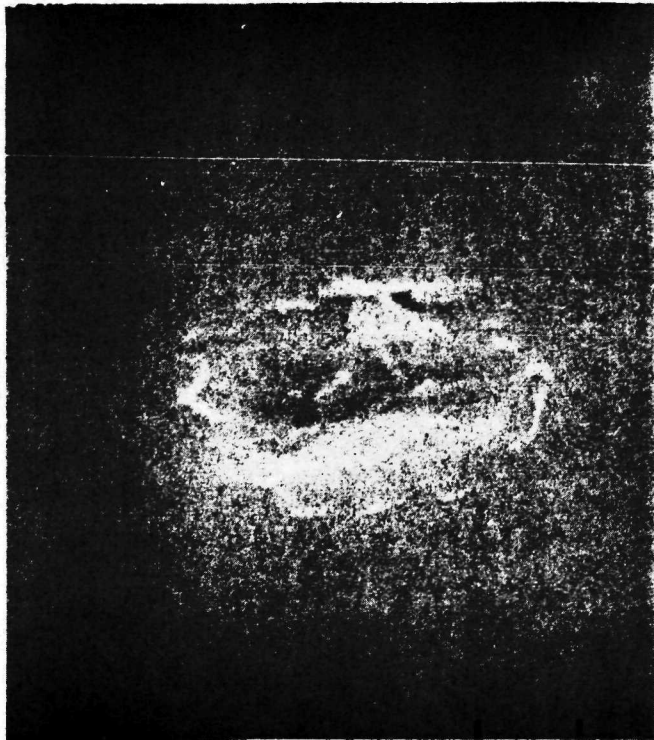
Figure 4-28 shows four examples of 30° to normal oblique impacts of lanthanum hexaboride particles on oligoclase. The impact velocities of (a) through (d) are, respectively, 2.43, 2.69, 4.25, and 5.31 km/s. The craters in (b), (c), and (d) are evidently oblique impacts, but none show the degree of spallation, crater lip, or droplet formation that was obtained with iron particle impacts.

Figure 4-29 contains photographs of 60° to normal oblique impacts of lanthanum hexaboride particles on oligoclase. The velocity range covered extends from 3.08 to 8.18 km/s. The craters in (a) and (b) at 3.08 and 3.36 km/s, respectively, show evidence that the particle bounced from the surface. There was almost no spallation for these impacts and no melt. The light petal-like rings around (c), (d), (e), and (f) are believed to be the remnants of the aluminum film which was evaporated onto the surface.

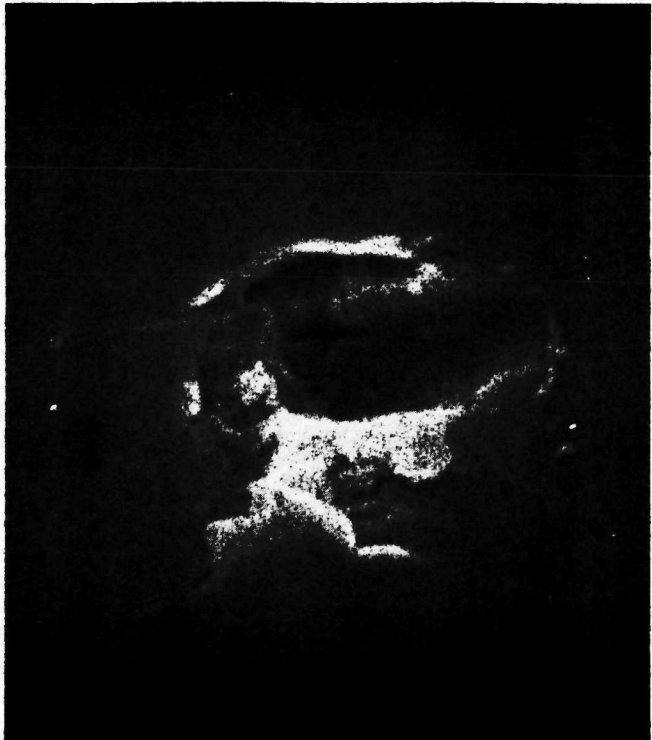
#### 4.2.3 Silicon Particle Impact Craters in Oligoclase

##### 4.2.3.1 Photographs of Normal Impact Craters at Different Crystal Orientations

Figure 4-30 and 4-31 contain the crater photographs for the data of Table 12. These impacts were made onto a surface which is parallel to the (010) plane of the crystal. The velocity range extends from 2.40 to 8.52 km/s in Figure 4-30 and from 9.68 to 22.4 km/s in Figure 4-31. The silicon particles used for these impacts have an irregular shape as did the LaB<sub>6</sub> particles of the previous section. Spallation was produced on



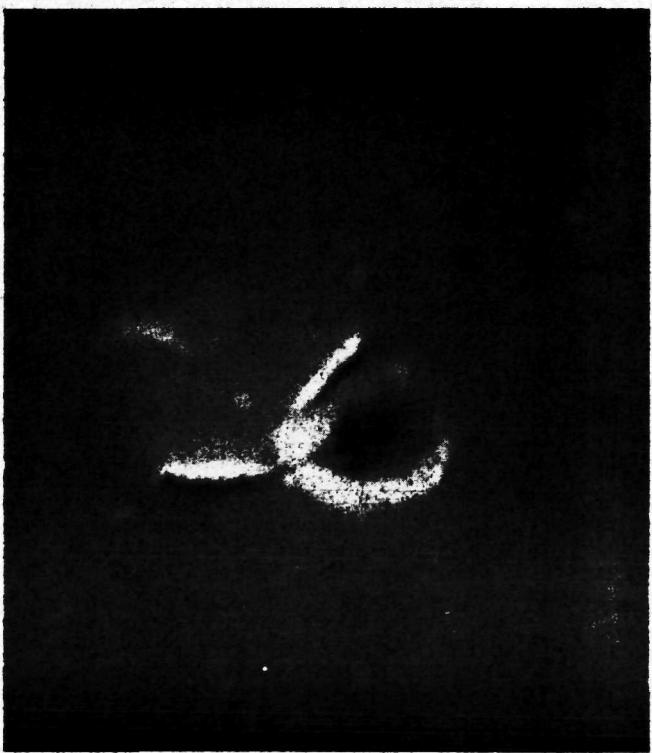
(a)



(b)



(c)

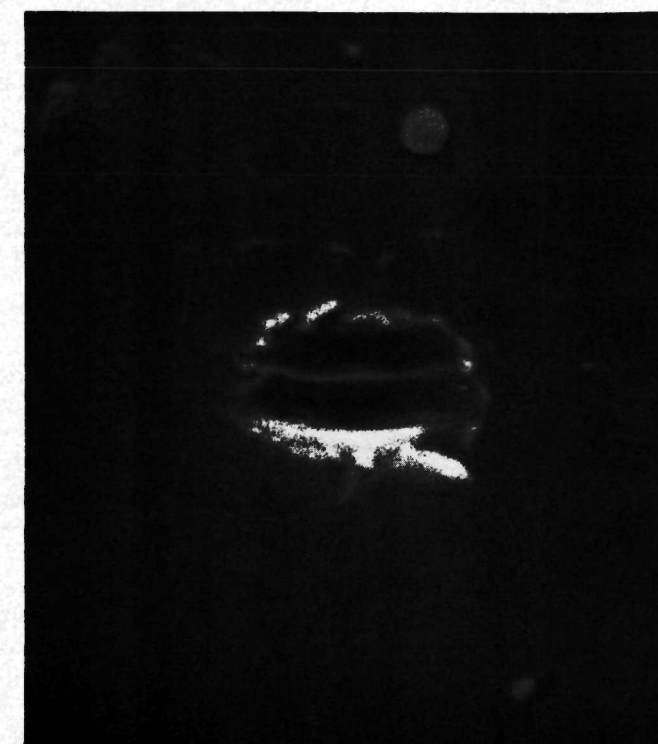


(d)

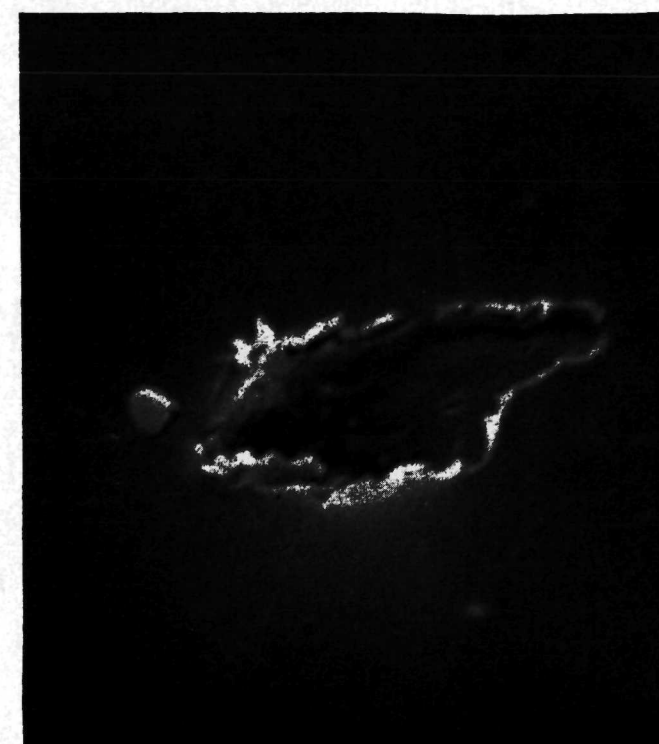
**FIGURE 4-28. Photographs of Craters from 30° to Normal Oblique Impacts of Lanthanum Hexaboride Particles on Oligoclase, 2.43 to 5.31 km/s: (a); crater S2-1-C, 2.43 km/s. (b); crater S2-6-A, 2.69 km/s. (c); crater S2-8-A, 4.25 km/s. (d); crater S2-8-E, 5.31 km/s. All have two micron index mark separation. (b) has a 14° tilt angle, all others have 20°.**



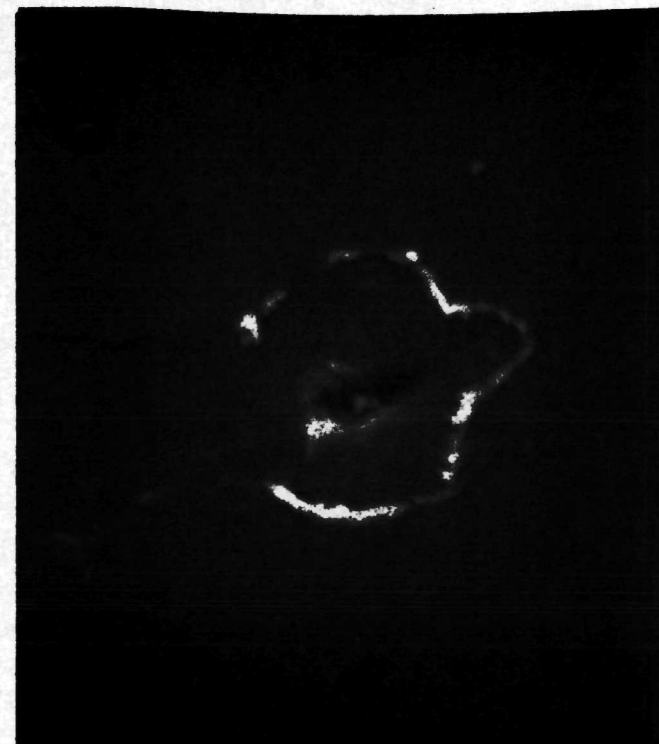
(a)



(b)



(c)



(d)

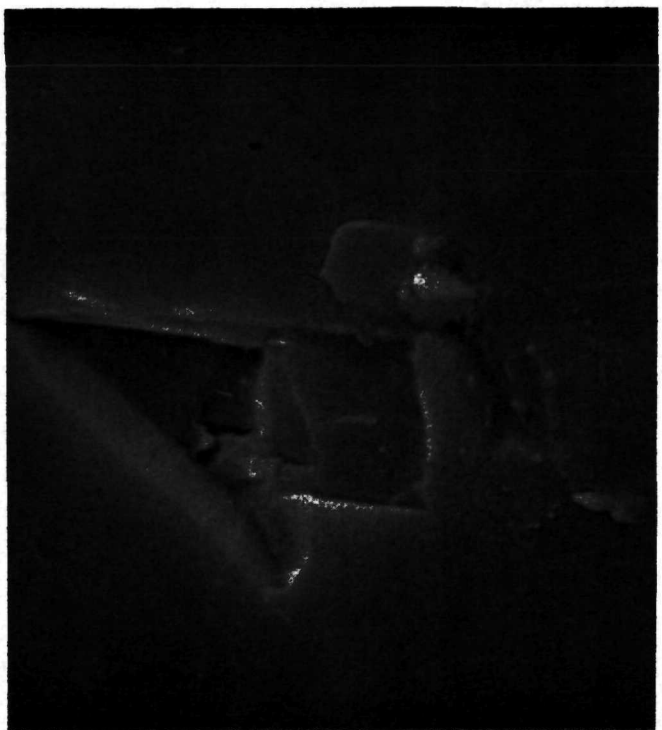


(e)

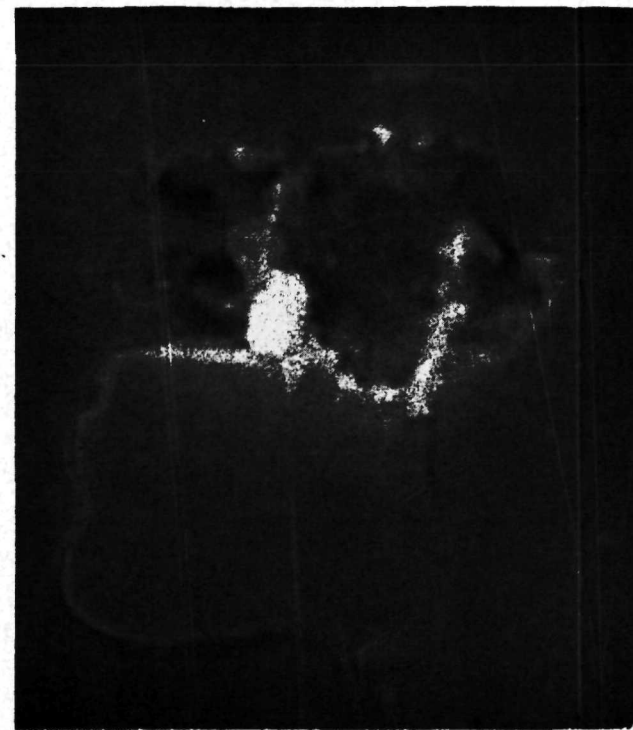


(f)

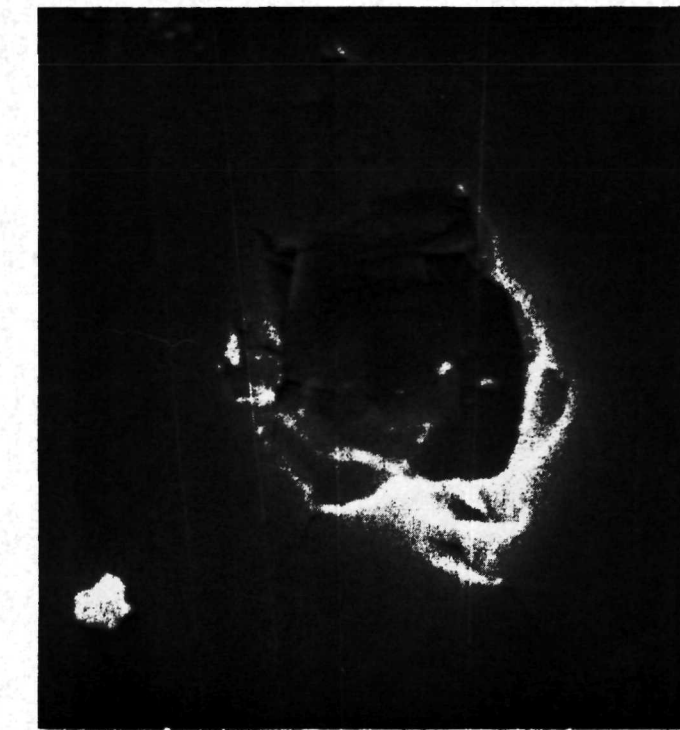
FIGURE 4-29. Photographs of Craters from 60° to Normal Oblique Impacts of Lanthanum Hexaboride Particles on Oligoclase, 3.08 to 8.18 km/s: (a); crater S2-2-E, 3.08 km/s. (b); crater S2-7-A, 3.36 km/s. (c); crater S2-9-A, 5.30 km/s. (d); crater S2-9-B, 5.86 km/s. (e); crater S2-4-D, 5.86 km/s. (f); crater S2-5-A, 8.18 km/s. All have 2 micron indexes and 20° tilt angle.



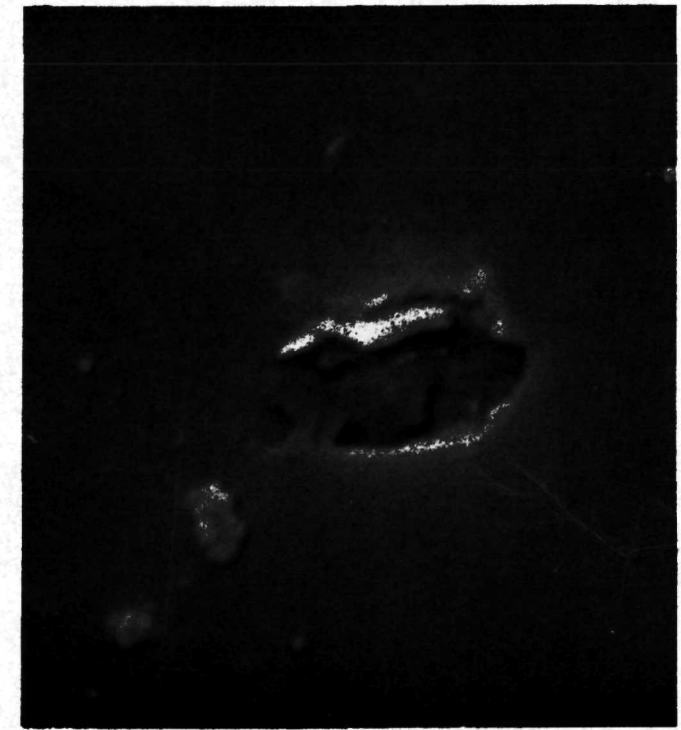
(a)



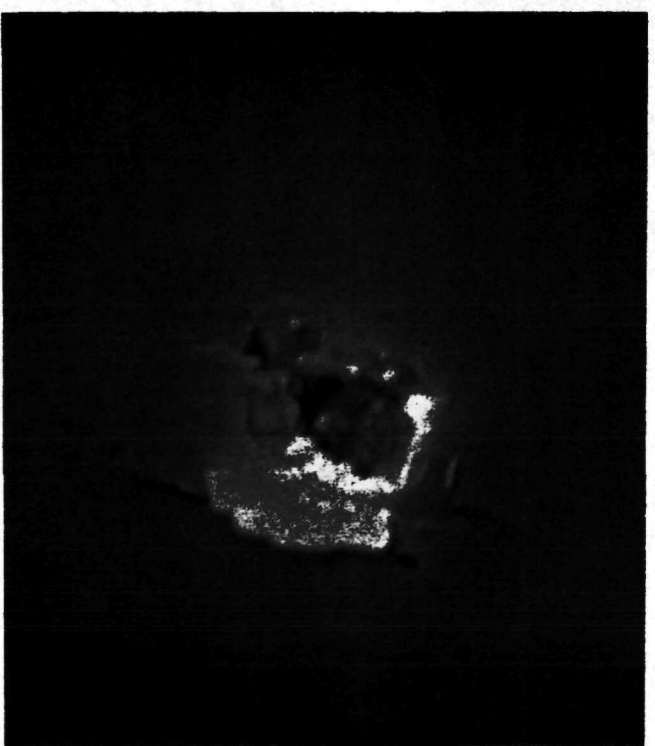
(b)



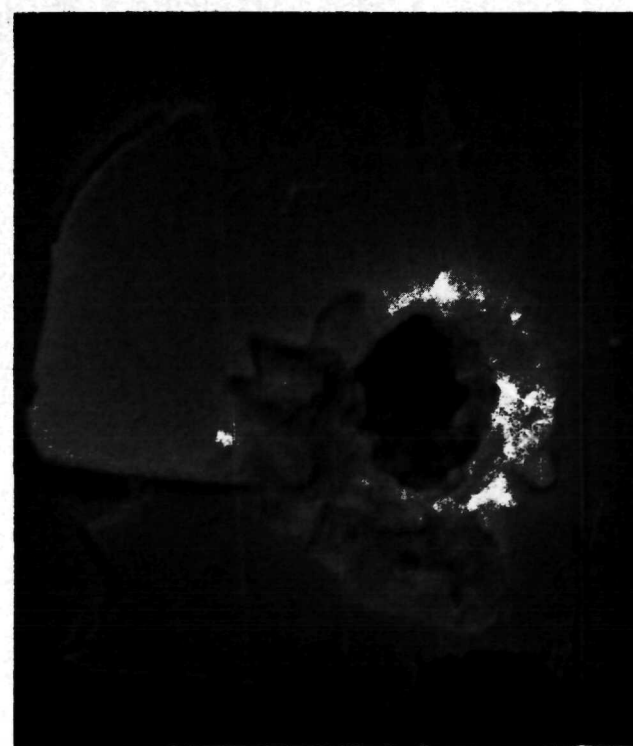
(c)



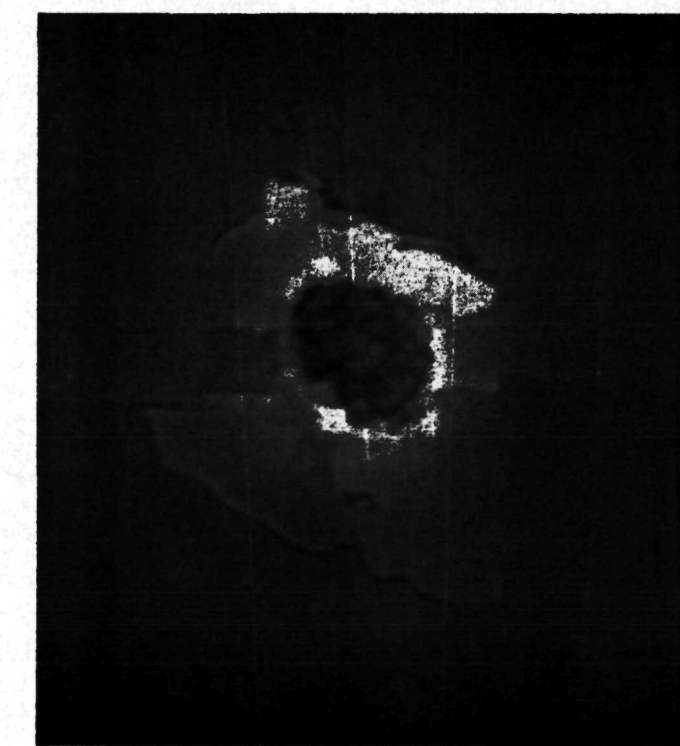
(d)



(e)

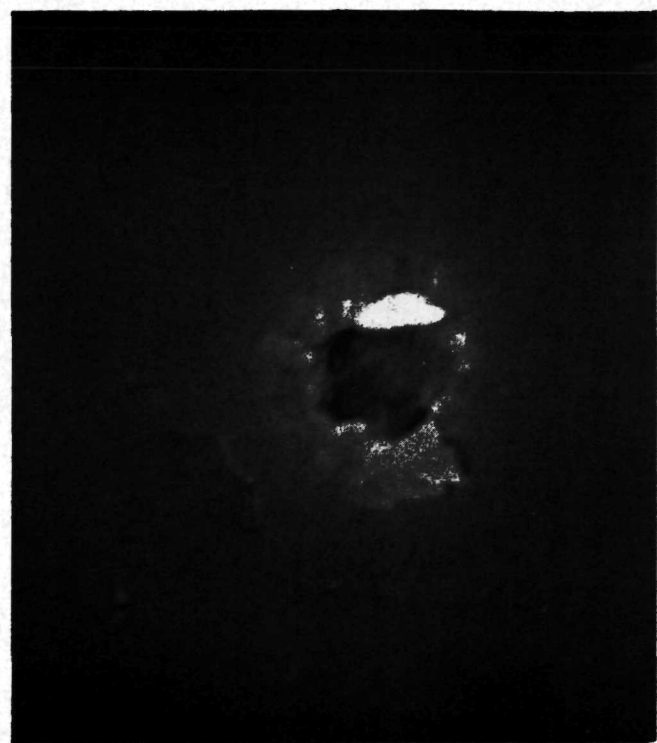


(f)

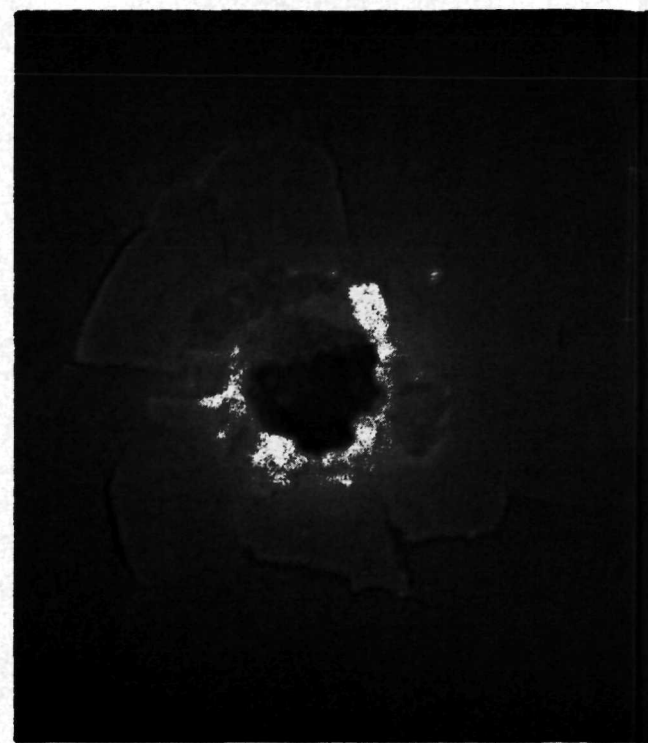


(g)

FIGURE 4-30. Photographs of Craters from Normal Impacts of Silicon Particles on Oligoclase, Surface Parallel to (010), 2.40 to 8.52 km/s: (a); crater S6-3-A, 2.40 km/s. (b); crater S6-2-A, 4.24 km/s. (c); crater S6-1-E, 4.90 km/s. (d); crater S6-1-C, 5.16 km/s. (e); crater S6-1-B, 5.93 km/s. (f); crater S6-1-A, 8.25 km/s. (g); crater S6-4-D, 8.52 km/s. (a), (c), and (e) have 5 micron indexes, all others have 2 micron indexes. All have 3.5° tilt angle.



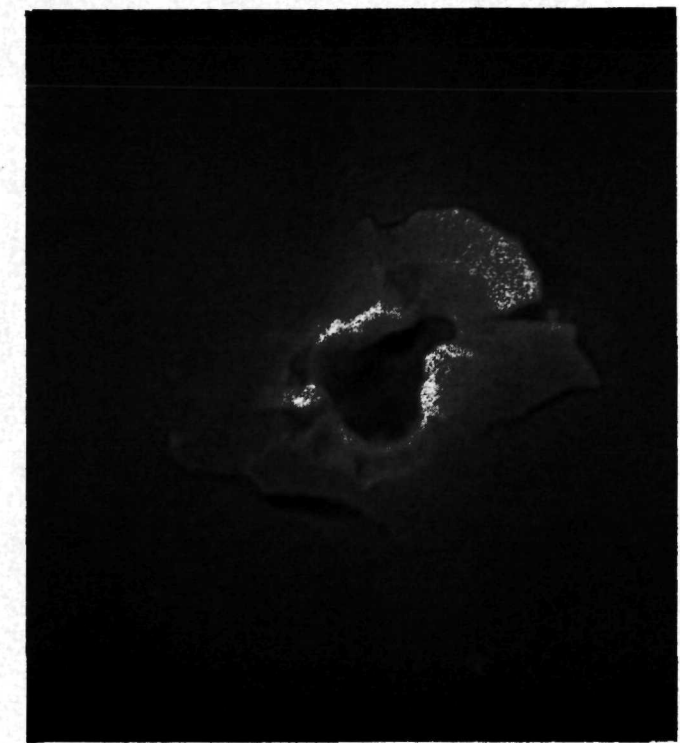
(a)



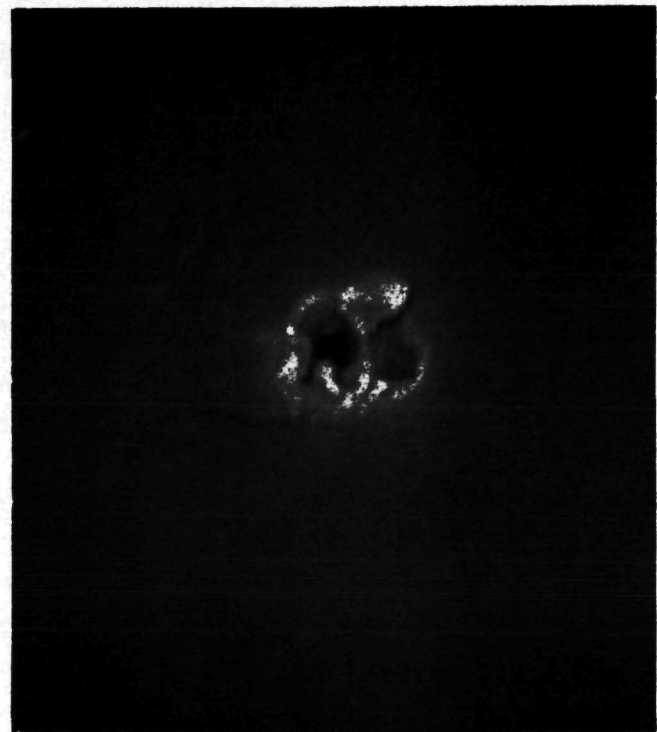
(b)



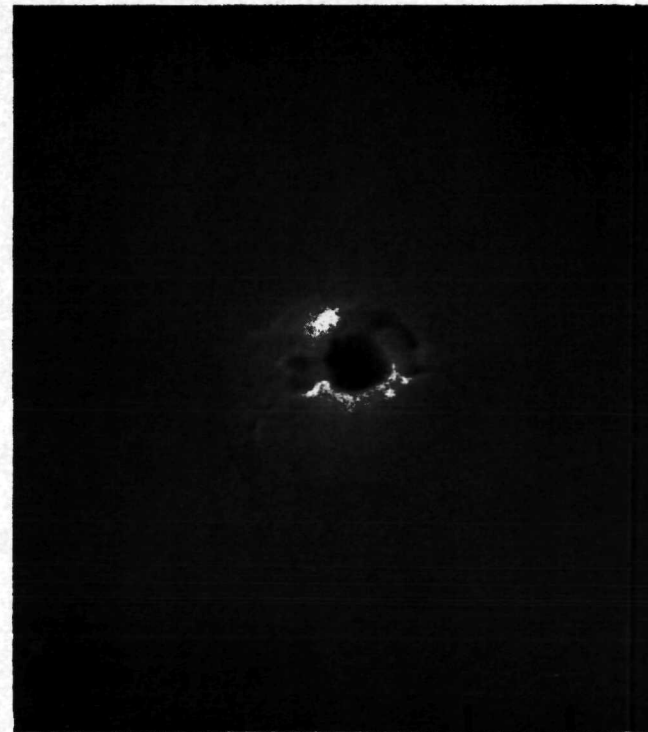
(c)



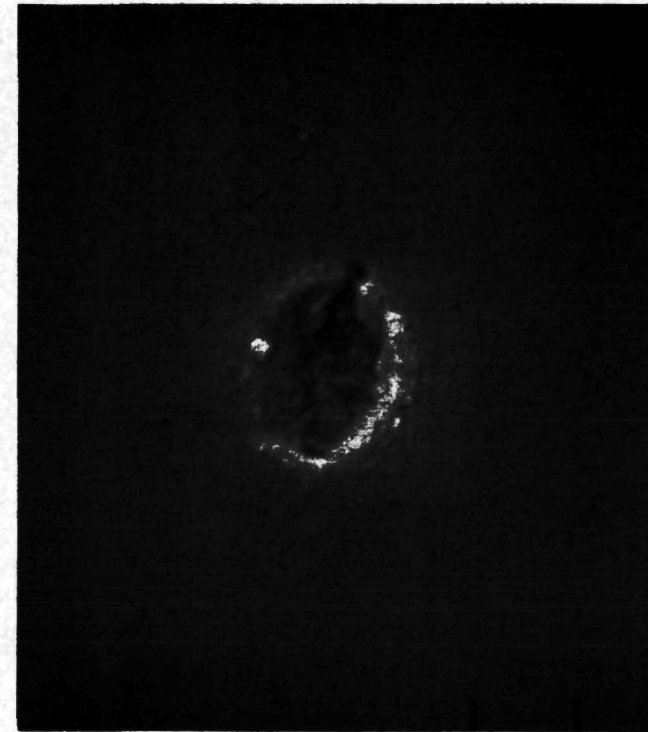
(d)



(e)



(f)



(g)

FIGURE 4-31. Photographs of Craters from Normal Impacts of Silicon Particles on Oligoclase, Surface Parallel to (010), 9.68 to 22.4 km/s: (a); crater S6-4-A, 9.68 km/s. (b); crater S6-4-B, 12.1 km/s. (c); crater S6-4-C, 13.1 km/s. (d); crater S6-5-A, 14.1 km/s. (e); crater S6-5-B, 16.8 km/s. (f); crater S6-5-C, 20.6 km/s. (g); crater S6-10-A, 22.4 km/s. All have 2 micron indexes. (a), (b), and (c) have 3.5° tilt angle, all others have 20°.

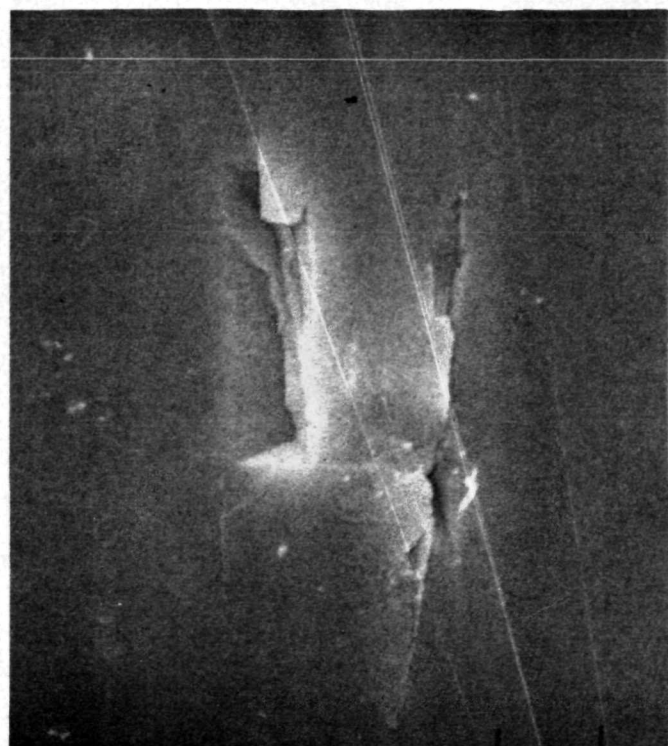
all impacts with the possible exceptions of Figures 4-30d and 4-31g. The development of the central pit lip structure cannot be determined very well since only remnants can be found. Most of the lip is spalled away in all cases where spallation exists. Droplet formation in the central pit may be seen in Figure 4-30b?, e, f, g and 4-31a, b.

Figures 4-32, and 4-33 contain photographs of the craters which produced the data of Table 14. These impacts occurred on a target surface which is parallel to the line of intersection of (010) and (001) and at 45° to both (010) and (001). The velocity range extends from 2.12 to 5.25 in Figure 4-32 and from 5.31 to 12.7 km/s in Figure 4-33. One immediately notices that more spallation is produced at this target surface orientation. The second point of note is that more droplets are seen within the crater pits. Figure 4-32a, b, c do not show melt or droplets; however, all remaining craters in both figures show a large number of droplets within the crater interior except for Figure 4-33e, and g. In (e) the central pit has been covered by a small plate and (g) appears to have a smooth glass lined interior.

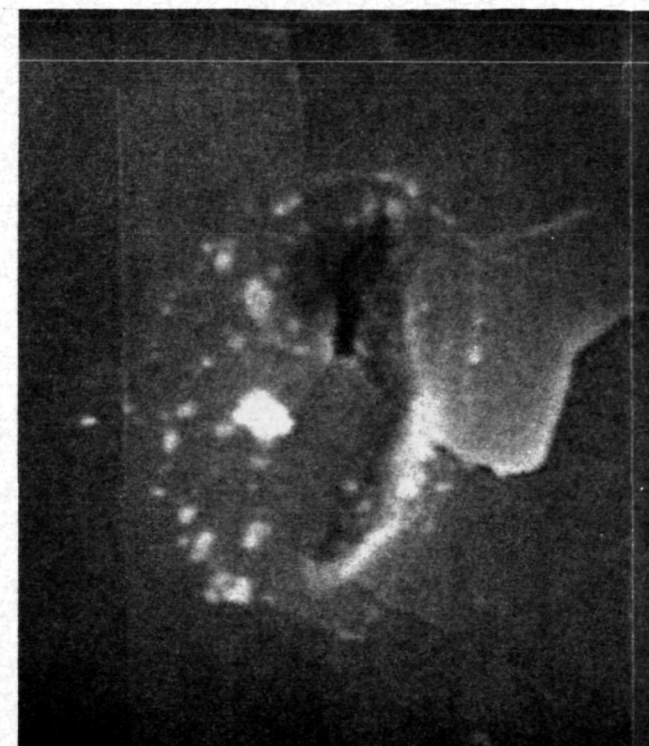
The craters corresponding to the data of Table 15 are shown in Figures 4-34 and 4-35. The impact surface for the set of craters is parallel to the prominent cleavage plane (001). The velocity range covered in Figure 4-34 extends from 2.82 to 10.6 km/s while that of Figure 4-35 extends from 10.6 to 12.4 km/s. The degree of spallation is less for this orientation than for the 45° cut used in the previous set. Portions of the central pit lip was spalled away in most cases above 5.60 km/s (Figure 4-34f).

#### 4.2.3.2 Oblique Impacts

Figures 4-36 and 4-37 contain the crater photographs for the data of Table 16. These impacts occurred at 30° to the target surface normal. The velocity range extends from 2.31 to 8.18 km/s in Figure 4-36 and from 10.5 to 20.6 km/s in Figure 4-37. Note that in Figure 4-36a



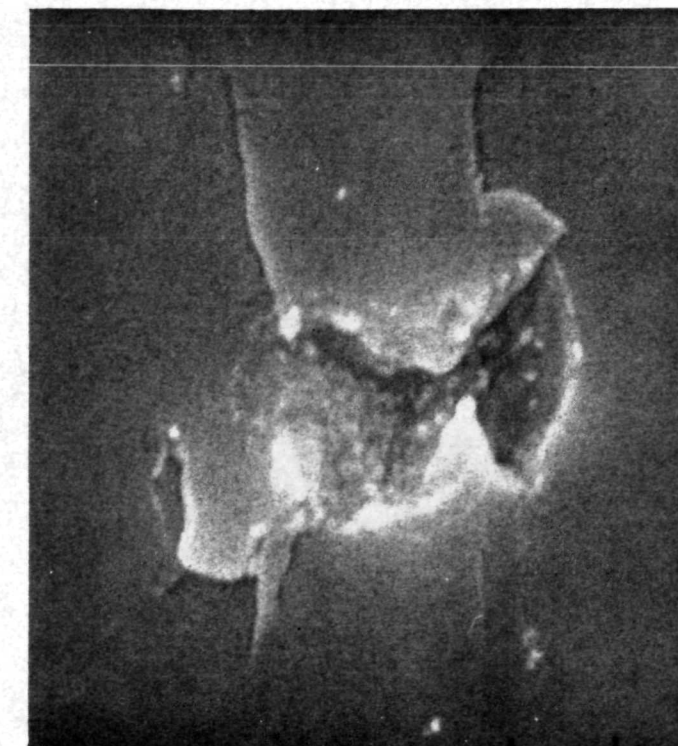
(a)



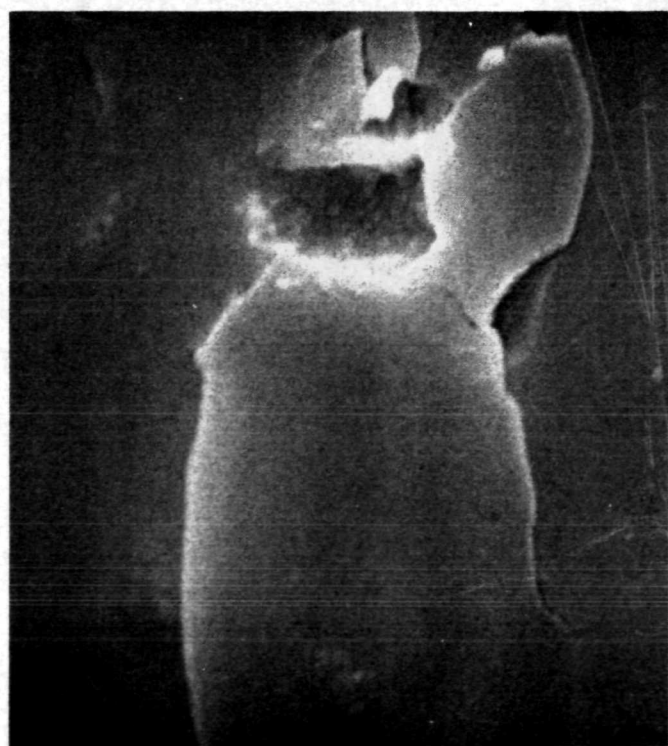
(b)



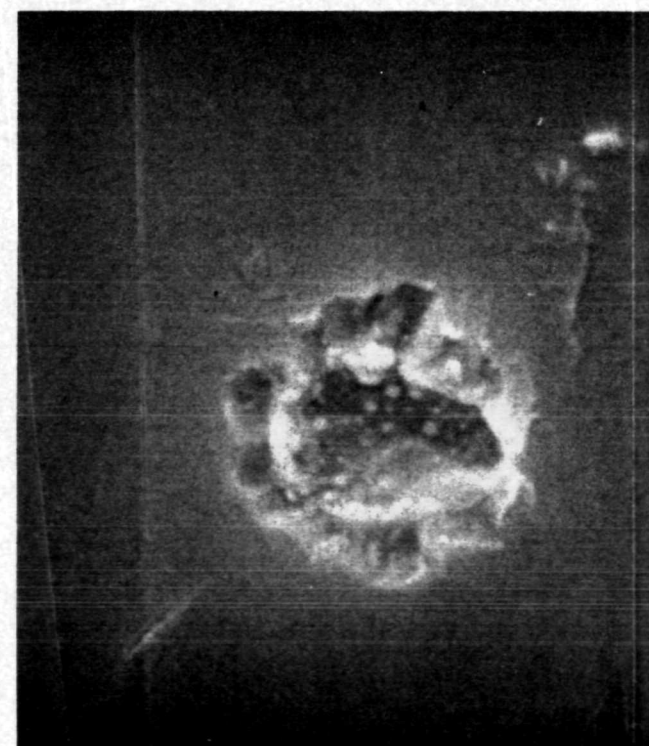
(c)



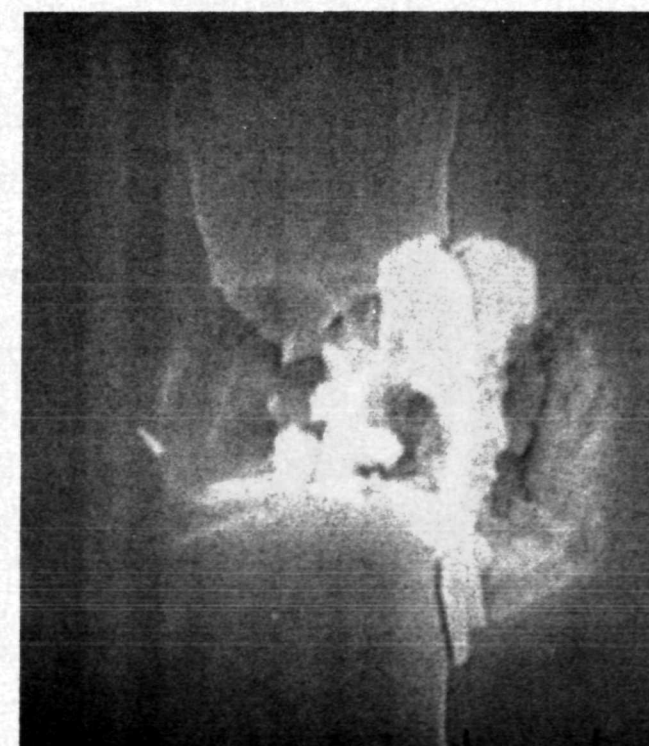
(d)



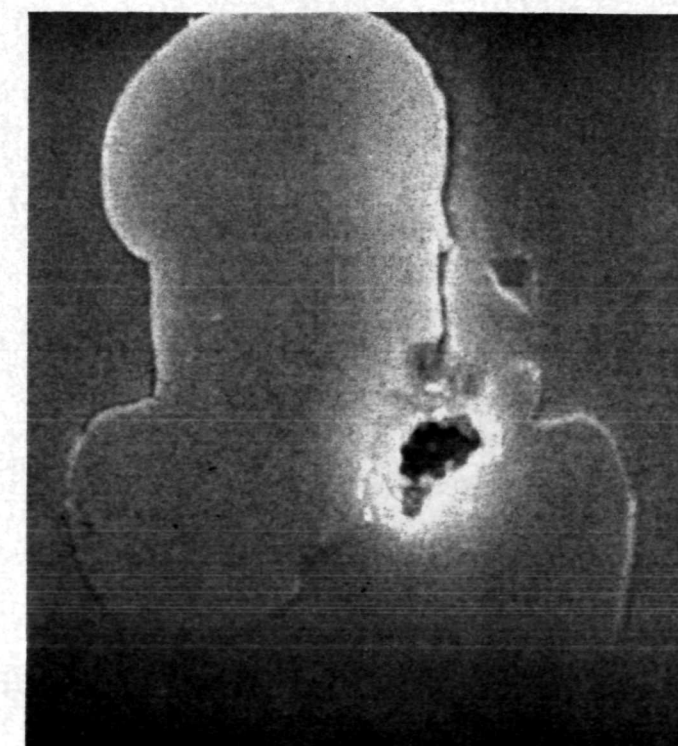
(e)



(f)

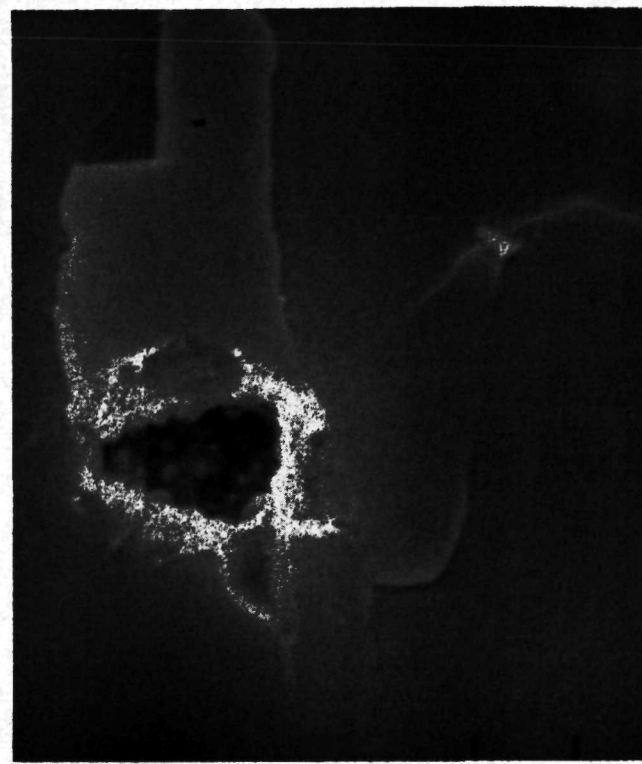


(g)

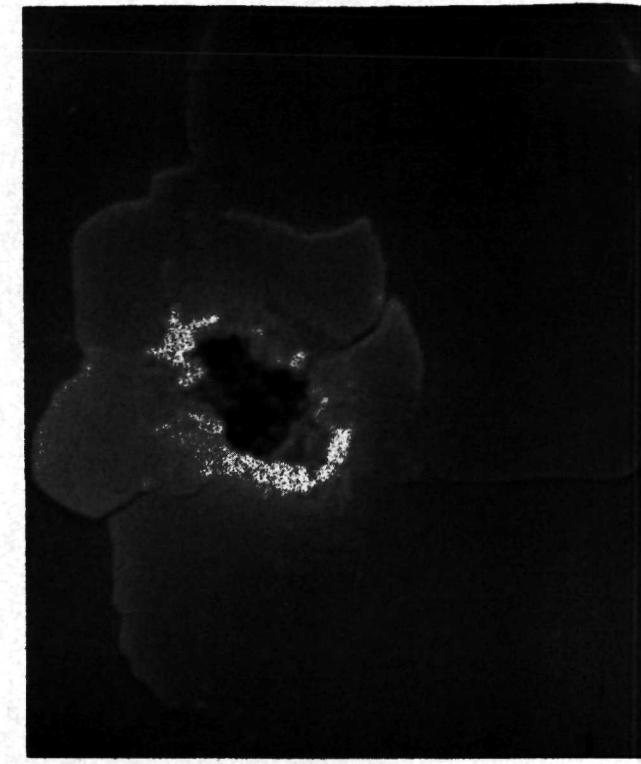


(h)

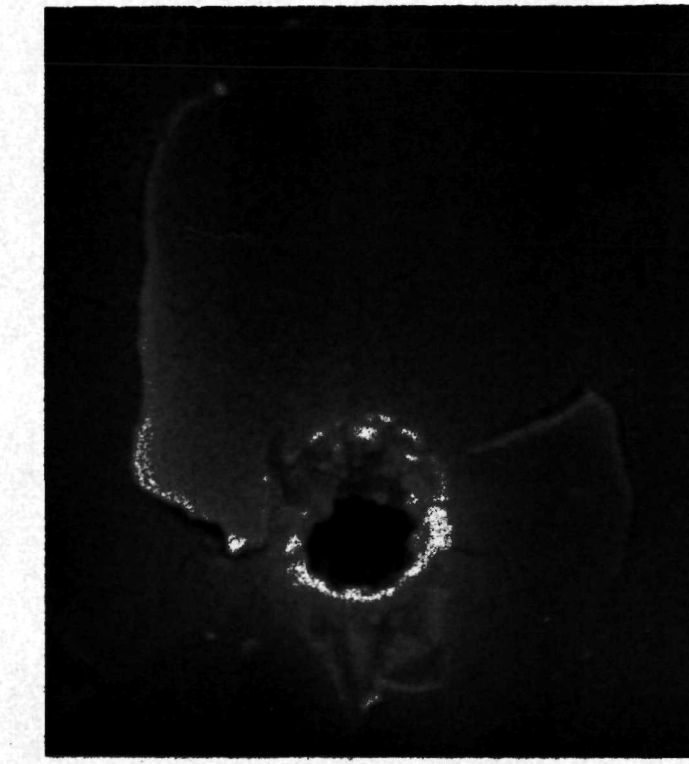
FIGURE 4-32. Photographs of Craters from Normal Impacts of Silicon Particles on Oligoclase, Surface at 45° to both (010) and (001), 2.12 to 5.25 km/s: (a); crater S9-4-C, 2.12 km/s. (b); crater S9-4-A, 2.63 km/s. (c); crater S9-4-D, 2.81 km/s. (d); crater S9-4-E, 3.09 km/s. (e); crater S9-3-B, 3.32 km/s. (f); crater S9-3-C, 4.23 km/s. (g); crater S9-3-A, 5.03 km/s. (h); crater S9-3-D, 5.25 km/s. (b), (d), and (f) have 2 micron indexes, all others have 5 micron indexes. All have 10° tilt angle.



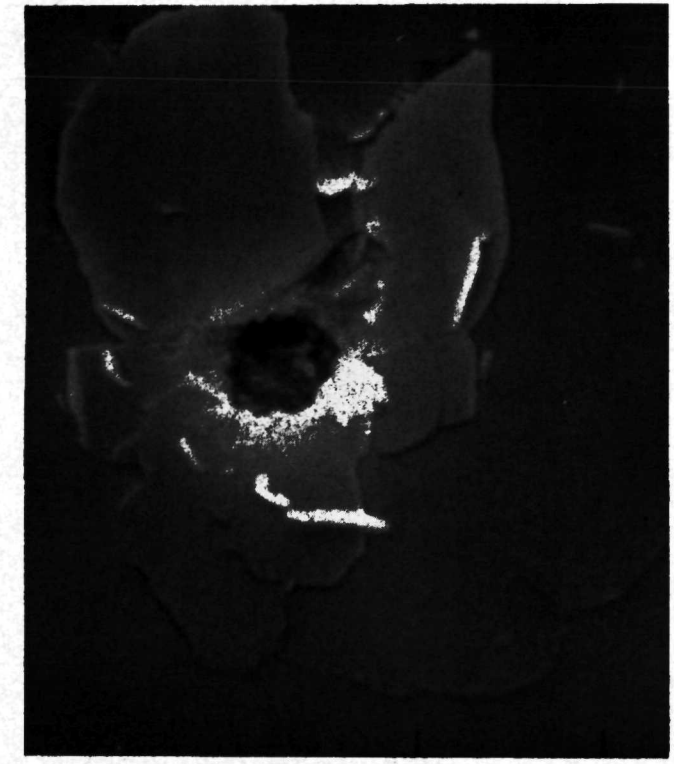
(a)



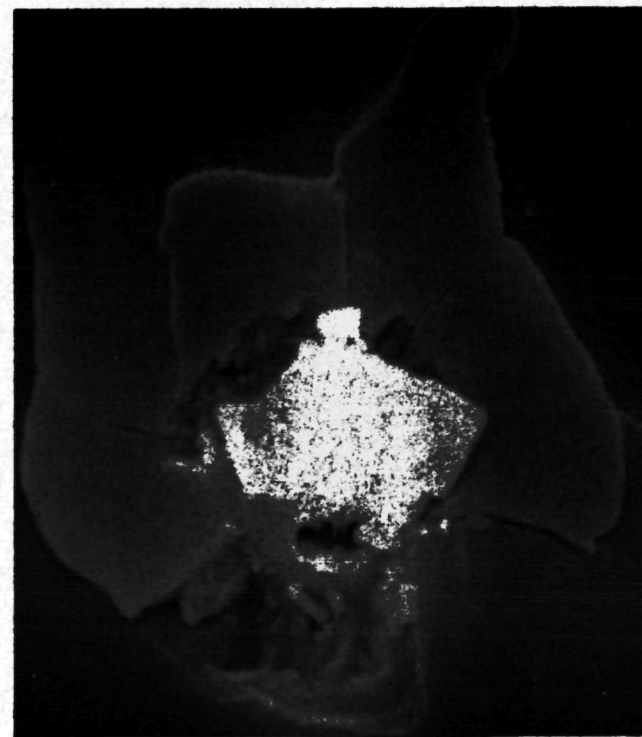
(b)



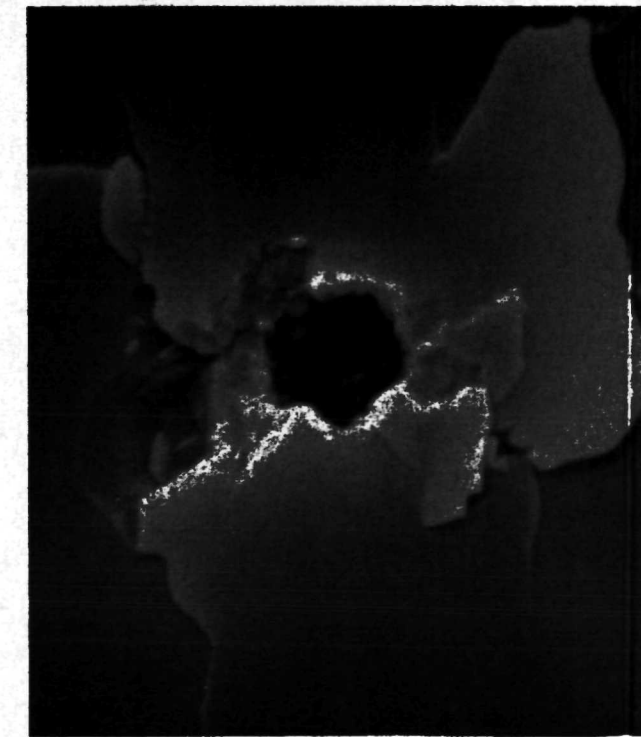
(c)



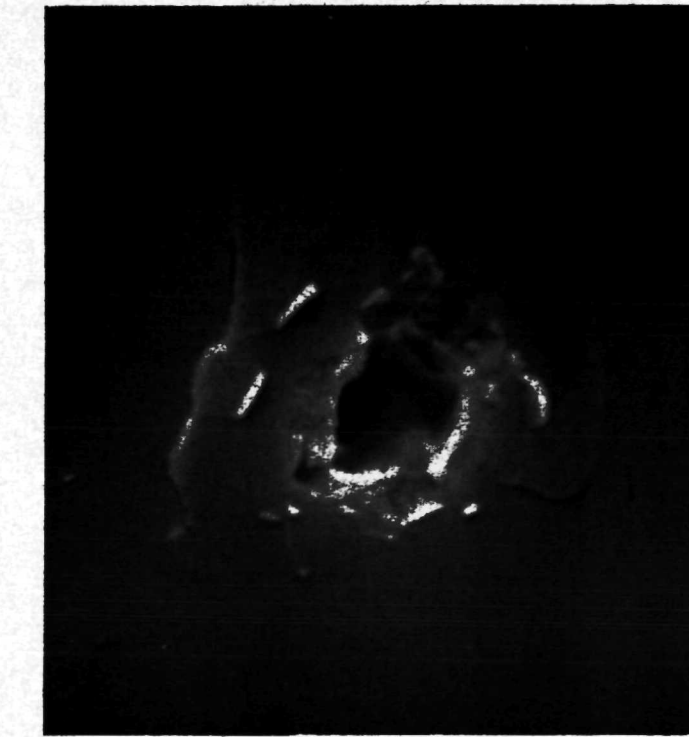
(d)



(e)

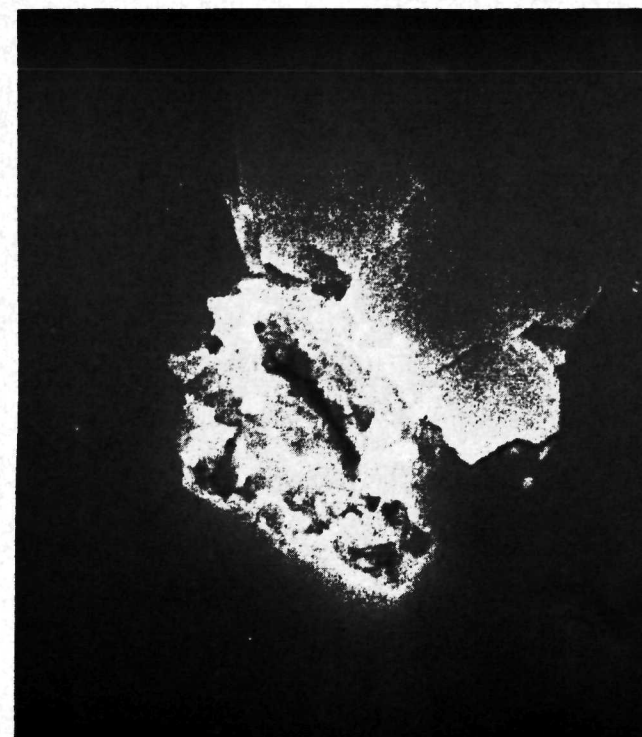


(f)

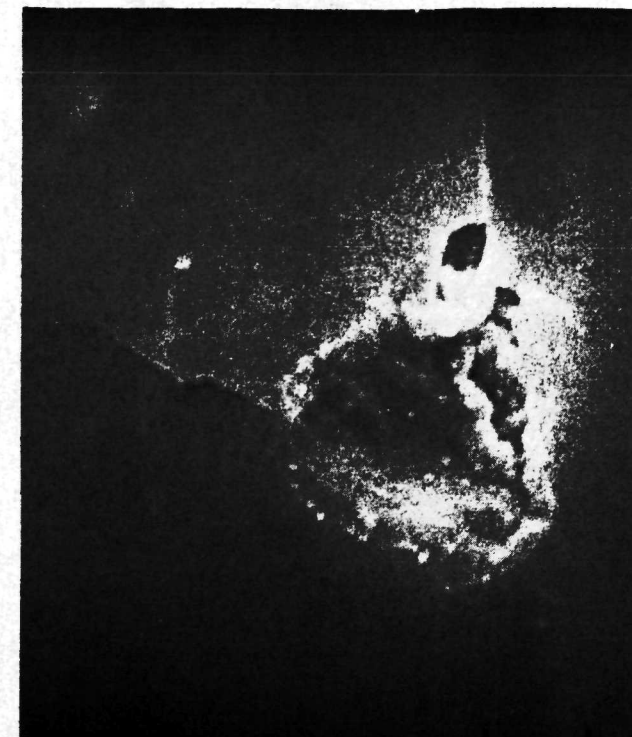


(g)

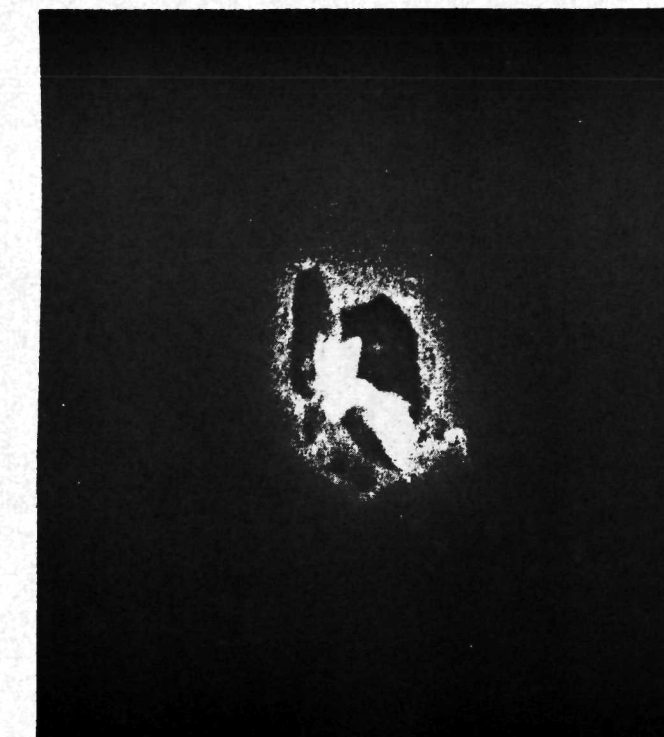
FIGURE 4-33. Photographs of Craters from Normal Impacts of Silicon Particles on Oligoclase, Surface at 45° to both (010) and (001), 5.31 to 12.7 km/s: (a); crater S9-2-A, 5.31 km/s. (b); crater S9-2-B, 6.10 km/s. (c); crater S9-2-C, 6.90 km/s. (d); crater S9-1-A, 7.72 km/s. (e); crater S9-1-C, 7.96 km/s. (f); crater S9-1-B, 9.29 km/s. (g); crater S9-1-D, 12.7 km/s. (d) and (e) have 5 micron indexes, all others have 2 micron indexes. All have a 10° tilt angle.



(a)



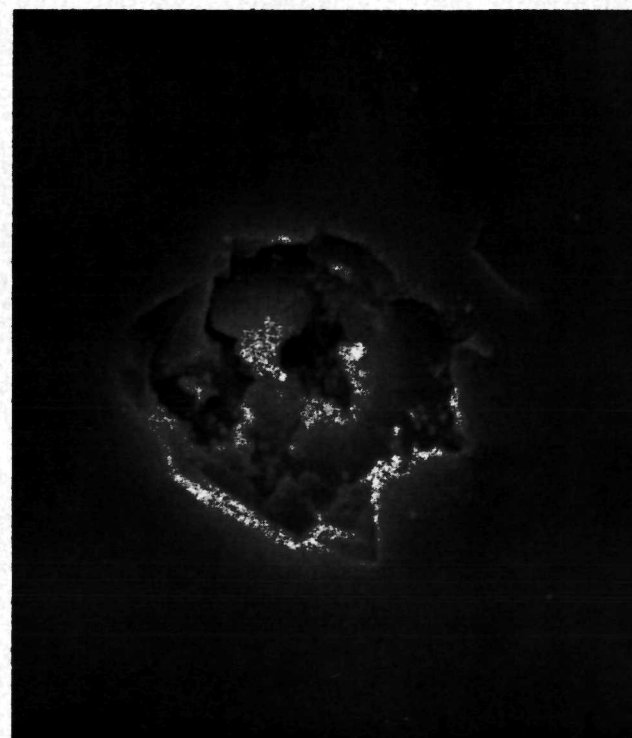
(b)



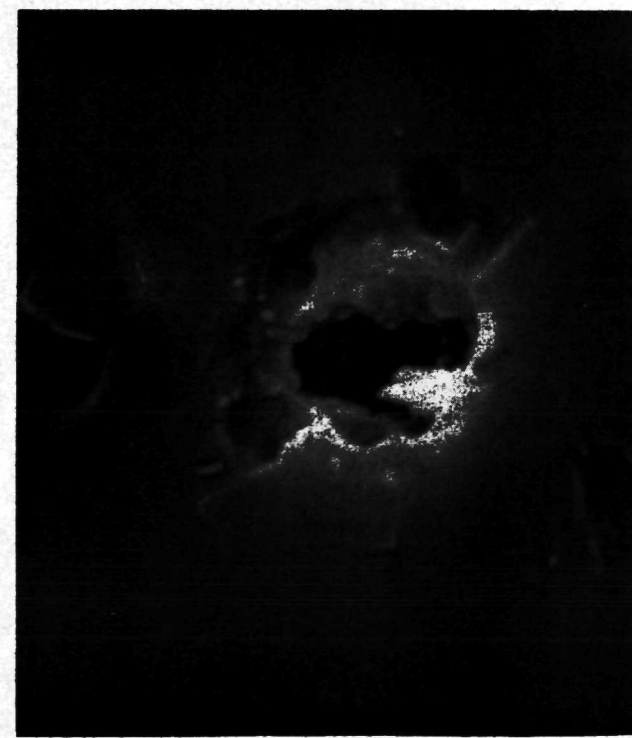
(c)



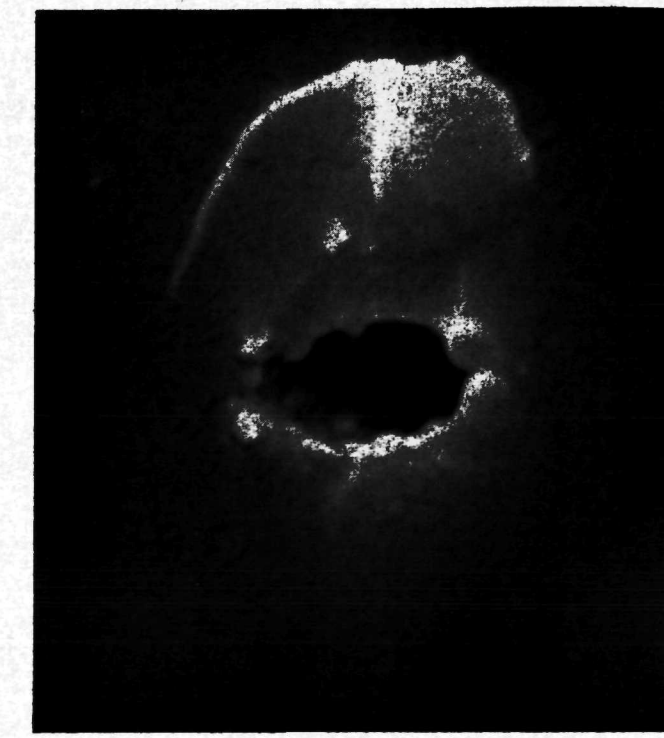
(d)



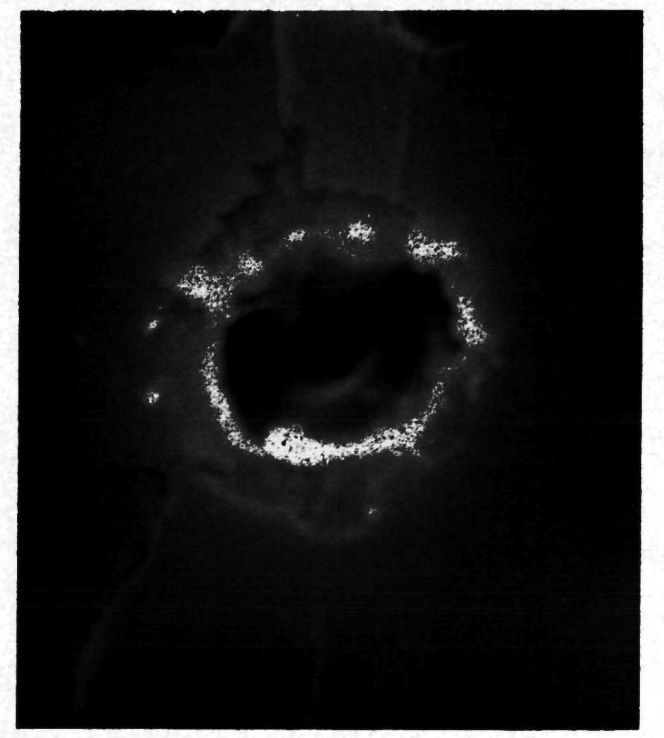
(e)



(f)

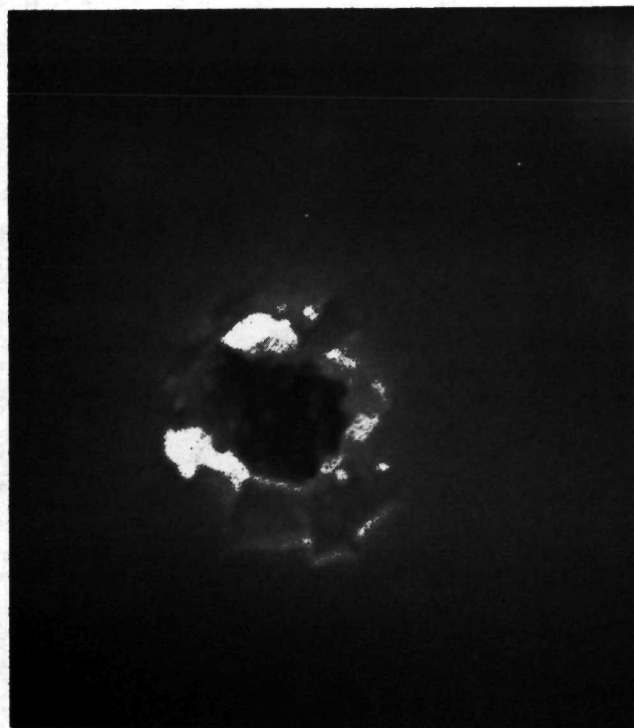


(g)

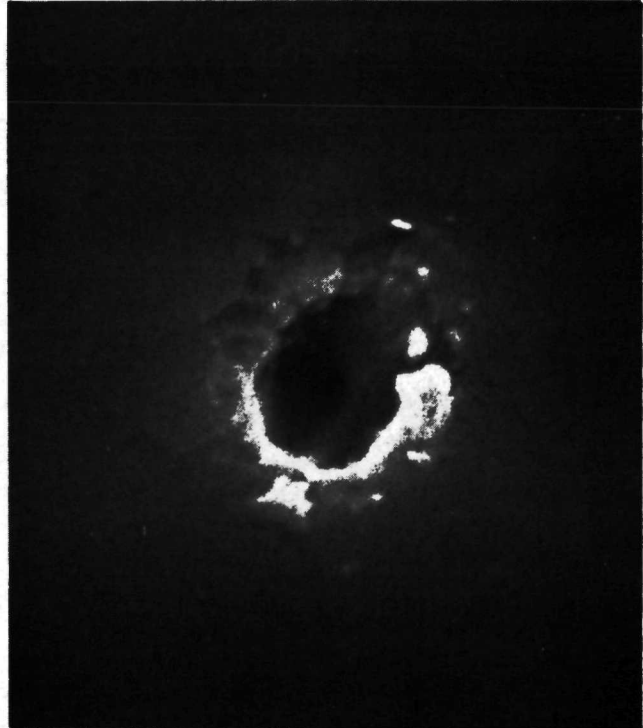


(h)

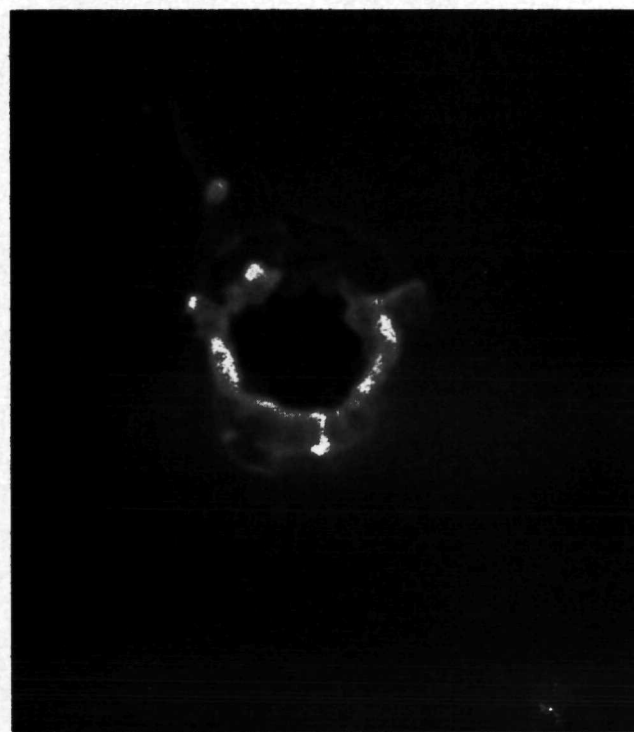
FIGURE 4-34. Photographs of Craters from Normal Impacts of Silicon Particles on Oligoclase, Surface Parallel to (001), 2.82 to 10.6 km/s: (a); crater S10-3-B, 2.82 km/s. (b); crater S10-3-A, 3.57 km/s. (c); crater S10-3-C, 3.58 km/s. (d); crater S10-2-B, 4.96 km/s. (e); crater S10-2-A, 5.03 km/s. (f); crater S10-2-D, 5.60 km/s. (g); crater S10-1-D, 7.47 km/s. (h); crater S10-1-E, 10.6 km/s. All have 2 micron indexes and 10° tilt angle.



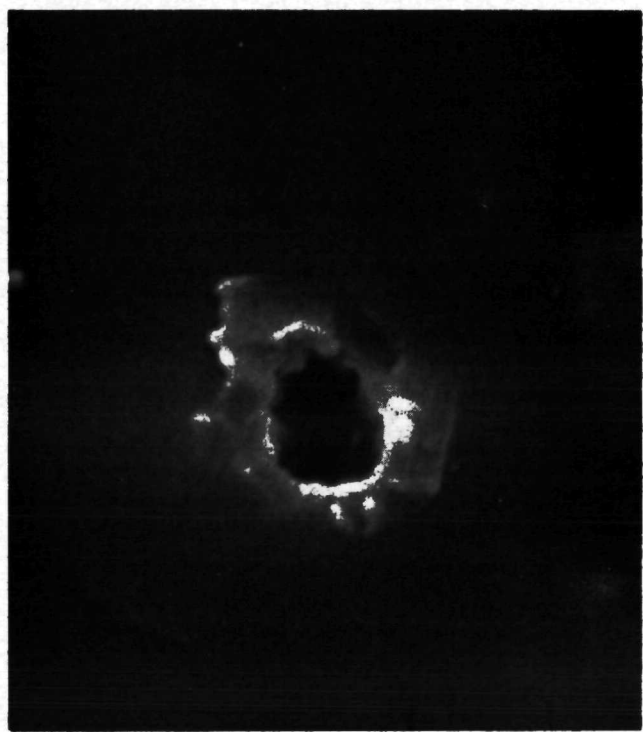
(a)



(b)

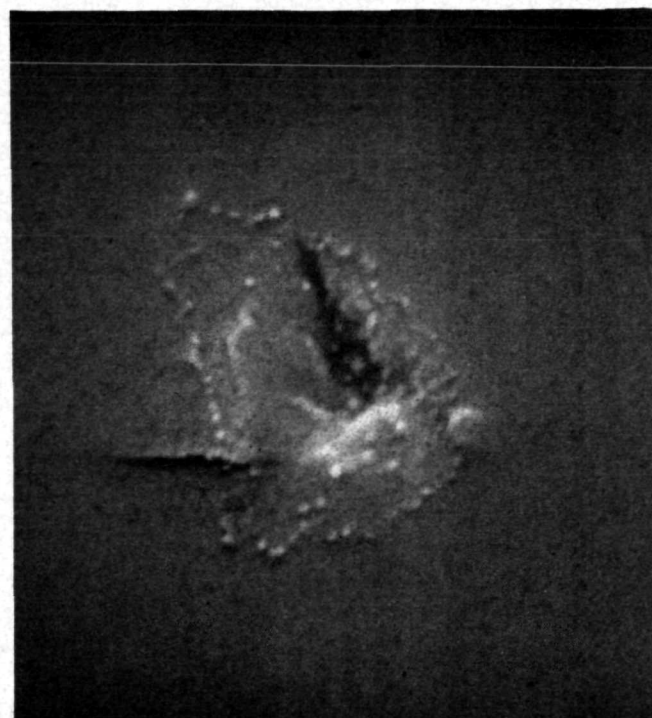


(c)

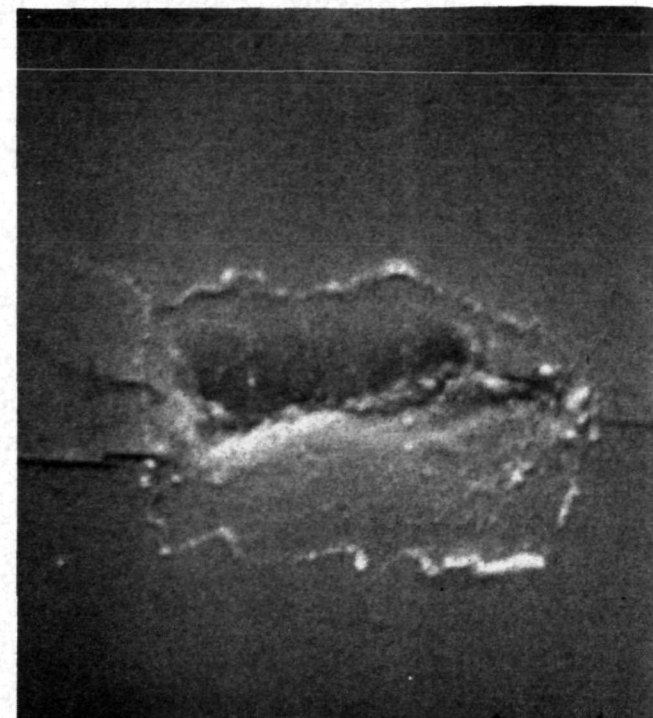


(d)

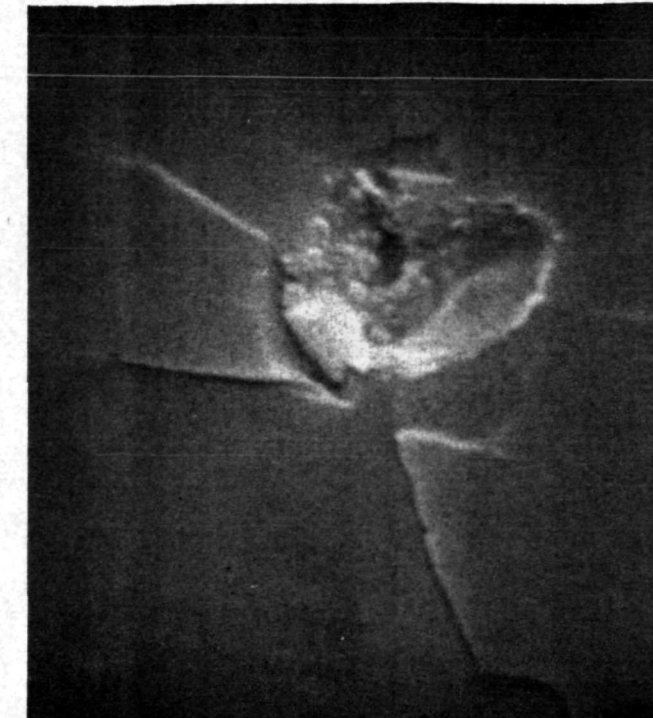
FIGURE 4-35. Photographs of Craters from Normal Impacts of Silicon Particles on Oligoclase, Surface Parallel to (001), 10.6 to 12.4 km/s: (a); crater S10-1-B, 10.6 km/s. (b); crater S10-1-C, 10.7 km/s. (c); crater S10-2-C, 11.5 km/s. (d); crater S10-1-A, 12.4 km/s. All have two micron indexes and 10° tilt angle.



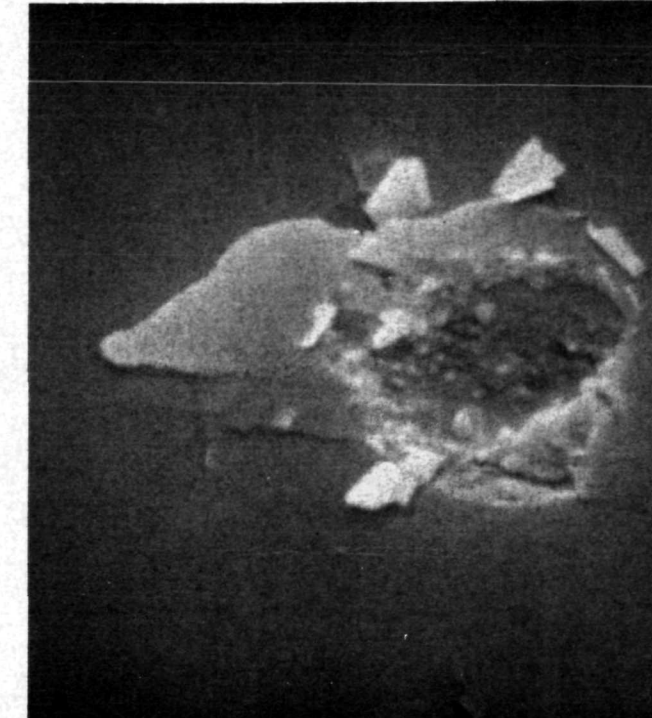
(a)



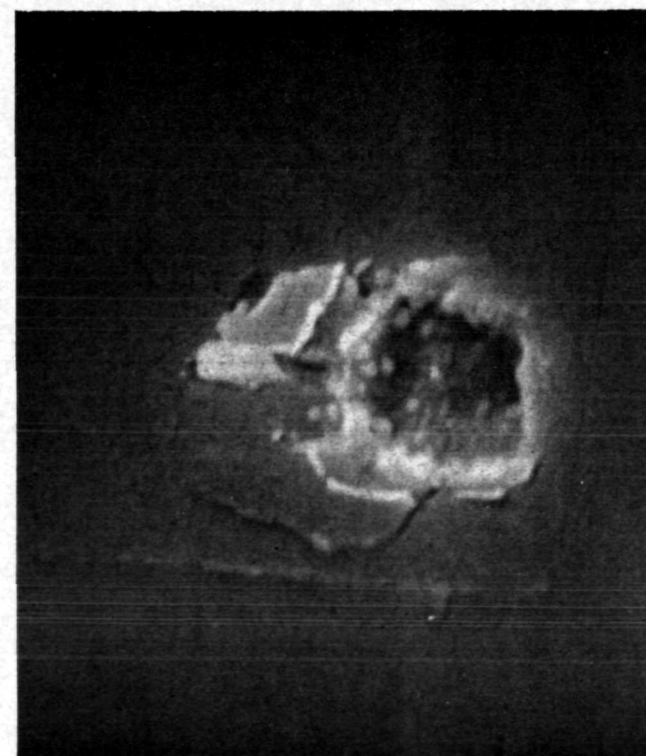
(b)



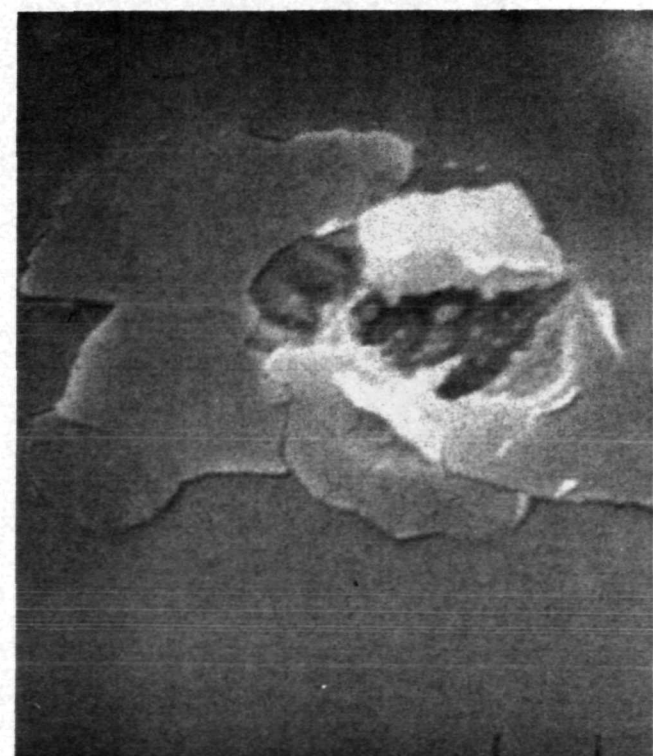
(c)



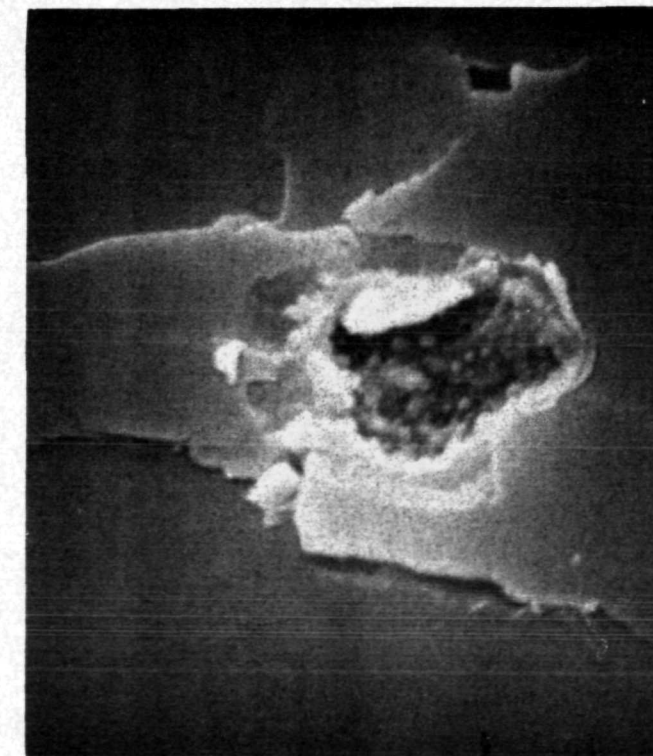
(d)



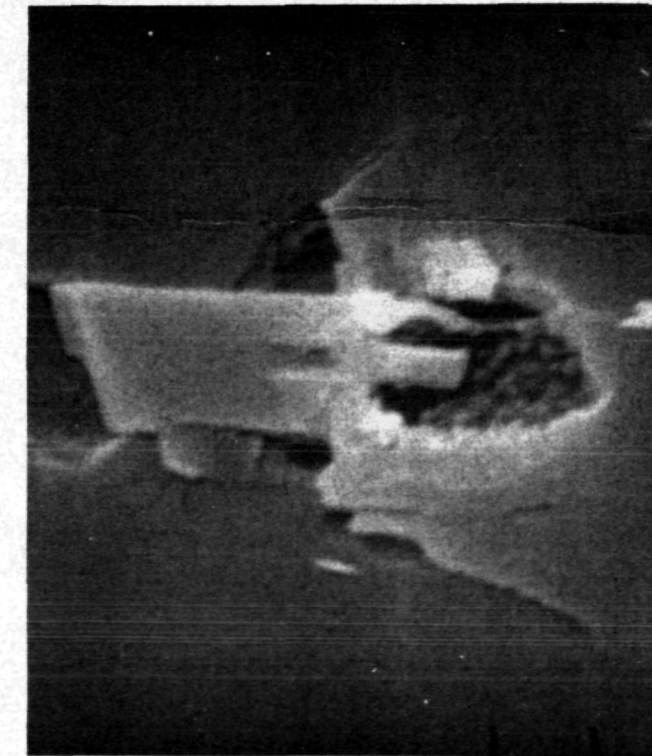
(e)



(f)

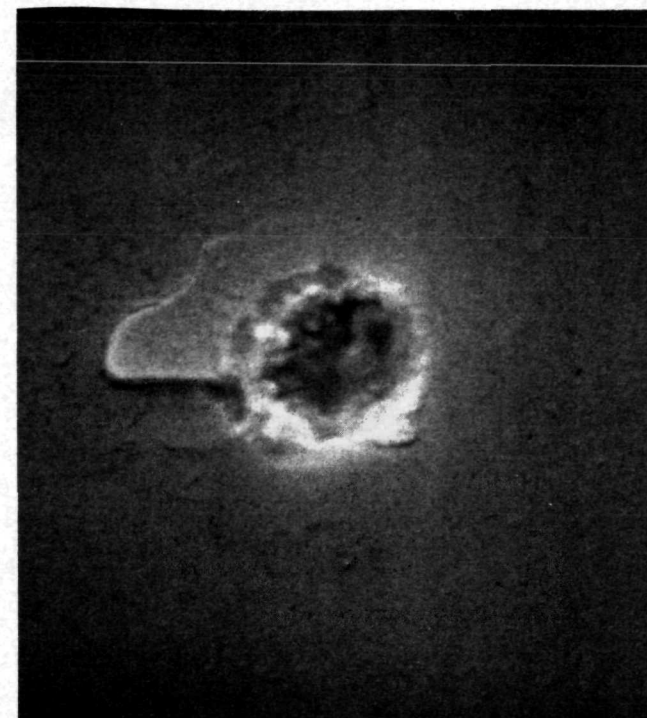


(g)

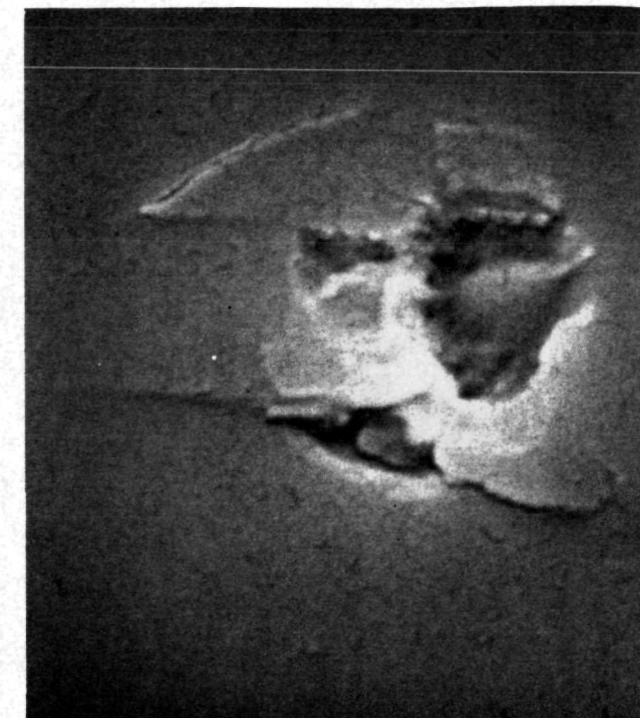


(h)

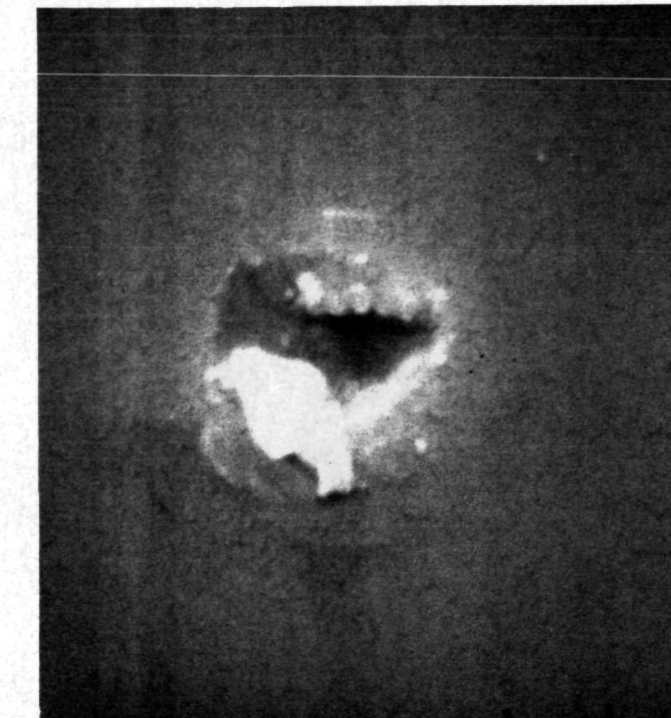
FIGURE 4-36. Photographs of Craters from 30° to Normal Oblique Impacts of Silicon Particles on Oligoclase, 2.31 to 8.18 km/s: (a); crater S5-13-D, 2.31 km/s. (b); crater S5-13-B, 3.12 km/s. (c); crater S5-16-A, 4.58 km/s. (d); crater S5-11-B, 4.78 km/s. (e); crater S5-4-B, 5.91 km/s. (f); crater S5-4-A, 6.53 km/s. (g); crater S5-9-A, 7.55 km/s. (h); crater S5-4-C, 8.18 km/s. (c) has 5 micron indexes, all others have 2 micron indexes. (c) and (d) have 15° tilt angles, all others have 20° tilt angle.



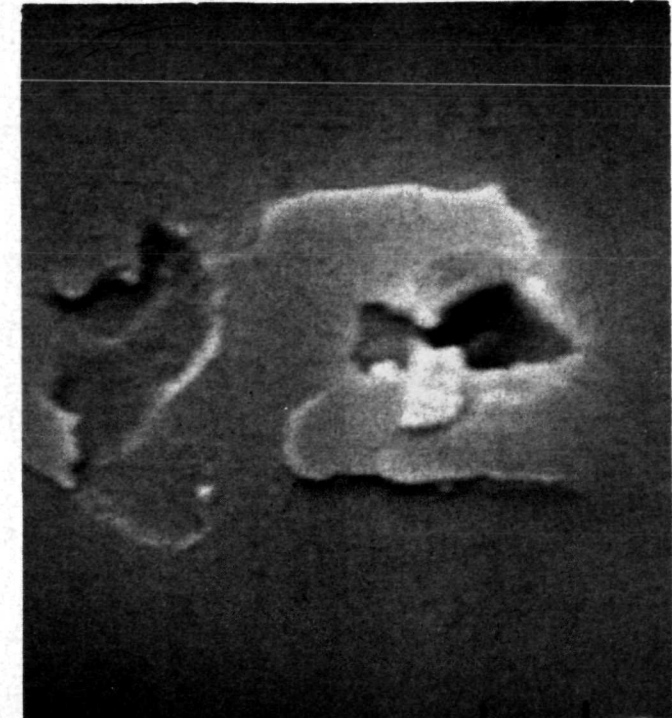
(a)



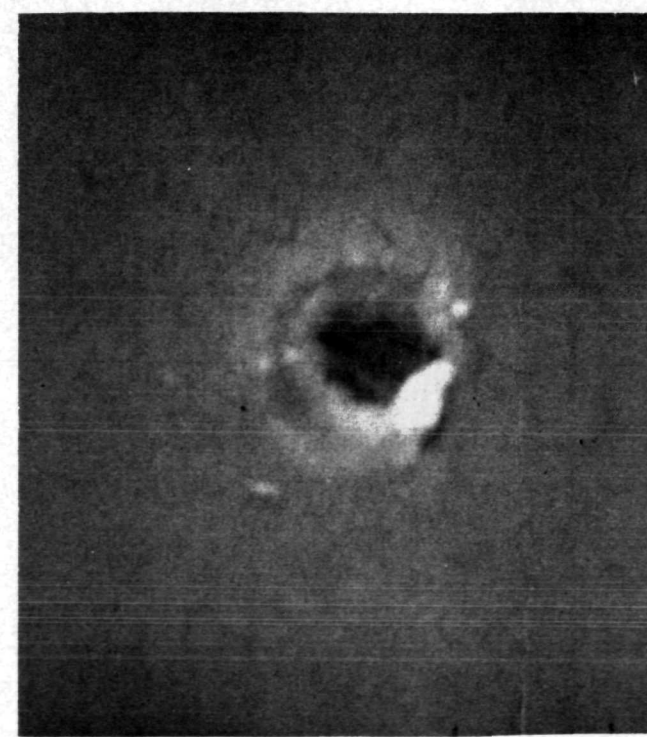
(b)



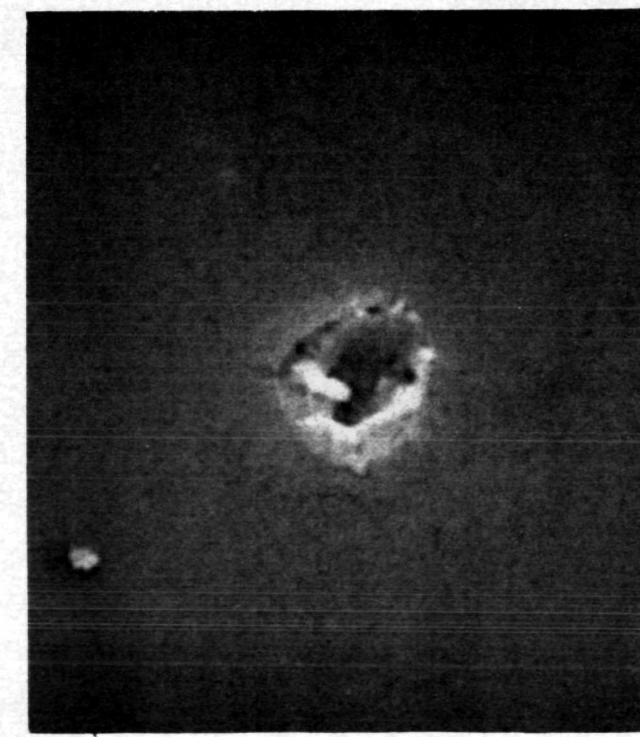
(c)



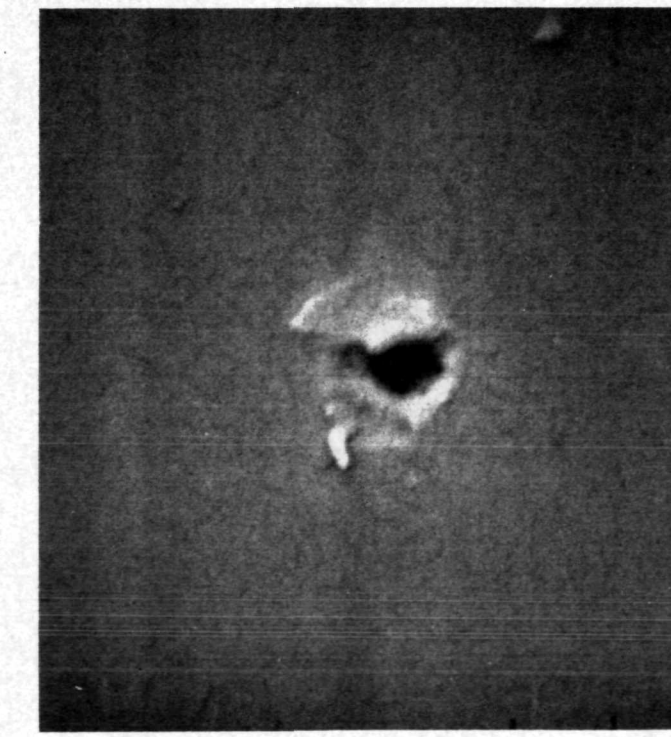
(d)



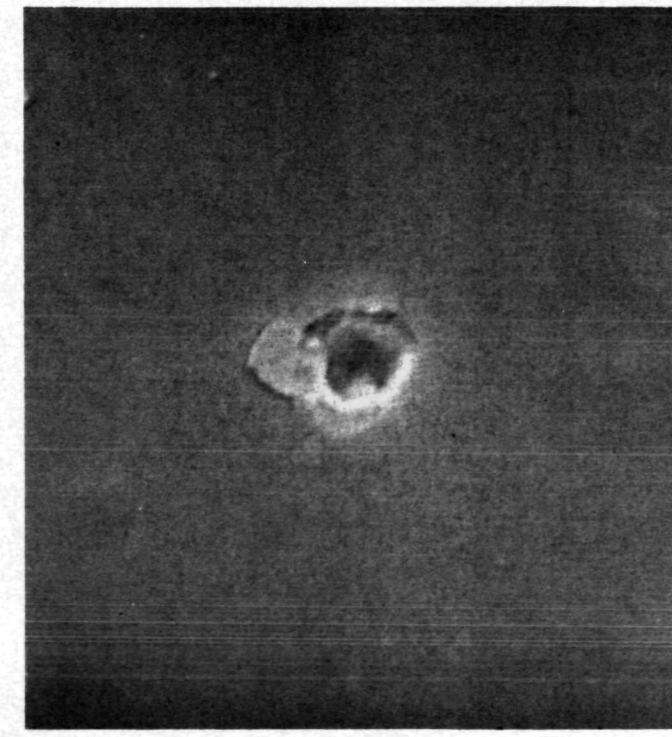
(e)



(f)



(g)



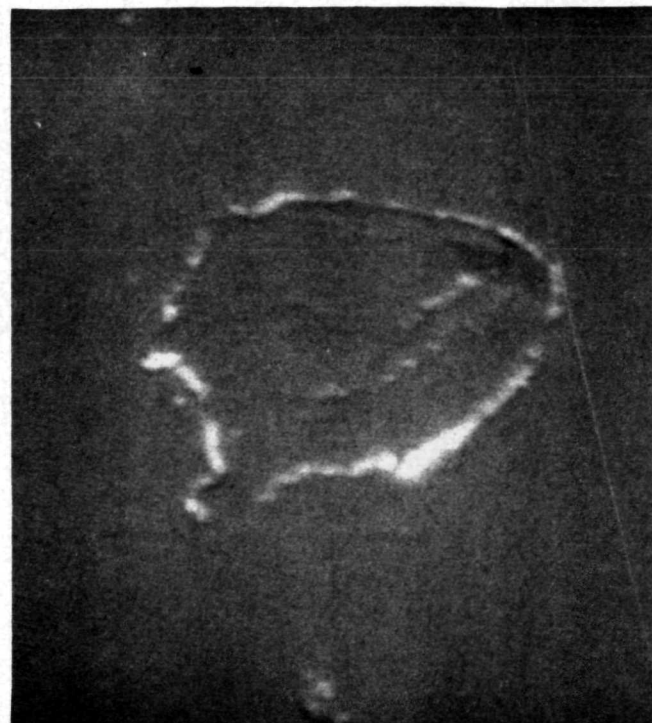
(h)

FIGURE 4-37. Photographs of Craters from 30° to Normal Oblique Impacts of Silicon Particles on Oligoclase, 10.5 to 20.6 km/s: (a); crater S6-8-A, 10.5 km/s. (b); crater S6-13-C, 10.6 km/s. (c); crater S6-13-B, 11.7 km/s. (d); crater S6-8-B, 14.3 km/s. (e); crater S6-6-D, 16.2 km/s. (f); crater S6-6-B, 16.9 km/s. (g); crater S6-6-A, 19.6 km/s. (h); crater S6-6-C, 20.6 km/s. All have 2 micron indexes. (a) through (d) have 20° tilt angle while (e) through (h) have 8.5° tilt angle.

at 2.31 km/s only cracks are produced and the "central pit" is in reality only a depression in the surface. The same is true of (b) at 3.12 km/s. In (c) at 4.58 km/s a recognizable central pit is beginning to form complete with sufficient melt to form droplets in the interior. Numerous droplets may be seen in the interior of all craters up to Figure 4-37b (10.6 km/s). In (b) the droplets are quite small. At higher velocities the resolution is either inadequate to detect droplets within the central pit or else the pit has a smooth interior, the smooth interior being more likely. The oblique nature of these impacts are much more difficult to determine from crater morphology than was iron particle impacts. At the higher velocities, Figure 4-37f, g, h, "memory" of the oblique nature of the impact is almost totally lost.

Figures 4-38 and 4-39 contain the crater photographs for the data of Table 17. These impacts occurred at  $60^\circ$  to normal on a surface parallel to (010). The velocity range for Figure 4-38 extends from 2.18 to 9.08 km/s while that in Figure 4-39 extends from 10.6 to 19.5 km/s. The first three craters of Figure 4-38 show only depressions in the surface where the central pit would normally be. In (d) at 4.57 km/s a central pit is developed along with extensive spallation; however, note that in (e) and (f) only depressions exist again, although some droplets have formed in (e). The light colored rings seen in (a), (b), (c), (e), and (f) are believed to be the remnants of the deposited aluminum film. Notice that spallation has essentially ceased at 10.6 km/s (Figure 4-39a). These craters are quite elongated and do show a "memory" of the oblique impact up to the highest recorded data for the set (19.5 km/s).

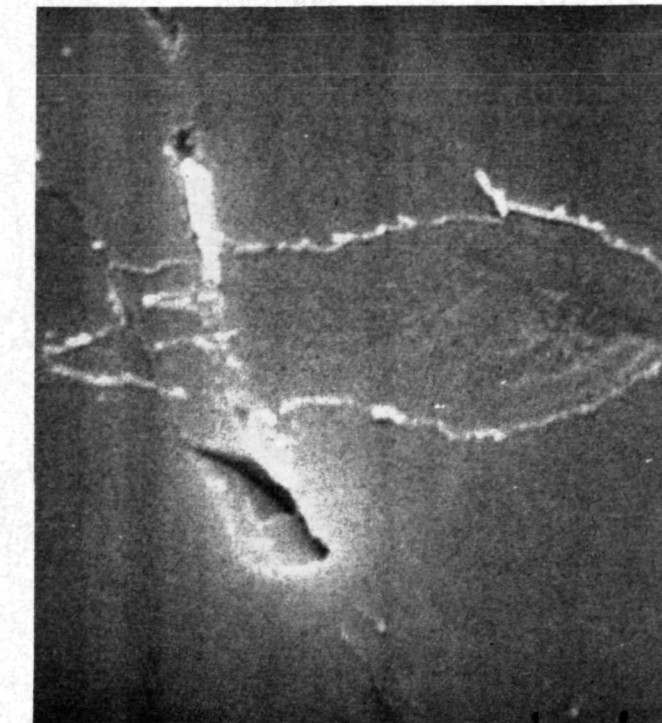
Attention should be called to Figure 4-39e. It is quite likely, in the authors' opinion, that the object to the upper right of the crater is the remains of a "jet" from the central pit of this crater. One may still observe a projection from the center of the crater. As a final



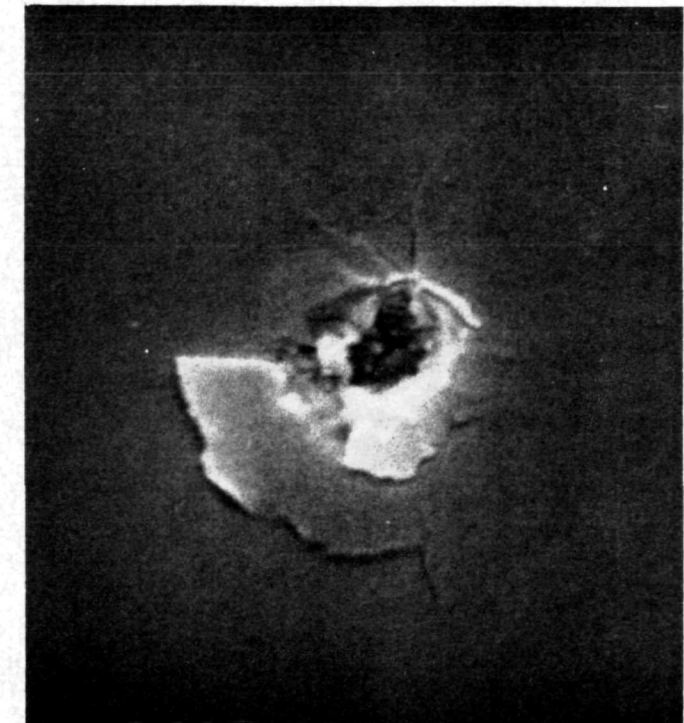
(a)



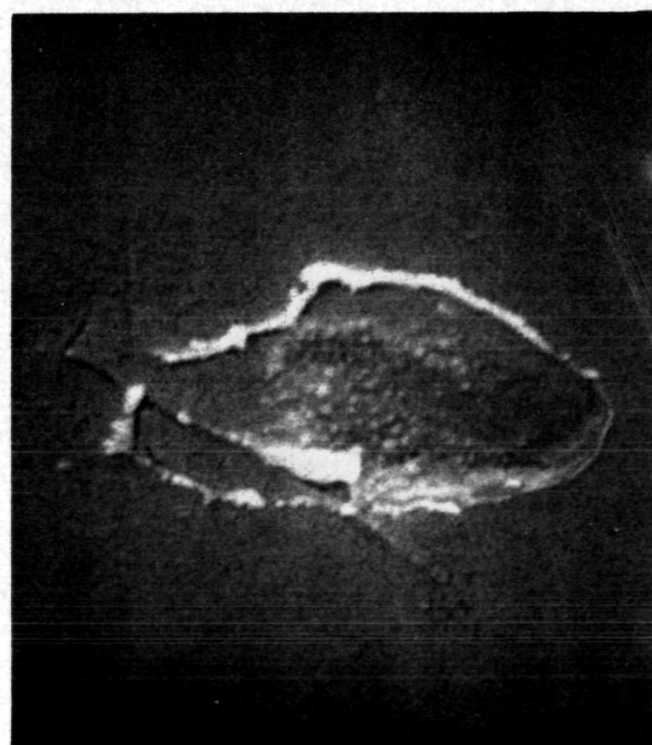
(b)



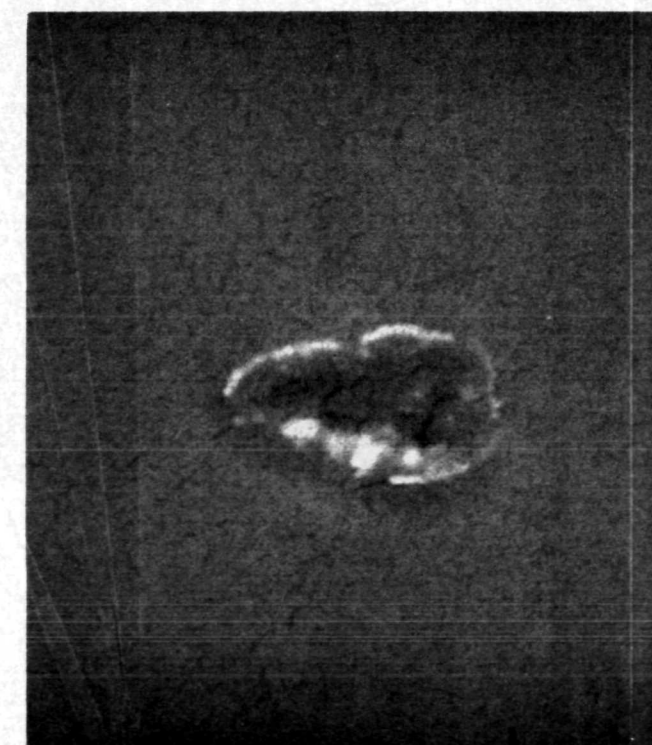
(c)



(d)



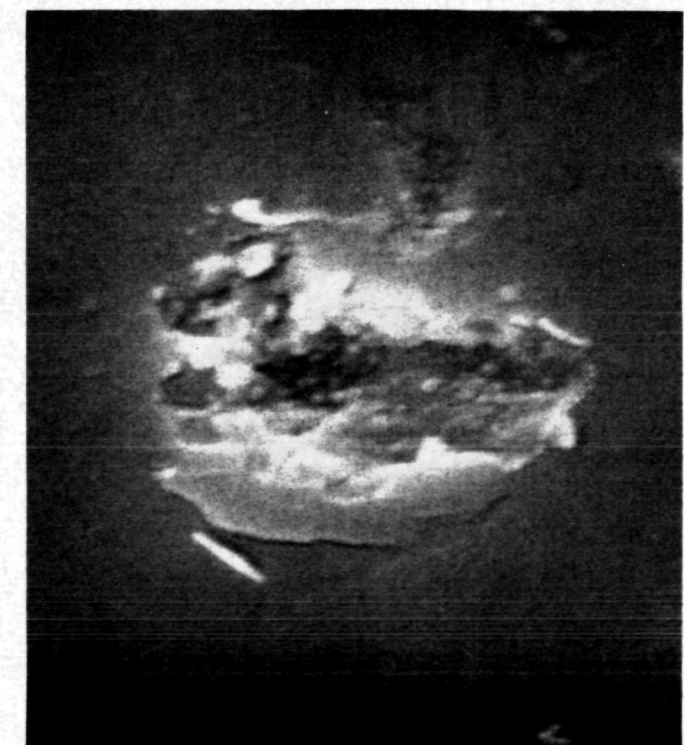
(e)



(f)

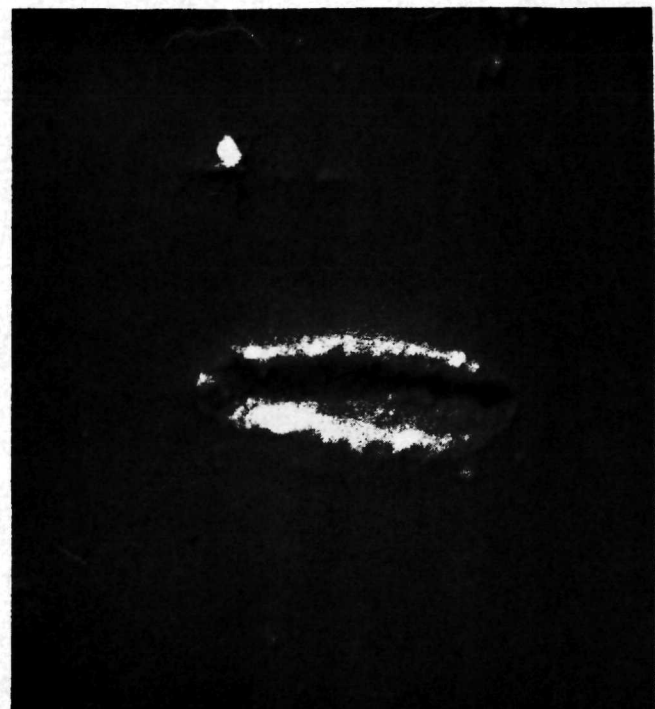


(g)

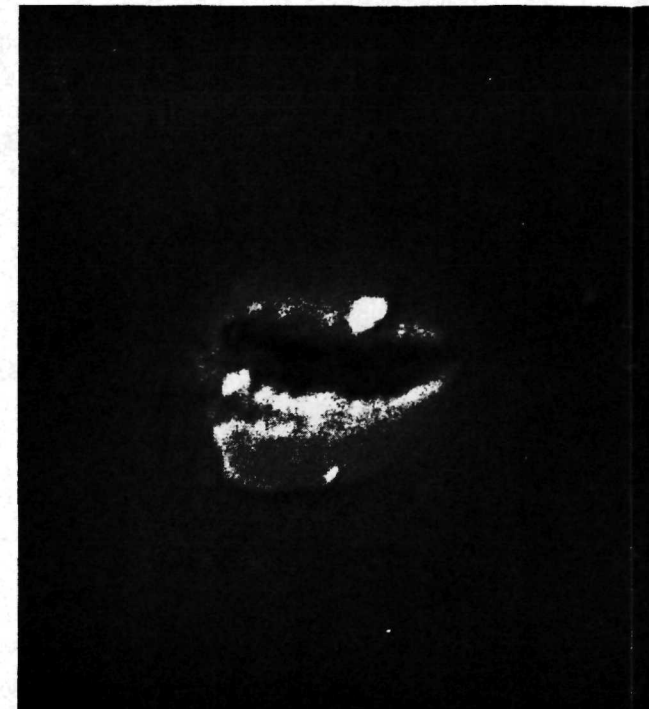


(h)

FIGURE 4-38. Photographs of Craters from 60° to Normal Oblique Impacts of Silicon Particles on Oligoclase, 2.18 to 9.08 km/s: (a); crater S5-19-A, 2.18 km/s. (b); crater S5-12-C, 3.23 km/s. (c); crater S5-12-A, 3.66 km/s. (d); crater S5-12-D, 4.57 km/s. (e); crater S5-10-A, 7.18 km/s. (f); crater S5-15-D, 8.18 km/s. (g); crater S5-5-A, 8.56 km/s. (h); crater S5-5-C, 9.08 km/s. All have 2 micron indexes and 20° tilt angle.



(a)



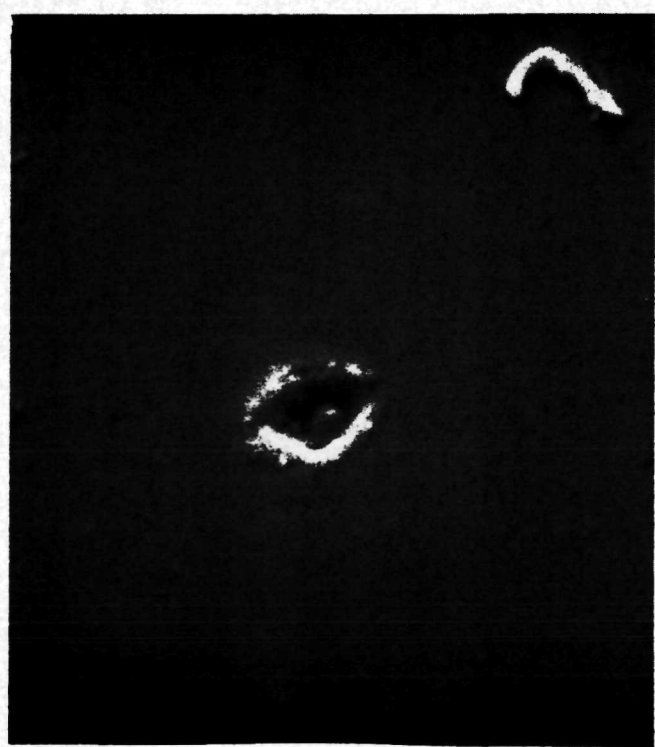
(b)



(c)



(d)



(e)



(f)



(g)



(h)

FIGURE 4-39. Photographs of Craters from 60° to Normal Oblique Impacts of Silicon Particles on Oligoclase, 10.6 to 19.5 km/s: (a); crater S6-14-B, 10.6 km/s. (b); crater S6-9-B, 12.1 km/s. (c); crater S6-14-A, 12.2 km/s. (d); crater S6-9-A, 14.2 km/s. (e); crater S6-12-A, 17.5 km/s. (f); crater S6-7-A, 17.9 km/s. (g); crater S6-12-B, 19.3 km/s. (h); crater S6-12-C, 19.5 km/s. All have 2 micron indexes and 20° tilt angle.

comment, some striking examples of jetting from impact craters were obtained on a similar program conducted by this organization under NASA sponsorship where the same particles used herein were impacted into quartz glass.<sup>9</sup> Certain of the quartz glass impacts showed long filaments still attached to the bottom of the crater pit. This jetting action was only observed in the 18 to 25 km/s range for quartz. It is believed that Figure 4-39e and Figure 4-27c are two examples of a similar action for oligoclase impacts.

5.0 SUMMARY

It is undoubtedly apparent to the reader at this point that this report contains a voluminous amount of data in the form of crater photographs for a variety of impact conditions. The intent of this report has been to reproduce herein as much of the acquired data as might be of use to the reader in understanding the subtle changes that occur in crater morphology as impact conditions are varied. It has been a further object of the report to reproduce the photographic data in a format which would permit a comparative analysis to be made between a crater having unknown impact parameters and those contained within. The final goal being to deduce some of the impact parameters from similarities between impact crater morphology.

In summary, we will attempt only to outline some of the gross differences or notable similarities observed. For the iron particle impacts, extensive spallation occurs at the lowest observed velocity (2.86 km/s) accompanied by sufficient melting to form a crater lip structure and to line the crater walls with droplets. The size of these droplets are seen to increase while their number decreases with increasing impact velocity. At 7 to 8 km/s only a few very large droplets are seen in the crater interior, a prominent lip structure has developed, and spallation has decreased to the point where only radial cracks are observed. Although it was not mentioned in the body of the report, ten low velocity impacts were obtained between 0.7 and 1.0 km/s. None of these impacts produced sufficient surface damage to allow the impact site to be located.

Much less spallation was observed from both the lanthanum hexaboride and silicon particle impacts than was seen from iron particle impacts. At 5 to 6 km/s, normal impact  $D_s/d$  for iron has a value of 8 to 9 while lanthanum hexaboride has a value of about 3 and silicon about 3 to 4. However, silicon particles were observed to produce spallation to much higher velocities than was  $\text{LaB}_6$  or iron. At 5 to 6 km/s,  $D_p/d$  for iron is about 1.1 while  $\text{LaB}_6$  is about 1.4 and silicon about 1.2.

Oblique impacts can generally be recognized as such due to elongation of the central crater along the direction of impact and by a "biasing" of the spallation produced toward the "downstream" side of the crater. For oblique angles slightly off the normal, the above characteristics do not exist at the higher velocities; however, for large angles (60° to normal) crater elongation is observed into the 20 km/s range.

## REFERENCES

1. Friichtenicht, J. F., "Two-Million-Volt Electrostatic Accelerator for Hypervelocity Research", Rev. of Sci. Instr., Vol. 33, No. 2, pp. 209-212, February 1962.
2. Shelton, H., Hendricks, C. D., and Wuerker, R. F., "Electrostatic Acceleration of Microparticles to Hypervelocities", Journ. of Appl. Phys., Vol. 31, No. 7, pp. 1243-1246, July 1960.
3. Roy, N. L., and Becker, D. G., "A Time Interval Selector and Proportional Delay Generator", Rev., of Sci. Instr., Vol. 42, No. 2, pp. 204-209, February 1971.
4. Hansen, D. O. and Roy, N. L., "A Solid-State Low-Noise Preamplifier", Nuclear Instruments and Methods, Vol. 40, pp. 209-212, North Holland Publishing Co., Amsterdam, 1966.
5. Becker, D. G., Friichtenicht, J. F., Hamermesh, B., and Langmuir, R. V., Rev. of Sci. Instr., Vol. 36, pp. 1480, 1965.
6. Final Progress Report: "Theoretical and Experimental Studies Relating to Use of a Linear Accelerator for Micrometeoroids", TRW Systems Group Document No. 03716-6010-R000, April 1967. Prepared Under Contract NAS1-4099, National Aeronautics and Space Administration, Langley Research Center, Hampton, Virginia.
7. Heavens, O. S., "Optical Properties of Thin Films", Butterworth, London, 1955.
8. "Handbook of Chemistry and Physics", 50th Edition, The Chemical Rubber Company, 1969.
9. Final Progress Report: "Study for Apollo Window Meteoroid Experiment (S-176)", TRW Systems Group Document No. 20921-6001-R0-00, July 1972. Prepared under Contract NAS9-12072, National Aeronautics and Space Administration, Manned Spacecraft Center, Houston, Texas.